Dissertation

submitted to the

Combined Faculty of Mathematics, Engineering and Natural Sciences

of Heidelberg University, Germany

for the degree of

Doctor of Natural Sciences

Put forward by

Apoorva Anant Hegde

born in: Sirsi, India

Oral examination: April 28, 2022

Noisy Dynamics of U(1) Lattice Gauge Theory in Ultracold Atomic Mixtures

Referees: Prof. Dr. Fred Jendrzejewski
Prof. Dr. Selim Jochim

सर्वद्रव्येषु विद्यैव द्रव्यमाहुरनुत्तमम् ।
अहार्यत्वादनर्घ्यत्वात् अक्षय्यत्वाच्च सर्वदा ।

"Of all the gifts that one should collect, and protect,
education is the most important one, for none can steal it.
It is the most valuable, the more you use it, the more it grows."

[0]Taken from *Sanskrit Subhashitagalu.* Poornaprajna Samshodhana Mandira. 2013. Translated to English by Dr. A. V. Nagasampige.

Abstract

Gauge theories are the governing principles of elementary interactions between matter particles and the mediating gauge fields. Even though they have been studied extensively in the realm of High Energy Physics (HEP), realizing their quantum dynamical aspects still remains an arduous task. Quantum simulators provide a promising approach in this regard by mimicking such systems, and mapping them onto other physical platforms that are experimentally accessible. In this thesis, an extension of the experimental studies undertaken to simulate a minimalistic version U(1) of Lattice Gauge Theory (LGT), also known as Schwinger model is presented [1]. The experiment conducted therein used an ultracold gas mixture of sodium ($^{23}\mathrm{Na}$) and lithium ($^{7}\mathrm{Li}$), where $^{23}\mathrm{Na}$ realized the gauge field and $^{7}\mathrm{Li}$ realized the matter component. The principle of local gauge invariance, which is a consequence of matter gauge coupling was realized through interspecies spin changing collisions (SCC). A theoretical framework based on mean field approach was then used to describe the corresponding experimental data. As the data was acquired over multiple realizations, it exhibited fluctuations, which were unaccounted for in the previous description of the model. This thesis provides an account of data analysis and theoretical treatments that were performed in order to investigate the cause of such fluctuations. Along with a better understanding of the underlying dynamics, this study opens up further insights. For instance, the fluctuations arising from finite temperature of the atoms might reveal the long time behavior of the system. Furthermore, fluctuations of technical origin are critical in assessing the stability of an experimental setup, which when reduced, pave the way to the study of quantum fluctuations, the role of which is pivotal in all the areas of fundamental physics.

Zusammenfassung

Eichtheorien sind die maßgeblichen Prinzipien der elementaren Wechselwirkung zwischen Materieteilchen und dem vermittelnden Eichfeld. Obgleich sie im Bereich der Hochenergiephysik ausgiebig untersucht wurden, ist die Realisierung ihrer quantendynamischen Aspekte noch immer eine mühsame Aufgabe. Quantensimulatoren bieten einen vielversprechenden Ansatz, indem sie solche Systeme auf andere physikalische Plattformen abbilden, die experimentell zugänglich sind. Diese Arbeit präsentiert eine Erweiterung der experimentellen Studien, die zur Simulation einer minimalistischen Version U(1) der Gittereichtheorie (LGT), auch bekannt als Schwinger Modell, durchgeführt wurden[1]. Hierbei wurde eine ultrakalte Quantengasmischung aus Natrium ($^{23}\mathrm{Na}$) und Lithium ($^{7}\mathrm{Li}$) verwendet, wobei $^{23}\mathrm{Na}$ das Eichfeld und $^{7}\mathrm{Li}$ die Materiekomponente darstellte. Das Prinzip der lokalen Eichinvarianz, das eine Folge der Materie-Eichfeldkopplung ist, wurde durch Spin-Austauschprozesse (SCC) zwischen den beiden Atomsorten realisiert. Zur Beschreibung der entsprechenden experimentellen Daten wurde ein theoretischer Rahmen, basierend auf der Molekularfeldtheorie, gewählt. Da die Daten über mehrere Realisierungen erfasst wurden, wiesen sie Fluktuationen auf, die in der vorherigen Beschreibung des Modells nicht berücksichtigt wurden. Diese Arbeit bietet eine umfassende Datenanalyse und beschreibt die theoretischen Herangehensweisen, die angewandt wurden, um die Ursache für diese Fluktuationen zu untersuchen. Neben einem besseren Verständnis der zugrundeliegenden Dynamik eröffnet diese Studie weitere Erkenntnisse. Zum Beispiel könnten die Fluktuationen, die sich aus der endlichen Temperatur der Atome ergeben, das Langzeitverhalten des Systems aufzeigen. Darüber hinaus sind technisch bedingte Fluktuationen entscheidend für die Beurteilung der Stabilität eines Versuchsaufbaus, und ebnen, wenn sie reduziert werden, den Weg zu Quantenfluktuationen, die in allen Bereichen der Grundlagenphysik eine zentrale Rolle spielen.

Contents

The account of research presented in this thesis is an extended study of the results published in the article below:

A scalable realization of local U(1) gauge invariance in cold atomic mixtures
Alexander Mil, Torsten. V. Zache, Apoorva Hegde, Andy Xia, Rohit Prasad Bhatt, Markus. K. Oberthaler, Philipp Hauke, Jürgen Berges, Fred Jendrzejewski
Science 367, 1128-1130 (2020)

Chapter 1

Introduction

1.1 Quantum simulations

The concept of simulation, in which one physical system is used to describe another has been a longstanding method of scientific practice. However, when quantum systems are considered, the usual practice of simulating them with classical computers suddenly becomes a next to impossible task due to the fact that the system scales exponentially with the number of its constituents. Tremendous efforts were made to solve these problems by means of approximations and numerical methods such as Monte-Carlo techniques[2, 3] and tensor network theory[4]. However, these methods have their own limitations and are not enough to tackle out-of-equilibrium problems[5]. Late 20^{th} century physicist Richard Feynman argued that if one were to simulate a physical many-body system, one would have to make use of the laws of quantum mechanics because nature is inherently quantum[6]. This marked somewhat informally, the birth of a quantum simulator (QS). The use cases of a QS, thus fall into either of the two categories or both; first, they can be used to access processes which lie beyond the capabilities of classical simulations or to significantly speed up the existing ones. Second, they act as analogue systems to an existing question of research, which is otherwise hard to understand through a conventional laboratory experiment. While there's no strict or universal definition of a QS, for it encompasses a wide range of adaptations depending on its applicability, it can be thought of as a well controlled experimental system used to imitate the behavior of a given physical system, by reproducing its Hamiltonian [7, 8, 9]. To successfully undertake such a task, a QS should contain the following aspects:

- particles obeying quantum statistics, such as bosons or/and fermions.
- well controlled initial state.
- engineering the system Hamiltonian with tunable interaction terms.
- faithful detection of the final state.
- verification

To this end, one can distinguish between two types of QS: Digital Quantum Simulators (AQS) and Analog Quantum Simulators (AQS). DQS stems from the circuit based approach of quantum computing where the wavefunction to be simulated is encoded in the computational ba-

sis and the unitary evolution is then carried out by qubit operations[10]. Hence, it is *universal* since the operations on the initial state can be written in terms of a set of universal gates[11]. However, the quest for a fully fledged general purpose universal quantum computer is still in progress, with rigorous amount of research put into scalability and error correction protocols[12]. Nevertheless, a QS could still be designed to solve specific problems that are otherwise inaccessible. When the evolution of a system to be simulated is mapped onto the controlled evolution of a QS, it goes by the name AQS. As this involves a rather one-to-one mapping between the two systems, its usage stays restricted to a limited class of problems. However, more often than not, its feature of being system specific has practical advantages[13, 14].

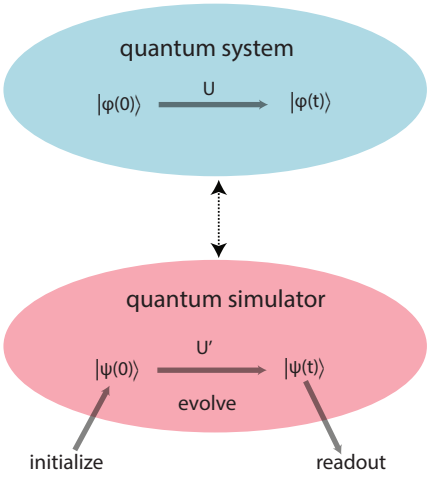

Figure 1.1: General idea of a quantum simulator. A QS should exhibit controllability such as initial state preparation, manipulation and appropriate detection methods. The states of the system are either encoded in qubits (DQS), or can be system specific with one-to-one mapping of the Hamiltonian (AQS).

Till date, both AQS and DQS have been realized in a highly controlled fashion in platforms based on trapped ions[15, 16], quantum dots[17], superconducting circuits[18, 19], photonic systems[20], Rydberg atoms[21], ultracold atoms[22, 23] and ultracold molecules[24]. The field has found unprecedented applications and continues to be the hope to solve more difficult and longstanding open questions in the field of condensed matter physics, high energy physics and quantum chemistry.

1.2 Ultracold atoms and Bose-Einstein condensates

There has been a booming development in the study of ultracold gases in the context of quantum simulation, thanks to the techniques like laser cooling and trapping, that laid the foundation for the experimental progress that was seen in cold dilute gases in the last two decades. In his Nobel lecture in 1997, William D. Phillips said, "In 1978 I had only vague notions about the excitement that lay ahead with laser cooled atoms, but I concluded that slowing down an atomic beam was the first step"[25]. In the 1970s, laser cooling was developed as a widely used technique towards highly precise measurements related to spectroscopy and atomic clocks. The prospects of working with slower and hence colder atoms promptly nudged yet another active field of research on superfluid ^{4}He, and its connection to Bose-Einstein condensation[26], a state of matter where a gas of bosons occupy the lowest energy state. The

occurrence of such a macroscopic ground state occupation in a gas of bosons below a certain critical temperature was first predicted by Satyendra Nath Bose and Albert Einstein in 1924. However, ^{4}He being a strongly interacting system, was a highly complicated system. In close contexts, dilute atomic gases emerged as ideal candidates, with their weakly interacting nature and their property of being controlled by laser light and magnetic fields. Thus, during the next 15 years, laser cooling techniques were combined with evaporative cooling, leading to groundbreaking observations of atomic Bose-Einstein condensations[27, 28, 29]. Since then, there have been rapid developments in the field of ultracold quantum gases where the properties of a BEC were studied intensively. Condensates have been widely used for atom-interferometry due to their coherent phase relations[30]. Trapping techniques that were independent of spin degree of freedom were developed, thus facilitating the creation of spinor condensates, which were highly promising candidates for the study of quantum magnetism, phase transitions, and a plethora of topics in condensed matter physics[31]. Further important milestones were the observation of Feshbach resonances[32], and the advent of optical lattices[33]. While Feshbach resonances allowed one to control the interaction between two atoms by applying an external magnetic field, optical lattices mimicked a defect free solid state environment. Along with a closely followed achievement of degenerate Fermi gas[34], these aspects naturally opened up dramatic possibilities in studying strongly interacting fermionic systems[35], phase transitions such as superfluid to Mott-insulator [36], BEC-BCS crossover[37], and as exotic as the realization of molecular condensates[38, 39].
Yet another class of dilute gases that significantly extended the class of phenomena that one could study were the heteronuclear systems, i.e., degenerate mixtures of two different species of either bosons or fermions or mixed. Some notable early examples include ^{6}Li-^{7}Li[40, 41], ^{23}Na-^{6}Li[42], ^{87}Rb-^{40}K[43, 44]. These experiments used the technique of sympathetic cooling where one species was cooled using a second species via collisions. Having observed simultaneous degeneracy, these mixtures were used to study the magnitude and nature of the interspecies interactions. Since then, mixtures have been used in the study of molecules[45], long range interactions in dipolar condensates[46] and impurity physics. In the latter, few or many atoms of one species (impurity) are immersed in a large condensate (bath) of the other species. Such a setting allowed one to study the coupling between the two, thereby exploring further aspects of an impurity-bath system such as decoherence effects[47], emergence of quasiparticles such as Bose or Fermi polarons[48, 49].

These are few examples in the long list of accomplishments in the field, which shaped itself into a very versatile and adaptable platform, becoming one of the most promising for quantum simulations.

1.3 Gauge theories and the lattice Schwinger model

In addition to the profuse examples of QS mimicking condensed matter systems, there has been a surge of interest in simulating High Energy Physics (HEP), such as gauge theories. As known from the Standard Model, which itself is a gauge theory, they are vital to the description of nature in that they govern the interaction between subatomic particles and their associated quantum fields, by means of strong and weak forces[50, 51, 52]. At its core, it signifies a mathematical formulation by means of gauge transformations, where certain redundant variables in a system of elementary particles are removed without altering the underlying physics. Consequently, the system is associated with a freedom of description, and obeys a

certain symmetry. The essence of gauge theories can be traced back to Maxwell's classical electromagnetism, where one could arbitrarily choose the scalar and the vector potential via gauge transformations, without affecting the resulting values of electric and magnetic fields. In the context of QS, they are incorporated in the form of Lattice Gauge Theories (LGT), where they are subjected to space-time discretization as a means of regularization[53]. Introduced first by K. Wilson in 1977, they soon emerged as effective ways of treating non-perturbative problems in QCD such as quark confinement, chiral symmetry breaking, and hadronization to name a few[54]. Moreover, the lattice formalism allowed for classical computational techniques like Monte-Carlo[55] and tensor network methods[56]. With high scope for its application in several areas of physics, quantum simulation of LGTs has been an actively pursed topic in the last decade, both theoretically and experimentally[57, 58, 59]. HEP models in particular demand a more complicated approach as one has to take care that the following criteria are fulfilled[60]:

- Inclusion of fermions and bosons: this stems from the Standard model that the matter particles are fermions, whose interactions are mediated by the gauge bosons.
- Principle of local gauge invariance/Gauss' law: this is a symmetry to be fulfilled. For example, the interactions between the electrons mediated by photons constitute U(1) gauge symmetry in QED.
- Lorentz invariance, which takes into account the relativistic effects.

One such model that has been investigated thoroughly both from a theoretical and an experimental perspective is the lattice Schwinger model. It is essentially QED in (1+1) dimension, which deals with fermionic matter fields coupled to bosonic gauge fields[61]. In its lattice Hamiltonian version, the fermionic degrees of freedom are defined on the lattice sites and the gauge fields, on the link connecting the adjacent sites[62](see chapter 2). The Gauss' law is then nothing but a local matter-gauge field coupling, signifying that the gauge transformations are the functions of the lattice sites. While it was originally defined in an infinite dimensional Hilbert space, the experimental friendly version was established through the Quantum Link Model (QLM), a mapping from HEP to quantum spin algebra with finite dimensions.

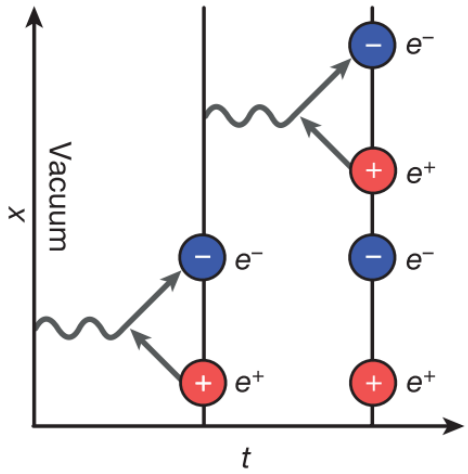

Figure 1.2: Mechanism of Schwinger pair production. QED predicts that when vacuum becomes unstable due to quantum fluctuations, it results in electron-positron pair creation. Image taken from[63].

The Schwinger model has been theoretically studied extensively over the years[64, 65, 66, 67] because it is the simplest gauge theory, but exhibits intriguing features like Schwinger pair production and string breaking[68], which extend to QCD. Hence, it provides a natural starting point for simulating HEP models, given that phenomena like these still belong to the class of problems which are extremely hard to observe directly.
The first experimental implementation in this regard came from a trapped ion based DQS[63]. They demonstrated the instability of vacuum via the dynamics of particle-antiparticle creation using $^{40}Ca^{+}$ ions confined in a linear Paul Trap. The internal state of each ion was encoded into spin-up and spin-down states, which could be manipulated by optical means, see Fig. 1.3a. The interactions and evolution were then engineered via a sequence of gate operations. Starting from an initial state resembling a bare vacuum, i.e., where the matter is absent, electric field term was scanned and the phenomenon of pair production was observed after a time evolution, see Fig. 1.3b. The observed trend in particle number density showed good agreement with theoretical predictions.

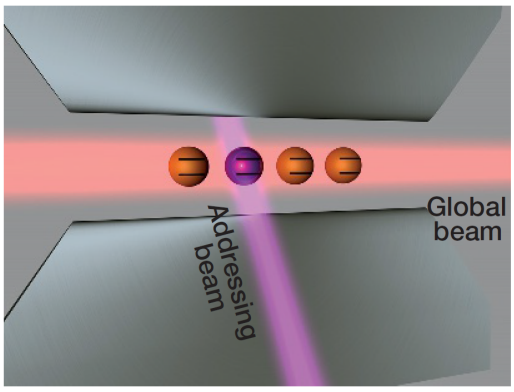

(a) Implementation scheme for Schwinger model with ions.

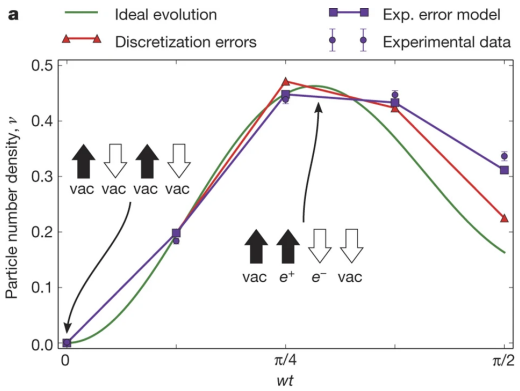

(b) Particle number as a function of electric field energy.

Figure 1.3: Experimental implementation of lattice Schwinger model in a trapped ion simulator. The internal states of the trapped $^{40}Ca^{+}$ ions were used as qubits and were selectively manipulated using laser beams. The unitary time evolution was then engineered with the help of gate operations. The process of pair production is observed as the particle number density goes from 0 to 0.5, where it corresponds to one pair on average. Image taken from [63].

Another notable contribution from trapped ions was the demonstration of a self-verifying QS of the Schwinger model using a classical-quantum hybrid algorithm[69]. A trapped ion AQS generated the trial states needed for the optimization scheme. The algorithm was then used to predict the ground state energy of the Schwinger model, and more importantly, the variances of the energies. Hence, it realized a verification process which is a prime step in showing the reliability of a QS.

The model was realized also in a Rydberg simulator, using ^{87}Rb atoms trapped in one dimensional optical tweezer arrays[70]. Coherent interactions were engineered by coupling the atoms from their ground state to Rydberg states. The setup therein originally described a Ising-type quantum spin model with tunable interactions[71]. Interestingly, it was shown that the same dynamics could be mapped exactly onto U(1) LGT with the help of QLM, and that the Gauss law could be implemented through the mechanism of Rydberg blockade[72].

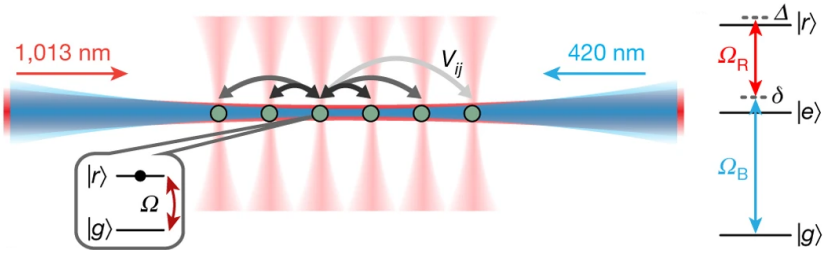

(a) ^{87}Rb atoms confined in optical tweezers.

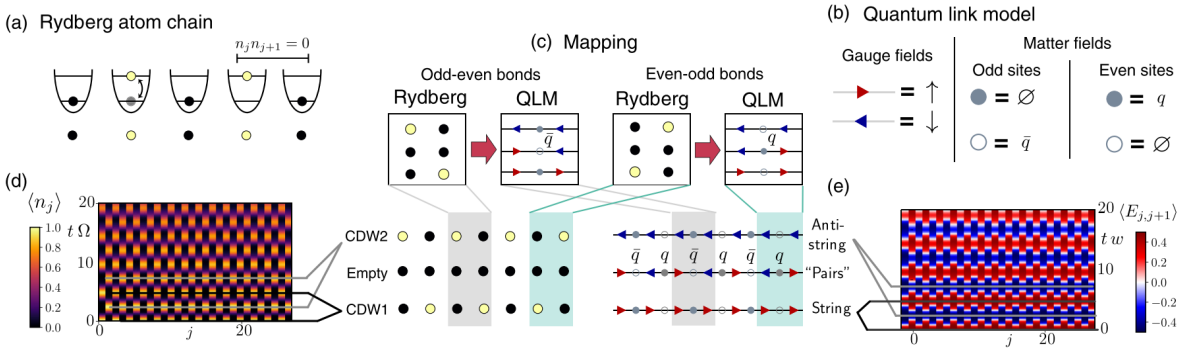

(b) Mapping of Rydberg traps to QLM

Figure 1.4: U(1) LGT in Rydberg simulator. (a). ^{87}Rb atoms trapped in optical traps are excited to Rydberg states with tunable coupling parameters. Image taken from[70]. **(b)** The 1D Rydberg chain is mapped onto Kogut-Susskind formalism of U(1) LGT using QLM. Figures shown in (d) and (e) show the time evolution of the Rydberg array and that of electric field in QLM respectively. Thus, the dynamics originally governed by quantum Ising-type Hamiltonian as in (d) is exactly mapped onto Schwinger model in (e). Image taken from [72].

In all the examples above, U(1) LGT was re-written in terms of effective models, where either one of the ingredients of gauge theory was eliminated in order to make it best suitable for experimental implementations. In [63] and [69], gauge field degrees of freedom were eliminated, thus effectively changing the original problem to a pure spin model with long-range spin-spin interactions. On the other hand, Rydberg simulator presented in [72] eliminated matter degrees of freedom, as a consequence which, only nearest-neighbour couplings would violate Gauss' law, which were already strongly suppressed by the Rydberg blockade. Contrary to both methods, an ultracold atom machine realized U(1) LGT inclusive of both degrees of freedom in an extended 1D lattice with 71 sites trapping ^{87}Rb atoms[73]. An optical superlattice was employed to realize the staggered structure with odd and even sites, which represented matter and gauge field respectively. The system, described by a Bose-Hubbard Hamiltonian, was mapped onto U(1) gauge theory, where the gauge invariance principle was realized by driving the system across a phase transition. As the Hubbard parameters were changed, single atoms residing in even sites bound to form doublons on odd sites, thus realizing the analog of annihilation of matter accompanied by a simultaneous deviation in the electric field, see Fig. 1.5b.

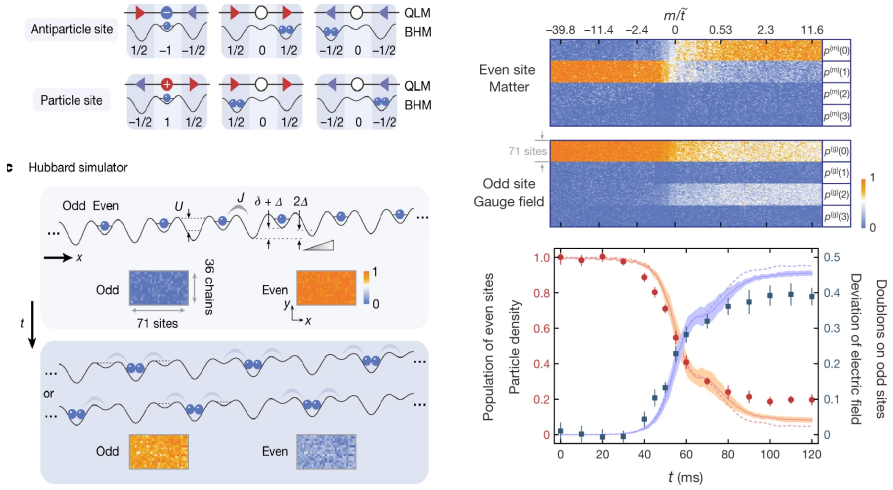

(a) mapping of Bose-Hubbard system onto QLM in staggered formulation.

(b) Observation of gauge invariant dynamics.

Figure 1.5: Simulating pair production mechanism using ^{87}Rb atoms confined in an optical superlattice. **(a)** the system obeys a Bose-Hubbard Hamiltonian with tunable parameters, which in turn is mapped onto QLM. Singly occupied even sites represent matter and doubly occupied odd sites represent gauge field. **(b)** starting from an initial Mott insulator state, Hubbard parameters such as mass and tunneling rate are ramped up, driving the system across a phase transition. The analogy of gauge invariance where is then attributed to the observation that the atoms initially residing in even sites (matter) transfer into odd sites forming doublons (gauge field). Images taken from [73].

Gauge theories are important not only in the context HEP, but they also emerge as effective theories in condensed matter systems and quantum information. Hence, it is worthwhile noting that there have been several experiments where they were implemented even though not in a dynamical fashion. For example, $\mathbb{Z}2$ gauge theory was implemented using Floquet engineering in ultracold ^{87} atoms[74]. Another experiment simulated a minimum toric-code Hamiltonian by devising four body ring-exchange interaction in ^{87}Rb atoms residing on the sites of a single plaquette[75].

Outline of the thesis

This thesis elaborates on the results of the experiment conducted using a quantum degenerate mixture of $^{23}\mathrm{Na} - {}^{7}\mathrm{Li}$, to quantum simulate a fundamental building block of Schwinger model. The experimental implementation exploited the internal states of sodium to mimic the gauge field, and lithium that of matter. As the original model describes QED on a one dimensional lattice, this experimental realization is considered as simulating one lattice site. Similar to the various examples given section 1.3, QLM mapped the gauge invariant interaction to interspecies spin- changing collisionsSCC. The same process was also described akin to pair production mechanism. Moreover, the mediated interaction makes the gauge field dynamical. Several measurements were undertaken to demonstrate the aspects of tunability and control. The foundation of the research presented in this thesis lies in the first experimental results on SCC, along with the mean field theoretical model, with which it was described. The analysis presented here investigates the fluctuations observed in the raw data, thereby leading to a better understanding of the interspecies dynamics.

- **Chapter 2**: theoretical background that is relevant to the experimental platform and discussion of data are presented. Starting out with a basic description of Bose gases using Gross-Pitaevskii Equation (GPE), the chapter further elaborates on the mathematical formulation of U(1) LGT, and its mapping onto ultracold gases with spin degree of freedom, using QLM. With that established, a mean field approach is used to realize the QS Hamiltonian in terms of quantum mechanical spin operators and hence implement local gauge invariance in ultracold $^{23}\mathrm{Na}$-$^{7}\mathrm{Li}$ mixture.

- **Chapter 3**: the experimental apparatus that produced the condensate mixtures is revisited, alongside the experimental sequence itself. As most parts of the setup were built well before the research presented here, only a brief description is provided to guide the reader through the sequential stages leading to the observation of condensates. However, many of these parts were replaced or upgraded during the course of this thesis, the description of which, is provided as and when relevant. Furthermore, crucial steps involved in engineering the interspecies SCC as an analog of Gauss' law are explained. All the raw data, where the SCC were observed are displayed for different types of measurements undertaken.

- **Chapter 4**: main findings of the study of fluctuations are presented. Starting out with a compact description of the comparison of the SCC data with the mean field spin model that was published in [1], further analysis is carried out in light of the observed fluctuations in the raw data. The results of these analyses are crucial for a more precise understanding of the data. Consequently, the origin and behavior of these fluctuations are discussed using rigorous theoretical treatments, followed by independent, yet intriguing interpretations of the data.

The overall concept of the thesis is summarized in the outlook chapter, along with prospects and applicability of this research.

Chapter 2

Theoretical concepts

This chapter mainly focuses on the general theoretical concepts that are relevant for the description of the experiment. The topic of a non-interacting Bose gas and its occupation of the macroscopic ground state upon condensation have been extensively covered in the realm of statistical physics[76]. Here, a rather qualitative description of the preliminary concepts of Bose-Einstein condensates are presented, mainly motivated by the literature presented in [77]. The treatment of Bose gas is further modified, considering the weak inter-particle interactions, since it is the most fitting description to the experimental platforms. In light of using the mixture of $^{23}\mathrm{Na} - {}^{7}\mathrm{Li}$ as a simulator of the building block of U(1) LGT, the second part of this chapter entails the general idea and constraints associated with simulating HEP models, such as the principle of local gauge invariance, also known as Gauss' law. The theoretical framework of quantum link model of QLM is presented, which is essentially a mapping from the framework of HEP to quantum spin algebra. This follows closely with the concept of treating the atomic ensembles as effective spins. Having established these aspects, the chapter further addresses how a degenerate Bose-Bose mixture of $^{23}\mathrm{Na} - {}^{7}\mathrm{Li}$ emulates the building block of U(1) gauge theory, using the internal states of two species.

2.1 Non-interacting Bose gas

For a gas composed of bosonic atoms at a finite temperature, the distribution of mean occupation number of single-particle states is given by

$$f^0(\epsilon_\nu) = \frac{1}{e^{(\epsilon_\nu - \mu)/\kappa_B T} - 1} \tag{2.1}$$

with ϵ_ν being the energy of the single-particle state, T, the equilibrium temperature of the gas, κ_B, Boltzmann constant. μ is the chemical potential, fixed by the the normalization condition $\sum_\nu f^0(\epsilon_\nu) = N$, i.e., the total number of particles in the gas is equal to the sum of the individual occupancy of levels. At high temperature, the equation (2.1) is approximated by the classical Boltzmann distribution,

$$f^0(\epsilon_\nu) \simeq e^{-(\epsilon_\nu - \mu)/\kappa_B T} \tag{2.2}$$

and μ is much less than ϵ_{min}, the minimum possible energy of a single-particle state. When the overall temperature goes down, chemical potential becomes less and less negative, and the criticality sets in when it approaches ϵ_{min}. As the equation (2.1) indicates, μ has an upper bound, that it only can reach a maximum value of ϵ_{min}, otherwise the occupation number

would become negative, which is nonphysical. Consequently, this sets a limit of on the occupation number of the excited state to be $1/\{exp[(\epsilon_\nu - \epsilon_{min})/\kappa_B T] - 1\}$. If the number of particles in the excited state is less than the total N, the remaining particles occupy the ground state. Thus, any additional particle added gets accommodated in the ground state, where there is no limit to the occupation number. This phenomenon is the transition to BEC, and the temperature at which it occurs is called the critical temperature, T_c. It is the maximum value of temperature where a condensate can exist. While this is a general description for a homogeneous Bose gas, the properties of a condensate depend on the kind of confining potential. In the case of bosons confined in a harmonic trap, the minimum energy of a single particle state is the zero point energy. However, it can be neglected for large N and can be set to zero[1]. Hence, the highest value that μ can attain is zero. With this condition, the critical temperature for a Bose gas in a 3D harmonic trap is found to be,

$$T_c \approx 0.94 \left(\frac{\hbar \bar{\omega} N^{1/3}}{\kappa_B} \right) \tag{2.3}$$

where $\bar{\omega}$ is the geometric mean of the trapping frequencies. Additionally, it is helpful to rewrite it in terms of particle number density n,

$$T_c \approx 3.31 \left(\frac{\hbar^2 n^{2/3}}{m \kappa_B} \right); \quad n = N/V \tag{2.4}$$

because it leads to the definition of yet another transition parameter called the phase-space density n_{ph}. It is a dimensionless quantity that corresponds to the number of particles present within a volume equal to the cube of the thermal de-Broglie wavelength, and is given by

$$n_{ph} = n \left(\frac{2\pi\hbar^2}{m \kappa_B T} \right)^{3/2} \tag{2.5}$$

where $\left(\frac{2\pi\hbar^2}{m\kappa_B T} \right) = \lambda_T^3$. According to the equation (2.4), the BEC occurs at a critical density of ≈ 2.612.

2.1.1 Condensate fraction and temperature

The ratio of the number of particles N_0 that exist in the macroscopic ground state to the total number particles N is called the condensate fraction and is given by

$$\eta_c = \frac{N_0}{N_0 + N_{th}} = 1 - \left(\frac{T}{T_c} \right)^3 \tag{2.6}$$

where N_0 and N_{th} are the number of particles in the macroscopic ground state and the thermally excited state. This expression is once again specific to the 3D harmonic trap. Hence the number of particles in the condensate is,

$$N_0 = N \left[1 - \left(\frac{T}{T_c} \right)^3 \right] \tag{2.7}$$

[1]It can be treated as a correction[77].

The density distribution of particles in the condensed state implies the shape of the ground state wavefunction $\phi_0(\mathbf{r})$, which for an anisotropic 3D harmonic trap is given by

$$\phi_0(\mathbf{r}) = \frac{1}{\pi^{3/4}(a_x a_y a_z)^{1/2}} e^{-x^2/2a_x^2} e^{-y^2/2a_y^2} e^{-z^2/2a_z^2} \tag{2.8}$$

where a_i are the oscillator lengths in the three spatial directions, decided by the the corresponding trapping frequencies,

$$a_i = \sqrt{\frac{\hbar}{m\omega_i}} \tag{2.9}$$

The density distribution of the non-condensed part is given by,

$$n(\mathbf{r}) = \frac{N}{\pi^{3/2} R_x R_y R_z} e^{-x^2/R_x^2} e^{-y^2/R_y^2} e^{-z^2/R_z^2} \tag{2.10}$$

where R_i are the widths of the clouds,

$$R_i = \sqrt{\frac{2\kappa_B T}{m\omega_i^2}} \tag{2.11}$$

2.2 Weakly interacting BEC

The interactions between particles are essentially described by scattering processes. If the particles are separated by a large distance such as those in a BEC, the scattered wave is a spherical wave given by $f(\vec{k})exp(ikr)/r$ where $f(\vec{k})$ is called the scattering amplitude and $\vec{k}$ is the wave vector of the scattered wave. In low energy systems, it is sufficient to consider the s-wave scattering. Then the scattering amplitude approaches a constant which is called the scattering length. Typically, the value of the scattering length is much smaller than the inter-atomic distances of a dilute gas. Hence, it is safe to assume that dominant interactions in system of a dilute ultracold boson gas comes from the so called binary collisions, i.e., due to two-body encounters. While the interaction in dilute alkali gases can be described by a Van der Waals interactions[77], the effective form of interactions in momentum representation is given by

$$g = \frac{4\pi\hbar^2 a}{m} \tag{2.12}$$

where a is the scattering length and m is the mass of the atom. Such a system at zero temperature is described by time-independent Gross-Pitaevskii equation (GPE),

$$-\frac{\hbar^2}{2m}\nabla^2\psi(\mathbf{r}) + V(\mathbf{r})\psi(\mathbf{r}) + g|\psi(\mathbf{r})|^2\psi(\mathbf{r}) = \mu\psi(\mathbf{r}) \tag{2.13}$$

V is the total external potential, $g|\psi(\mathbf{r})|^2$ is the mean field potential. The density of this macroscopic occupation is given by

$$n(\mathbf{r}) = |\psi(\mathbf{r})|^2 \tag{2.14}$$

Considering the experimental relevance, it is worthwhile to adapt the GPE for bosons confined in a three dimensional harmonic trap, whose potential is given by

$$V(x, y, z) = \frac{1}{2}m(\omega_x x^2 + \omega_y y^2 + \omega_z z^2) \tag{2.15}$$

where ω_x, ω_y and ω_z are the trapping frequencies in the respective spatial direction. When the interactions are repulsive and the number of atoms is large, the ratio of kinetic energy to the potential energy is small. The energy per particle is then given by

$$\frac{E}{N} = \hbar\omega_0 \left(\frac{Na}{a_{osc}}\right)^{2/5} \tag{2.16}$$

where $\bar{\omega} = (\omega_x\omega_y\omega_z)^{1/3}$ is the geometric average of the trapping frequencies, N is the number of atoms and a_{osc} is the characteristic harmonic oscillator length, which is nothing but a measure of the spatial extent of the atomic cloud. Neglecting the kinetic energy in the overall GPE simplifies (2.13) to,

$$V(\mathbf{r})\psi(\mathbf{r}) + g|\psi(\mathbf{r})|^2\psi(\mathbf{r}) = \mu\psi(\mathbf{r}) \tag{2.17}$$

and for density,

$$n(\mathbf{r}) = |\psi(\mathbf{r})|^2 = \frac{[\mu - V(\mathbf{r})]}{g} \tag{2.18}$$

This is called Thomas-Fermi approximation. The extension of the cloud in this approximation is given by

$$R_i^2 = \frac{2\mu}{mw_i^2}; \quad i = x, y, z \tag{2.19}$$

The atom number and the chemical potential are related by

$$N = \frac{8\pi}{15}\left(\frac{2\mu}{m\bar{\omega}^2}\right)^{3/2}\frac{\mu}{g} \tag{2.20}$$

Moreover, the density distribution can be rewritten as,

$$n_{TF} = \frac{15}{8\pi R_x R_y R_z}\left(1 - \frac{x^2}{R_x^2} - \frac{y^2}{R_y^2} - \frac{z^2}{R_z^2}\right) \tag{2.21}$$

which features an inverted parabola.
Reducing the temperature of the atoms below the critical temperature results in condensation and as the temperature is reduced further, the number of condensed atoms grows larger until $T = 0, N_0 = N$, i.e. all of the atoms are in the condensate. Apart from the physically unattainable state of $T = 0$, the condensed atoms co-exists with the non-condensed and hence thermal atoms.

2.3 U(1) lattice gauge theory

The next step after cooling the atoms to degeneracy is to manipulate them in ways to fit the specific requirements of a QS, designed to simulate a given physical system. Here, the system of interest is U(1) LGT, the gauge theory that governs QED. In this section, the concept of local U(1) gauge theory is introduced, followed by an illustration of its Hamiltonian formulation on a 1D lattice. The three components that constitute the theory are described, namely matter field, gauge field and their coupling.

2.3.1 Origin of gauge fields and Gauss' law

Free matter particles in an one dimensional lattice[2] are described by the Hamiltonian

$$H = -t\sum_{n}(\psi^{\dagger}_{n+1}\psi_n + h.c) + m\sum_{n}(-1)^n\psi^{\dagger}_n\psi_n \tag{2.22}$$

where ψ and $\psi^{\dagger}$ are the creation and annihilation operators of the matter field respectively, n is the index of the lattice site and m is the particle mass, and t is the strength of the tunneling matrix element. The factor $(-1)^n$ realizes the staggered mass. The field operators when subjected to global U(1) gauge transformations transform as,

$$\psi_n \rightarrow e^{i\alpha}\psi_n \quad ; \quad \psi^{\dagger}_{n+1} \rightarrow e^{i\alpha}\psi^{\dagger}_{n+1}, \quad \alpha \in \mathbb{R} \tag{2.23}$$

Here U(1) corresponds to a gauge group whose elements can be parametrised as phases α as they span a circle in the complex plane. As long as the phase is altered everywhere equally, equation (2.22) stays invariant by mapping the Hamiltonian onto itself under transformations. Consider the class of transformations where the group elements are given by

$$\psi_n \rightarrow V_n\psi_n \quad ; \quad \psi^{\dagger}_n V_n, \quad \text{with} \quad V_n = \exp\left(i\sum_{n}\alpha_n G_n\right) \tag{2.24}$$

where G_n is the generator of transformation. α_n now explicitly depends on the lattice site n, i.e., $\alpha_n \neq \alpha_{n+1}$. The hopping term transforms as,

$$\psi^{\dagger}_{n+1}\psi_n \rightarrow \psi^{\dagger}_{n+1}V^{\dagger}_{n+1}V_n\psi_n \tag{2.25}$$

which clearly shows that the H is not invariant under the transformation given in equation (2.24), i.e., the system doesn't possess a local U(1) symmetry naturally.

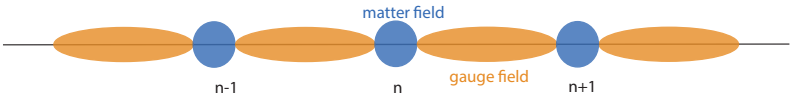

Figure 2.1: Visualization of LGT. Matter fields reside on the lattice sites (blue circles). Gauge fields connect the two adjacent sites (orange ellipses).

However, the gauge symmetry can be restored locally by introducing a new set of operators, called the link operators U_n. These are the so called *gauge links* because they act on the link connecting the two lattice sites, see Fig. 2.1. They transform as,

$$U_n \rightarrow V_{n+1}U_nV^{\dagger}_n \tag{2.26}$$

with $[U_n, U^{\dagger}_m] = 0$. The term in equation (2.25) then transforms as,

$$\psi^{\dagger}_{n+1}U_n\psi_n \rightarrow \psi^{\dagger}_{n+1}V^{\dagger}_{n+1}V_{n+1}U_nV^{\dagger}_nV_n\psi_n = \psi^{\dagger}_{n+1}U_n\psi_n \tag{2.27}$$

leading to

$$H \rightarrow VHV^{\dagger}. \tag{2.28}$$

[2]The reduced Planck's constant $\hbar$ and speed of light c are set to 1 throughout this theoretical description.

Introducing the gauge fields into the theory of free matter particles not only keeps the Hamiltonian invariant under gauge transformation, but also introduces a new constraint; interaction between matter field and the gauge field. In the case of QED, the matter corresponds to fermions and gauge field is represented by electric field. Hence the generators G_n of the local transformation (2.24) which results in equation (2.28) are represented by the operator,

$$G_n = E_{n+1} - E_n - e\psi_n^\dagger \psi_n \tag{2.29}$$

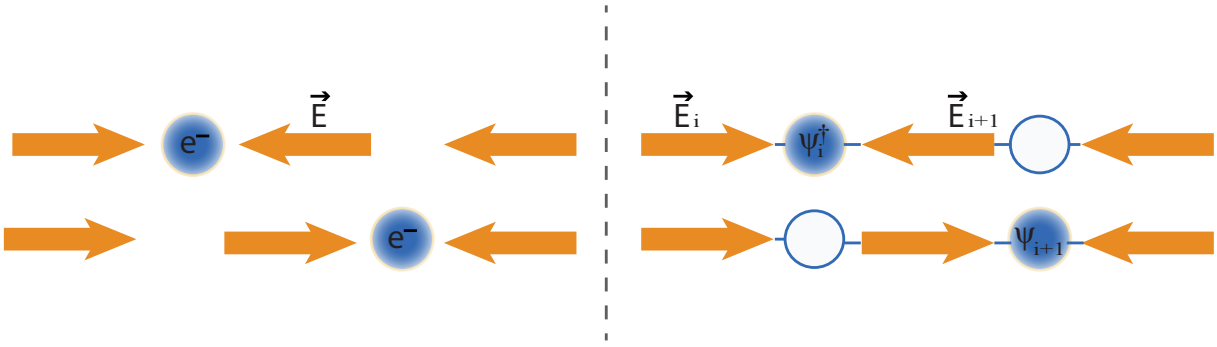

Figure 2.2: A simple depiction of Gauss'law. The scheme on the left illustrates the Gauss' law in classical electrodynamics. As shown on the upper line, the electric field lines (orange arrows) associated with the electron (blue circle) point inwards towards the charge; the lower line shows that a shift in the position of the electron causes the field to change accordingly. The scheme on the right is the lattice version, and the charge is replaced by a fermionic field operator as in QED. The charges lives on the lattice sites and the gauge field lives on the link connecting the two sites. The two field values E_i, and E_{i+1} are unequal if the charge is present on the site and their difference equals to one quanta. On the other hand, they are equal if the charge is absent.

Equation (2.29) has a very important implication and draws its nature directly from classical electromagnetism. It represents Gauss' law, i.e., the change of electric field associated with a moving charge; in this case, a hopping fermion across two lattice sites is always accompanied with link operators $U_n, U_n^\dagger$ causing a correlated increase or decrease in the value of the electric field on the link. The field thus has a dynamics of its own, which gives it the name *dynamical gauge field*. From equation (2.29), it follows that $[G_n, H] = 0$, which means that these generators are constants of motion and physical states are the ones that respect Gauss' law,

$$G_n \left|\psi_n\right\rangle = 0 \tag{2.30}$$

Implementing Gauss' law as described in equation (2.29) should be the first and foremost aim of any QS of HEP models, for that's what makes it a gauge theory. As it shall be seen in section 3.2, Gauss' law is implemented in an ultracold mixture via interspecies SCC.

2.3.2 Lattice QED

In the well known Kogut-Susskind formalism[62][78], the discretized Hamiltonian version of U(1) theory is given by

$$H_{KS} = \frac{a}{2}\sum_n E_n^2 + m\sum_n (-1)^n \psi_n^\dagger \psi_n - \frac{i}{2a}\sum_n (\psi_n^\dagger U_n \psi_{n+1} - h.c) \tag{2.31}$$

where a denotes the spacing of the real-space lattice[3]. Equation (2.31) describes QED in (1+1) space-time dimensions as it essentially stems from the conventional Dirac equation, which is the continuum description when the lattice spacing approaches zero. Comparing the above equation with (2.22), it can be observed that the hopping term is modified to include the local gauge invariance, as well as a pure gauge field term is added. Its quadratic expression stands for the energy contained in it.

The Dirac spinor is decomposed onto the neighbouring lattice sites in such a way that there are two separate fields for even and odd sites. The fermionic charge operator here is written as,

$$Q_n = \psi_n^\dagger \psi_n + \frac{(-1)^n - 1}{2} \tag{2.32}$$

The even sites contain *particles* and odd sites contain *anti-particles*. The latter basically corresponds to the absence of particles and is the analog of a filled *Dirac sea* in QED which is a theoretical interpretation of the negative energy solutions of continuum Dirac equation.
The link operator U_n and E_n acting between n^{th} and $(n+1)^{th}$ lattice site fulfill the commutation relations,

$$[E_n, U_m] = e\delta_{nm} U_m \quad ; \quad [E_n, U_m^\dagger] = -e\delta_{nm} U_m^\dagger \tag{2.33}$$

An alternative formulation of discretization is based on Wilson fermions[54][79]. The Hamiltonian is this case is given by,

$$H_W = \frac{a}{2}\sum_n E_n^2 + \left(m + \frac{1}{a}\right)\sum_n \psi_n^\dagger \begin{pmatrix} 0 & 1 \\ 1 & 0 \end{pmatrix} \psi_n + \frac{1}{a}\sum_n \psi_n^\dagger \begin{pmatrix} 0 & 1 \\ 0 & 0 \end{pmatrix} U_n \psi_{n+1} + h.c \tag{2.34}$$

where $\psi_n \to \sqrt{a_s}(-1)^n \psi_n$. The two components are then

$$\psi_n = \begin{pmatrix} \psi_{n,1} \\ \psi_{n,2} \end{pmatrix}. \tag{2.35}$$

obeying the anti-commutation relation $\{\psi n, \alpha, \psi n, \beta\} = \delta_{\alpha\beta}\delta_{nn'}$.

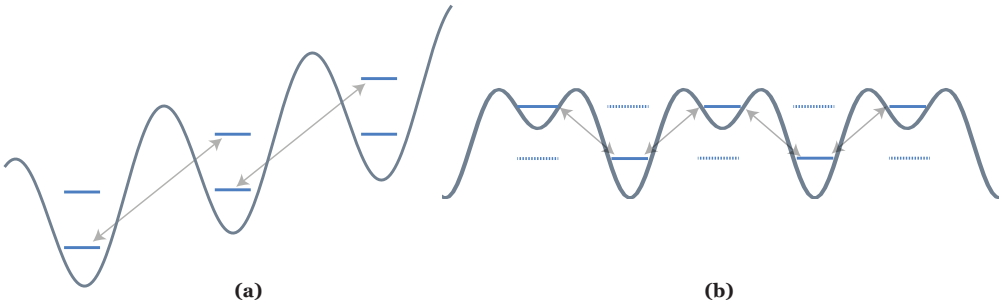

Figure 2.3: Implementation of U(1) LGT in an optical lattice: Staggered vs Wilson fermions. The grey patterns represent the lattice potentials. The blue lines are the internal states of matter particles. The grey arrows represent the coupling between the matter fields in different lattice sites, constituting a 1D chain. **(a)** optimized Wilson formulation in a tilted optical lattice. **(b)** staggered formulation, which experimentally demands an optical superlattice.

[3]It is not to be confused with the spacing of the optical lattice itself.

The major difference to the staggered formulation is that here two components of the Dirac spinor live on the same lattice site. This model thus realizes the same number of degrees of freedom in only half the space. Moreover, from an experimental perspective, staggered formulation typically requires an optical superlattice to engineer the alternating on-site energy[80], whereas the Wilson formulation proposes a tilted lattice as shown in figure, which could be technically less demanding. Detailed theoretical description and proposed implementation can be found in [81].

2.4 U(1) Quantum link model

Quantum link models were originally introduced in the context of HEP [58]. One of the major problems in experimentally implementing the U(1) gauge theory follows from the fact that the link operators are defined on an infinite dimensional Hilbert space. This is where the true essence of QLM lies, i.e., it maps the gauge fields defined on the links to a finite dimensional objects, whose dimensions are given by the number of bosonic atoms residing on a given link. This simplification strongly encourages one to use atomic systems as simulation platforms. In this approach, the gauge field is identified with the z-component of quantum spin operator $\hat{L}_{z,n}$ as,

$$E_n \rightarrow e\hat{L}_{z,n} \tag{2.36}$$

and the link operators are represented with the ladder operators $L_{\pm,n} = L_{x,n} \pm iL_{y,n}$,

$$U_n = [l(l+1)]^{-\frac{1}{2}} L_{+,n} \tag{2.37}$$

$$U_n^\dagger = [l(l+1)]^{-\frac{1}{2}} L_{-,n} \tag{2.38}$$

$$\tag{2.39}$$

where l denotes the magnitude of the spin vector $\vec{L}$. The spin operators obey the quantum mechanical commutation relation $[L_{i,n}, L_{j,m}] = i\delta_{nm}\epsilon_{ijk}L_{k,n}$, with $i, j, k = x, y, z$. The above substitution still preserves the originally discussed commutation relations given by (2.33). With l being finite in the QLM description, it is expressed by

$$[U_n, U_m^\dagger] = \frac{2\delta_{nm}E_m}{el(l+1)} \tag{2.40}$$

At the same time, (2.33) doesn't go to zero with a finite l, which perfectly supports the transition from a infinite dimensional case to the finite dimensional one. The QLM Hamiltonian is then given by

$$H_{QLM} = \frac{ae^2}{2}\sum_n \hat{L}_{z,n}^2 + \left(m + \frac{1}{a}\right)\sum_n \left(\psi_{n,1}^\dagger \psi_{n,2} + h.c\right) - \frac{1}{a\sqrt{l(l+1)}}\sum_n \left(\psi_{n,1}^\dagger L_{+,n}\psi_{n+1,2}\right) \tag{2.41}$$

It is this general version of the original Hamiltonian that enables the experimental implementation using ultracold atoms in optical lattices.

2.5 Ultracold $^{23}\mathrm{Na} - {}^{7}\mathrm{Li}$ mixture as a quantum simulator

The experimental system under consideration is comprised of two condensates, sodium and lithium, whose internal states $|F = 1, m_F = 1\rangle$ and $|F = 1, m_F = 0\rangle$ are manipulated

in order to engineer the constituents of U(1) theory. As outlined by QLM, the gauge field is mapped onto the sodium states, and the matter field onto lithium states. While the QLM Hamiltonian in equation (2.41) is the fitting description for implementation in an 1D optical lattice, the simulator realized in the $^{23}\mathrm{Na} - {}^{7}\mathrm{Li}$ experiment represents one building block of the extended model. In this section, theoretical description of this building block is presented, where the possible interactions among the four internal states of two species are discussed. Throughout this chapter, the indices N and L stand for sodium and lithium respectively. The first principle Hamiltonian of such a combined spin system is composed of *free* and *interaction* parts,

$$H = \underbrace{H_N + H_L}_{\text{free}} + \underbrace{H_{NN} + H_{LL} + H_{NL} + H_{scc}}_{\text{interaction}} \tag{2.42}$$

The free part of each species is given by,

$$H_s = \int_x \sum_\alpha \hat{\psi}^\dagger_{s,\alpha}(x) \left[\frac{-\nabla_x^2}{2m_s} + V_s(x) + E_{s,\alpha}(B_0) \right] \hat{\psi}_{s,\alpha}(x) \tag{2.43}$$

where $\hat{\psi}_{s,\alpha}$ and $\hat{\psi}^\dagger_{s,\alpha}$ are the field operators fulfilling

$$\left[\hat{\psi}_{s,\alpha}(x), \hat{\psi}^\dagger_{s,\alpha}(y) \right] = \delta_{ss'}\delta_{\alpha\beta}\delta(x-y) \tag{2.44}$$

with $\alpha, \beta \in \{0, 1\}$. The species index is denoted by $s \in \{N, L\}$, m_s denotes the atomic masses, V_s is the confining potential and $E_{s,\alpha}(B_0)$ is the single particle Zeeman shift in the presence of the magnetic field as given by the Breit-Rabi formula. The interactions are adequately described by the s-wave scattering length a. The interaction part of equation (2.42) is further divided broadly into two categories namely, inter-species and intra-species interactions. The intra-species part is given by,

$$H_s = \frac{1}{2} \int_x \left[g^s_{11} \hat{\psi}^\dagger_{s,1}\hat{\psi}^\dagger_{s,1}\hat{\psi}_{s,1}\hat{\psi}_{s,1} + g^s_{00}\hat{\psi}^\dagger_{s,0}\hat{\psi}^\dagger_{s,0}\hat{\psi}_{s,0}\hat{\psi}_{s,0} + 2g^s_{10}\hat{\psi}^\dagger_{s,1}\hat{\psi}^\dagger_{s,0}\hat{\psi}_{s,1}\hat{\psi}_{s,0} \right] \tag{2.45}$$

with

$$g^s_{jj} = \frac{4\pi\hbar^2}{m_s} a^s_{jj} \tag{2.46}$$

where a^s_{jj} is the reduced scattering length with $j \in \{0, 1\}$. Depending on whether the outgoing scattering state changes the internal state m_F, the inter-species interaction is further divided into non-spin changing and spin-changing collisions. The non SCC part is given by,

$$\begin{aligned} H_{NL} = \int_x \Big[& g^{NL}_{11}\hat{\psi}^\dagger_{N,1}\hat{\psi}_{N,1}\hat{\psi}^\dagger_{L,1}\hat{\psi}_{L,1} + g^{NL}_{00}\hat{\psi}^\dagger_{N,0}\hat{\psi}_{N,0}\hat{\psi}^\dagger_{L,0}\hat{\psi}_{L,0} + \\ & g^{NL}_{10}\hat{\psi}^\dagger_{N,1}\hat{\psi}_{N,1}\hat{\psi}^\dagger_{L,0}\hat{\psi}_{L,0} + g^{NL}_{10}\hat{\psi}^\dagger_{N,0}\hat{\psi}_{N,0}\hat{\psi}^\dagger_{L,1}\hat{\psi}_{L,1} \Big] \end{aligned} \tag{2.47}$$

with

$$g^{NL}_{jj} = \frac{2\pi\hbar^2}{\mu} a^{NL}_{jj} \tag{2.48}$$

where μ is the reduced mass, and a^{NL}_{jj} are again the reduced the scattering lengths for the non-spin changing interactions.

The last part is the spin-changing inter-species dynamics, which is of utmost importance when it comes to simulating the U(1) gauge theory and is given by,

$$H_{scc} = g^{scc} \int_x \left[\hat{\psi}^\dagger_{N,0} \hat{\psi}^\dagger_{L,1} \hat{\psi}_{N,1} \hat{\psi}_{L,0} + \hat{\psi}^\dagger_{N,1} \hat{\psi}^\dagger_{L,0} \hat{\psi}_{N,0} \hat{\psi}_{L,1} \right] \tag{2.49}$$

with

$$g^{scc} = \frac{2\pi\hbar^2}{\mu} a_{scc} \tag{2.50}$$

where a_{scc} is the reduced scattering length for the spin-changing collisions. The values for the different reduced scattering lengths are summarized in table 2.1.

2.5.1 Microscopic Hamiltonian

The description of the total system contains both spin-spin and density-density interactions. However the local gauge invariance principle is enforced through spin-spin interactions. To this end, the system is represented under *Single mode approximation(SMA)*, where the field operators are approximated with a single spatial mode of the BEC as,

$$\hat{\psi}_{s,\alpha}(x) \approx \Phi_{s,\alpha}(x) \hat{b}_{s,\alpha} \tag{2.51}$$

where $\Phi_{s,\alpha(x)}$ is the ground state wavefunction as determined by GPE. The Hamiltonian given in equation (2.42) can then be written as,

$$\begin{aligned} H_{SMA} = &\sum_s \left[\tilde{E}_{s,1}(B_0) \hat{b}^\dagger_{s,1} \hat{b}_{s,1} + \tilde{E}_{s,0}(B_0) \hat{b}^\dagger_{s,0} \hat{b}_{s,0} \right] + \\ &\sum_s \left[X^s_{11} \hat{b}^\dagger_{s,1} \hat{b}^\dagger_{s,1} \hat{b}_{s,1} \hat{b}_{s,1} + X_{00} \hat{b}^\dagger_{s,0} \hat{b}^\dagger_{s,0} \hat{b}_{s,0} \hat{b}_{s,0} + 2X^s_{10} \hat{b}^\dagger_{s,1} \hat{b}^\dagger_{s,0} \hat{b}_{s,1} \hat{b}_{s,0} \right] + \\ &X^{NL}_{11} \hat{b}^\dagger_{N,1} \hat{b}_{N,1} \hat{b}^\dagger_{L,1} \hat{b}_{L,1} + X^{NL}_{00} \hat{b}^\dagger_{N,0} \hat{b}_{N,0} \hat{b}^\dagger_{L,0} \hat{b}_{L,0} + X^{NL}_{10} \hat{b}^\dagger_{N,1} \hat{b}_{N,1} \hat{b}^\dagger_{L,0} \hat{b}_{L,0} + X^{NL}_{10} \hat{b}^\dagger_{N,0} \hat{b}_{N,0} \hat{b}^\dagger_{L,1} \hat{b}_{L,1} + \\ &X^{SCC} \hat{b}^\dagger_{N,0} \hat{b}^\dagger_{L,1} \hat{b}_{N,1} \hat{b}_{L,0} + X^{SCC} \hat{b}^\dagger_{N,1} \hat{b}^\dagger_{L,0} \hat{b}_{N,0} \hat{b}_{L,1} \end{aligned} \tag{2.52}$$

where

$$\tilde{E}_{s,\alpha}(B_0) = E_{s,\alpha}(B_0) + \int_x \Phi^*_{s,\alpha}(x) \left[\frac{-\nabla^2_x}{2m_s} + V_s(x) \right] \Phi_{s,\alpha}(x) \tag{2.53}$$

are the modified energy levels, $\hat{b}_{s,\alpha}$ and $\hat{b}^\dagger_{s,\alpha}$ represent the creation and the annihilation operators for the modes in the relevant spin states. The reduced interaction constants $X^s_{\alpha\beta}$ are calculated as

$$X^s_{\alpha\beta} = I^s_{\alpha\beta} \frac{g^s_{\alpha\beta}}{2}, \quad X^{NL}_{\alpha\beta} = I^{NL}_{\alpha\beta} g^{NL}_{\alpha\beta}, \quad X^{SCC} = I^{NL}_{10} g^{SCC} \tag{2.54}$$

from the relevant overlap integrals, which are given by,

$$I^s_{\alpha\beta} = \int_x |\Phi_{s,\alpha}(x)|^2 |\Phi_{s,\beta}(x)|^2 \tag{2.55}$$

$$I^{NL}_{\alpha\beta} = \int_x \Phi^*_{N,1} \Phi^*_{L,1} \Phi_{N,0} \Phi_{L,0} \tag{2.56}$$

$$I^{SCC} = \int_x \Phi^*_{N,1} \Phi^*_{L,1} \Phi_{N,0} \Phi_{L,0} \tag{2.57}$$

To further concentrate the description only on the spin dynamics of the system, a few more steps are employed. Firstly, the Schwinger Boson spin representation[82] is adapted as,

$$\hat{L}_{z,s} = \frac{1}{2}\left(\hat{N}_{s,1} - \hat{N}_{s,0}\right), \quad \hat{L}_{+,s} = \hat{b}^{\dagger}_{s,1}\hat{b}_{s,0}, \quad \hat{L}_{-,s} = \hat{b}^{\dagger}_{s,0}\hat{b}_{s,1} \tag{2.58}$$

Secondly, the total atom number is taken to be conserved,

$$\begin{aligned} \hat{N}_N &= \hat{N}_{N,1} + \hat{N}_{N,0} = const. \\ \hat{N}_L &= \hat{N}_{L,1} + \hat{N}_{L,0} = const. \end{aligned} \tag{2.59}$$

This is a valid under the approximation that s-wave collisions do not mix total hyperfine states of the colliding atoms, i.e., atoms do not leak to other states. Exploiting the above considerations, equation (2.52) can be segregated into the parts that contain spin operators and those which contain the number operators for the total atom numbers. (2.52). The free part of the equation (2.42) then translates to

$$H_s = \tilde{E}_{s,1}(B_0)\hat{N}_{s,1} + \tilde{E}_{s,0}(B_0)\hat{N}_{s,0} = \hat{N}_s\left[\frac{\tilde{E}_{s,1}(B_0) + \tilde{E}_{s,0}(B_0)}{2}\right] + \hat{L}_{z,s}\left[\tilde{E}_{s,1}(B_0) - \tilde{E}_{s,0}(B_0)\right] \tag{2.60}$$

To modify the interaction parts of the normally ordered equation given in (2.52), bosonic commutation relation $\hat{b}^{\dagger}_{s,1}\hat{b}^{\dagger}_{s,1}\hat{b}_{s,1}\hat{b}_{s,1} = \hat{N}_{s,1}(\hat{N}_{s,1} - 1)$ are employed. The resulting reduced interaction constants are,

$$\chi_s = X^s_{11} - X^s_{00} \tag{2.61}$$

$$\chi_{NL} = X^{NL}_{11} - X^{NL}_{00} \tag{2.62}$$

Using these definitions, the intra-species part of equation (2.52) is modified as,

$$\begin{aligned} H_{ss} &= X^s_{11}\hat{N}_{s,1}(\hat{N}_{s,1} - 1) + X^s_{00}\hat{N}_{s,0}(\hat{N}_{s,0} - 1) + 2X^s_{10}\hat{N}_{s,0}\hat{N}_{s,1} \\ &= \chi_s(\hat{N}_{s,1} - 1)\hat{L}_{z,s} - \chi_s\hat{L}^2_{z,s} + (X^s_{11} + X^s_{00} + 2X^s_{10})\frac{\hat{N}^2_s}{4} - (X^s_{11} + X^s_{00})\frac{\hat{N}_s}{2} \end{aligned} \tag{2.63}$$

and the inter-species part is modified as,

$$\begin{aligned} H_{NL} &= \left(X^{NL}_{11}\hat{N}_{N,1} + X^{NL}_{00}\hat{N}_{N,0}\right)\hat{N}_{L,1} + X^{NL}_{00}\left(\hat{N}_{N,1} + \hat{N}_{N,0}\right)\hat{N}_{L,0} \\ &= \frac{\chi_{NL}}{2}\hat{N}_N\hat{L}_{z,L} + \frac{\chi_{NL}}{2}\hat{N}_L\hat{L}_{z,N} + \chi_{NL}\hat{L}_{z,N}\hat{L}_{z,L} + \left[\frac{X^{NL}_{11} + 3X^{NL}_{00}}{4}\right]\hat{N}_N\hat{N}_L \end{aligned} \tag{2.64}$$

Finally, the SCC Hamiltonian becomes,

$$H_{SCC} = X^{SCC}\left[\hat{b}^{\dagger}_{L,1}\hat{L}_{-,N}\hat{b}_{L,0} + \hat{b}^{\dagger}_{L,0}\hat{L}_{+,N}\hat{b}_{L,1}\right] \tag{2.65}$$

The importance of equation (2.59) becomes apparent now, i.e., all the terms containing only the number operators can be dropped for further discussions.

Species	scattering length(red.)	value(a_B)
^{23}Na (intra-species)	a_{11}^N,a_{10}^N	55
	a_{00}^N	53
^{7}Li (intra-species)	a_{11}^L,a_{10}^L	12.5
	a_{00}^L	6.8
$^{23}\mathrm{Na} - {}^{7}\mathrm{Li}$ (inter-species)	a_{11}^{NL}	20
	a_{00}^{NL},a_{10}^{NL}	19.65
	a_{scc}	0.35

Table 2.1: Values of reduced scattering lengths for all possible scattering channels of $^{23}\mathrm{Na} - {}^{7}\mathrm{Li}$[31, 83, 84]. The desired states for the experimental implementation are the hyperfine states $|F=1, m_F=1\rangle$ and $|F=1, m_F=0\rangle$ of both the species. Different possible s-wave scattering channels include intra-species, and interspecies interactions.

2.5.2 Effective spin Hamiltonian

The derivation presented in section 2.5.1 results in a Hamiltonian containing terms with spin operators,

$$\begin{aligned} H_{spin} = &\left[E_{N,1}(B_0) - E_{N,0}(B_0) + \chi_N(\hat{N}_N - 1) + \frac{1}{2}\chi_{NL}\hat{N}_L\right]\hat{L}_{z,N} - \chi_N\hat{L}_{z,N}^2 \\ &+ \left[E_{L,1}(B_0) - E_{L,0}(B_0) + \chi_L(\hat{N}_L - 1) + \frac{1}{2}\chi_{NL}\hat{N}_N\right]\hat{L}_{z,L} - \chi_L\hat{L}_{z,L}^2 \\ &+ \chi_{NL}\hat{L}_{z,N}\hat{L}_{z,L} + H_{SCC} \end{aligned} \tag{2.66}$$

Even though the above Hamiltonian greatly simplified, it is still ambiguous when it comes to relating it with the cold-atom QED description as in equation (2.41). Hence, it is further modified by making use of yet another expression for the total magnetization,

$$\hat{M} = \hat{L}_{z,N} + \hat{L}_{z,L} \tag{2.67}$$

The equation (2.66) then becomes,

$$H_{spin}/\hbar = \chi\hat{L}_{z,N}^2 + \hat{\Delta}\hat{L}_{z,L} + \lambda\left(\hat{L}_{-,N}\hat{L}_{+,L} + \hat{L}_{+,N}\hat{L}_{-,L}\right) \tag{2.68}$$

where

$$\chi = -\chi_N - \chi_L - \chi_{NL} \tag{2.69}$$

$$\begin{aligned} \hat{\Delta} = &[E_{L,1}(B_0) - E_{L,0}(B_0)] - [E_{N,1}(B_0) - E_{N,0}(B_0)] + \\ &\chi_L(\hat{N}_L - 1) - \chi_N(\hat{N}_N - 1) + \frac{1}{2}\chi_{NL}(\hat{N}_N - \hat{N}_L) + 2\hat{M}\left(-\chi_L - \frac{1}{2}\chi_{NL}\right) \end{aligned} \tag{2.70}$$

$$\lambda = X^{SCC} \tag{2.71}$$

Using the Schwinger boson representation on $\hat{L}_{z,L}$, equation (2.68) can be rewritten as,

$$H_{spin}/\hbar = \chi\hat{L}_{z,N}^2 + \frac{\hat{\Delta}}{2}\left(\hat{b}_{L,0}^\dagger\hat{b}_{L,0} - \hat{b}_{L,1}^\dagger\hat{b}_{L,1}^\dagger\right) + \lambda\left(\hat{b}_{L,0}^\dagger\hat{L}_{-,N}\hat{b}_{L,1} + \hat{b}_{L,1}^\dagger\hat{L}_{+,N}\hat{b}_{L,0}\right) \tag{2.72}$$

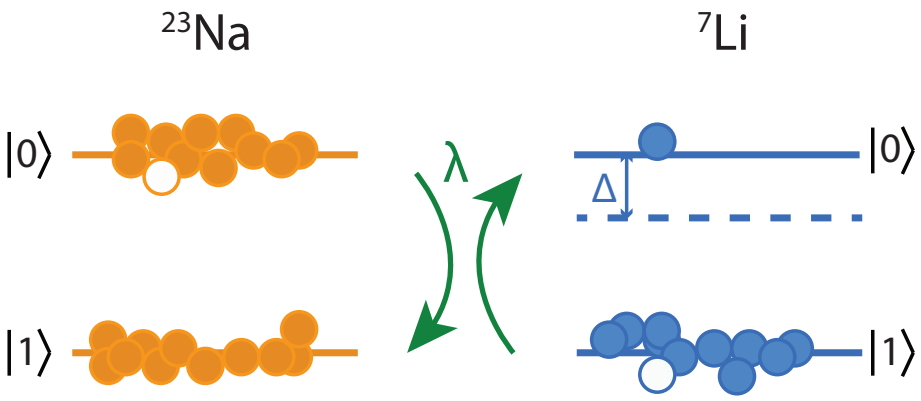

(a) The process of SCC between ^{23}Na and ^{7}Li.

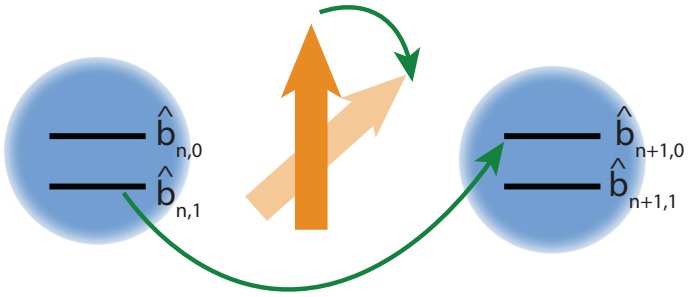

(b) Visualization of SCC in a single building block.

Figure 2.4: Pictorial representation of Hamiltonian presented in (2.72). **(a)** dynamics of inter-species spin changing collisions. The hyperfine states of ^{23}Na are populated with desired superposition, thus creating an $\hat{L}_{z,N}$ term. It is associated with χ, a combination of intra-species interaction strengths of ^{23}Na and ^{7}Li as described in equation (2.69). The detuning Δ signifies the shift the hyperfine energy level due to several effects: Zeeman shift due to the applied the magnetic field, collective mean field shifts from the atoms, shifts from a changing magnetization. The strength of the SCC itself is described by λ, which only depends on the extent of the spatial overlap between the two clouds. **(b)** lattice equivalent description of SCC dynamics shown in (a), on a single building block of 1D LGT. The two species are trapped together in the same confining potential. According to QLM, the two sodium states comprise the gauge field term and are represented as an effective spin (orange arrow) via Schwinger boson representation. The two lithium states describe components of the matter field as in the Wilson representation of QED. Even though the SCC dynamics takes place in the bulk BEC, it can be interpreted as a single unit of the lattice, that comprises the 1D chain. One component of the matter field is mapped onto one site ($\hat{b}_{n,1}$), and the other component to the next site ($\hat{b^{\dagger}}_{n+1,0}$) while the collective sodium spin acts as the link. Hence, the Gauss' law is manifested in the form of SCC process, where a lithium atom hop from one site to the next, with the effective sodium spin simultaneously changing its orientation on the link.

The above Hamiltonian is particularly useful to visualize the process of correlated hopping as in the quantum link Hamiltonian in equation (2.41). It is equivalent to the two adjacent lattice sites, where the two components of the matter field live respectively as $\hat{b}_{L,0} = \hat{b}_{n+1,0}$ and $\hat{b}_{L,1} = \hat{b}_{N,1}$. $\hat{L}^2_{z,N}$ gives the gauge field dynamics; the spin changing collision term then incorporates the local gauge invariance. The Gauss law operators now are,

$$\hat{G}'_n = \hat{L}_{z,N} + \hat{b}^{\dagger}_{L,0}\hat{b}_{L,0} \quad ; \quad \hat{G}'_{n+1} = \hat{L}_{z,N} + \hat{b}^{\dagger}_{L,1}\hat{b}_{L,1} \tag{2.73}$$

2.5.3 Coupled spin picture on the Bloch sphere

QLM provides a descriptive interpretation of the underlying principle of U(1) LGT. As all the processes are described using spin operators, the Bloch sphere representation can be adapted. This serves as a powerful visualization tool, as all the terms in the Hamiltonian are essentially rotations of the spin vectors. Consider the two basis states of the a spin-1/2 system to be $|\uparrow\rangle$ (spin up) and $|\downarrow\rangle$ (spin down) states. In general, all possible superpositions of these two states can be written as,

$$|\theta, \phi\rangle = \cos\frac{\theta}{2}|\uparrow\rangle + \sin\frac{\theta}{2}e^{i\phi}|\downarrow\rangle \tag{2.74}$$

and can be parametrized by the two angles, $\theta = [0, \pi]$ and $\phi = [0, 2\pi]$. A superposition state can then graphically represented on a sphere called the *Bloch sphere*, as shown in Fig. 2.5. Any unitary transformation can then be pictured as a rotation of the Bloch vector[85].

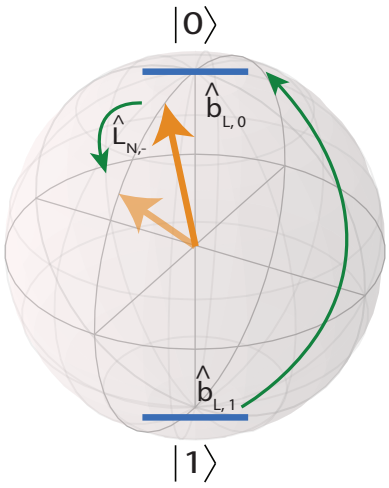

Figure 2.5: Representation of the SCC on the Bloch sphere. The generalization of a spin-S system to a spin-1/2 system provides a geometric description of spin algebra in the form of a unit sphere characterized by a polar angle θ and azimuthal angle ϕ. Only, instead of a traditional single spin vector, here it is a collective spin(orange arrow), whose value is $N/2$. The gauge field is the projection onto the z-axis. The two internal spin states of lithium are situated at the poles and represented $|F = 1, m_F = 1\rangle \rightarrow |1\rangle$ and $|F = 1, m_F = 0\rangle \rightarrow |0\rangle$. During SCC, lithium atoms transfer from $|1\rangle$ to $|0\rangle$. It is accompanied by the simultaneous lowering of the sodium L_z by one unit upon the action of the link operator $L_{N,-}$

They are generated by the spin-1/2 Pauli matrices, which fulfill the SU(2) commutation relations[86]. A spin-1/2 representation can be generalized to a spin-S system with the concept of a *collective spin*[87][88]. For an assembly of N particles, each with spin 1/2 and all directed long the same axis, the total spin of the system is given by $L = N/2$. This perfectly explains the scenario of the $^{23}\mathrm{Na}-{}^{7}\mathrm{Li}$ mixture, where the available states of the ground state hyperfine manifold $m_F = \{0, 1\}$ are populated by the condensed atoms and the $\hat{L}_{z,n}$ is also effectively given in terms of population imbalance via Schwinger boson representation. The Hamiltonian (2.68) can then be interpreted as that of two coupled spins of sodium and lithium and can be rewritten as

$$H/\hbar = \chi\hat{L}_{z,N}^2 + \hat{\Delta}\hat{L}_{z,L} + 2\lambda\left(\hat{L}_{x,N}\hat{L}_{x,L} + \hat{L}_{y,N}\hat{L}_{y,L}\right) \tag{2.75}$$

The pure gauge field term $\chi \hat{L}_{z,n}^2$ indicates that the sodium spin rotates in the x-y plane whose speed of rotation is given by $2\chi L_{z,N}$. Thus, it depends on the relative imbalance of the two hyperfine states, and higher the imbalance, the faster it rotates. The matter field term also describes a similar rotation of lithium spin, but with a speed specified by $\hat{\Delta}$. The process of spin changing collision is then seen as a resonance that occurs when the two spins are co-rotating,

$$2\chi \hat{L}_{z,N} \approx \hat{\Delta} \tag{2.76}$$

If the two rotation frequencies are substantially different, they keep on rotating completely uncorrelated, and hence the strength of their coupling averages out.

2.6 Summary

- In this section, the basic concepts of non interacting and weakly interacting Bose gases was presented. Starting from statistical description of an ideal Bose gas, the emergence of a BEC was described, along with brief explanations of its parameters, such as condensate fraction, temperature and density profiles in the case of a harmonic confinement.
- The concept of local gauge symmetry in the context of LGT was introduced. It was seen that the gauge transformations on a lattice depend on the position of the lattice site, and hence, the Hamiltonian doesn't remain the same under transformation. As a means of restoring the principle of local gauge invariance, which is an indispensable property of a HEP model, gauge fields were introduced on the links connecting the two lattice sites. The concept of U(1) LGT was introduced in context of QED in (1+1) dimension, using Kogut-Susskind formalism. Furthermore, it was shown that there exist alternative methods such as Wilson formulation, which is better suited for simulating QED using ultracold atoms in an optical lattice. In either cases, the mapping of the HEP version onto a cold atom version was established by QLM, in which the link operators are described by spin operators, and the gauge field itself is mapped onto the z-projection of sodium spin. Overall, it was shown that the U(1) LGT can indeed be implemented in a system of ultracold mixtures, by enforcing the Gauss' law in the form of heteronuclear SCC.
- The model was subjected to a rigorous mathematical treatment based on mean field GPE. Considering the properties of two species such as spatial extent, scattering lengths, and their behavior in an external magnetic field, different channels of interactions were outlined. The QLM Hamiltonian was re-written as an effective, coupled spin model, in terms of spin operators and it was shown that it is characterized by three important parameters namely χ, $\hat{\Delta}$ and λ.

Chapter 3

Experimental methods

This chapter focuses on the experimental methods involved in realizing an ultracold mixture of $^{23}\mathrm{Na}$ and $^{7}\mathrm{Li}$. Atomic vapors of both gases are cooled and trapped using various techniques such as magneto-optical trap (MOT), magnetic trap and optical dipole trap (ODT). In the first part of this chapter, the experimental system is described consisting of two major sections: i) The laser table, where the laser beams are manipulated in frequency, power and polarization, ii) The experimental chamber comprised of an atomic source, vacuum system and a science chamber. The setup as a whole was constructed long before the research presented in this thesis[89, 90, 91, 92, 93]. However, certain parts either had to be updated or replaced due to downgraded performance. There were two major changes in this regard, of which the first one was the replacement of the experimental control system. The different parts of the new control system and their functionalities are briefly explained in this chapter. The second change was the replacement of the atomic source itself. An overview of the crucial steps involved in creating two condensates is presented. Moreover, as the setup was subjected to upgrades and hardware replacements soon after the data acquisition from SCC experiment, all these steps had to be re-established. The final part of the chapter is devoted to the description on how the different internal states of the condensates can be manipulated with the help of Radio-Frequency (RF) and Microwave (MW) pulses. At the very end, the first results of SCC measurements are presented, along with the related aspects such as data acquisition method and detection techniques. Special emphasis is given to the raw data itself, where it was seen that the SCC measurements exhibit fluctuations.

3.1 Pathway to a mixture BEC

This section describes the experimental procedures involved in achieving the quantum degeneracy of the Na-Li mixture. The experiment takes place in an ultra-high vacuum (UHV), thereby well isolated from the environment. A heated dual species atomic source called the oven, supplies the sodium and lithium atoms. As a preliminary step in achieving the BECs, the method of laser cooling and trapping is employed in the form of a Zeeman slower and MOT, whereby the hot atoms effusing from the oven are cooled and subsequently captured. The associated optical setups are briefly described. The process of achieving condensation of atoms trapped in the MOT comprises of highly controlled and sequential stages aimed at reducing the temperature of the sample of atoms as well as increasing the phase space density. Standard absorption imaging technique is used throughout to benchmark the different stages. All these processes are addressed briefly in the following sections.

3.1.1 Vacuum system

The vacuum system of the Na-Li experiment is comprised of four major sections: a dual species source of atoms, pumping stage, the glass cell (science chamber) and finally the rear part consisting of a turbo-molecular pump. While several components and parts of the vacuum system have changed over the course of years, the overall setup remains the same. This section gives only a brief overview of the most important parts. A detailed account on the vacuum setup can be found in[93][90].

Dual species oven

The underlying design of the oven used in the Na-Li experiment is largely based on [94]. A detailed description on the technical aspects of its designs and functionality can be found in [95][90]. This type of oven features two chambers that act as reservoirs of the atomic species, followed by an oven nozzle and a mixing nozzle. The solid chunks of sodium and lithium in the reservoirs are independently heated to produce atomic vapors. Typical operating temperatures are 320°C for sodium and 380°C for lithium. They are reduced to 250°C (Na) and 280° (Li) during the night, when the experiment is on standby. The two oven chambers are connected by a small tube called the mixing nozzle. It is heated to 450°C indefinitely to avoid sodium deposition. The oven nozzle is yet another a small tube of mixing chamber to the final part of the oven, the collimation chamber with an exit hole. The oven nozzle and the exit nozzle function together to facilitate the collimation of the atomic beams when they exit the oven. The oven nozzle is also heated to 450°C.

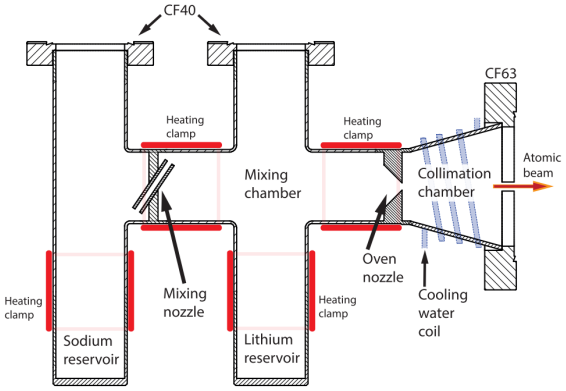

Figure 3.1: Dual species oven. It features two separate chambers for sodium and lithium. The cups containing the solid metal chunks are heated in order to produce the atomic vapors of sodium and lithium. Image taken from [93].

The SCC experiment was carried out while this oven was still functioning with ample amounts of sodium and lithium. It got depleted after few months, resulting in a heavily reduced flux. Due to the fact that the atoms used in the experiment once are not recycled in any form, lifetime of such an atomic source is limited. Historically, typical operation time of a fully filled Na-Li oven has been about one year or slightly more, depending on the operating temperatures. During the course of this thesis, the oven had to be replaced[92][93].

Pumping stage

This stage is physically located right next to the oven, and can be broadly divided into two parts, namely, an oven chamber and a pumping stage chamber. The oven chamber comprises of a 6-way cross and an ion pump[1]. The two chambers are connected by the 6-way cross, whose rear arm is connected to the back stage. The pumping stage comprises of a 4-way cross, and another ion pump(Agilent Starcell Valcon 55). A differential pumping tube connecting the two chambers causes a pressure difference by a factor of 100; the oven pump region typically operates at a pressure of $\approx 10^{-8}$ mbar, while the Starcell region stays at $\approx 10^{-10}$ mbar.

Glass cell/UHV chamber

This region forms the second half of the vacuum setup, where the atoms are captured. A differential pumping tube connects it to a bellow, to facilitate the centering the atomic beam onto the MOT position. A gate valve isolates the glass cell from the rest of the vacuum system[2]. An ion pump is connected to the glass cell, and reduces the pressure to $\approx 10^{-11}$ mbar, which is good enough for any kind of cold atom experiment. An ion gauge monitors this pressure indefinitely. Finally, the far end of the vacuum system is closed with a view port. This spot is highly prone to alkali deposition. Hence, it is heated at 150°C continuously.

Rear vacuum

The first 6-way cross connecting the oven and the pumping stage also connects to the back part of the vacuum system through its rear opening via an angle valve. The venting procedure during vacuum operations is undertaken here, and it is the first stage of towards achieving UHV. A turbo-molecular pump, in combination with a roughing pump reduce the pressure up to a maximum of 10^{-8} mbar. Furthermore, with a provision to connect a pressure gauge and a residual gas analyzer, it forms the first diagnostic stage. Once the desired pressures are reached everywhere and the system is ready to run the experiment, the rear part is closed off and only ion pumps at the front are responsible for maintaining the UHV pressure throughout.

3.1.2 Laser table and spectroscopy

In any ultracold experiment, the first stage of temperature reduction involves the techniques of laser cooling and trapping. These methods rely on precise control of the laser light. Moreover, the laser frequencies need be stabilized prior to the cooling itself. Typically, this is achieved by locking the laser frequency to that of an appropriate atomic transition. The Na-Li experiment uses one of the most commonly used methods of laser stabilization called Doppler-free saturated absorption spectroscopy[96]. This method relies on saturated absorption principle and is particularly employed to circumvent the problem of Doppler-broadening of the atomic transition and enable a narrower spectrum, and hence more precise frequency standard. In its simplest realization, it consists of a laser beam split into two counter-propagating, generally called the *pump* and *probe* beam, with differing intensities. At the atomic resonance

[1]During the oven change, the position of the oven pump was shifted from the bottom arm of the 6-way cross to its left side arm. This was motivated by an incident where fine sodium powder was found inside the pump during bake-out, allegedly causing it to malfunction.

[2]It was particularly helpful during vacuum operation of oven change, where it was crucial not to let the glass cell expose to the region with higher pressure.

frequency, i.e., for the atoms in the zero velocity class, the pump beam saturates the transition, leaving little to absorb for the probe. Thus, whenever the pump beam is present, the absorption from the probe beam reduces giving rise to a dip in its Doppler broadened signal.

Sodium

Sodium atoms are laser-cooled using a commercial laser (TOPTICA TA-SHG Pro). As the name indicates, it functions based on the principle of second harmonic generation[97]. It broadly features two sections: the first one comprises of a master laser (1178 nm) which is a tunable laser diode, followed by a high power tapered amplifier (TA), that is seeded by the master. The second part is a frequency doubling stage, where it produces the laser light at 589 nm at an optical power of $\approx$ 1.3W. The in-coupling mirrors into the TA and the SHG cavity are equipped with piezo actuators for the purpose of auto-alignment.[3] Parameters like laser current and temperature are interdependently controlled for both the master and the TA. The final wavelength can be tuned mainly by changing the master laser current, piezo voltage and the temperature.

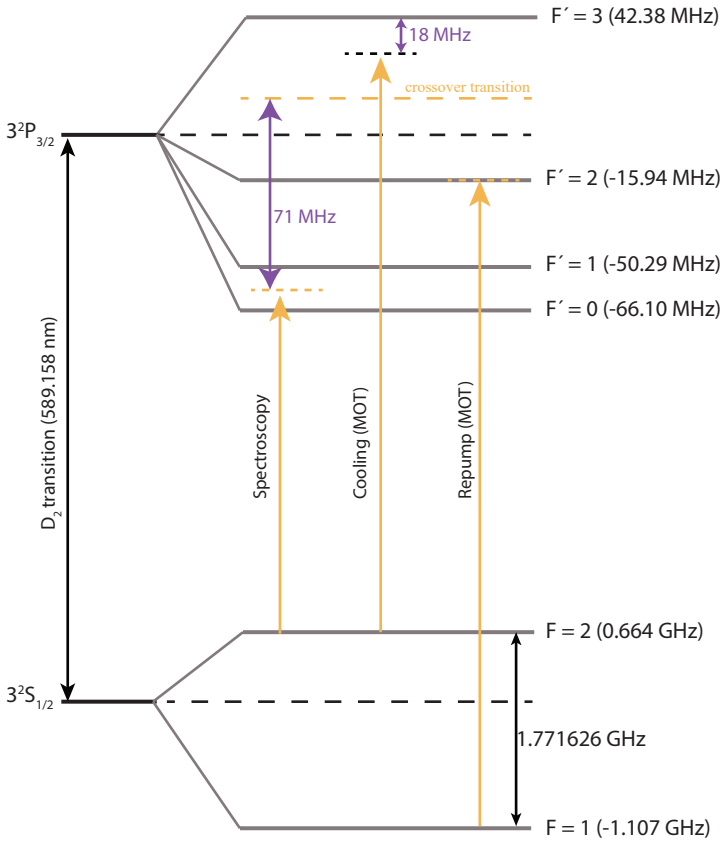

Figure 3.2: Energy level diagram for ^{23}Na. The laser cooling and trapping relies on the sodium D2 spectral line. The hyperfine transitions shown here serve as cooling and repump transitions for the MOT. The spectroscopy is done on the excited crossover resonance of $F = 2 \rightarrow F' = 3$.

The spectroscopy is performed by locking the laser to the $F = 2 \rightarrow F' = 3$ excited

[3]There were instances when the auto-alignment did not improve the in-coupling and hence the alignment had to be performed manually. In that case, the piezo actuator arms should be loosened and beam-walking should be performed to get the maximum power output.

crossover transition of the sodium D2 line. The spectroscopy setup is composed of a standard pump and probe beams passing through a sodium cell. The frequency of the pump beam is shifted by a 71 MHz AOM in its +1 order in double pass configuration. The spectroscopy signal is obtained by directly monitoring the probe beam a photo-diode. The locking signal is then generated with the help of a lock-in amplifier in the following manner: the spectroscopy AOM is modulated via a function generator with a 21 KHz sinusoidal signal, which also serves as a reference signal to the lock-in amplifier. Taking the spectroscopy signal as the input, it generates an error signal which is then fed to a standard PI (proportional-integral) controller. With optimized PI parameters, the laser is locked to the zero crossing of the error signal corresponding to the crossover transition. Detailed description of the schematics can be found in [90].

Lithium

The optical setup for lithium is equipped with provisions to cool and trap both the isotopes, ^{7}Li and ^{6}Li, as many projects in the past dealt with ^{23}Na-^{6}Li mixture[98]. However, given the context of this thesis, only ^{7}Li is addressed. The overall laser system is comprised of three lasers:

Master laser: This laser is solely used for spectroscopy. During the course of this thesis, the existing setup given in[99] was slightly modified, where a previously used home-built diode laser (ECDL) was replaced by a tunable commercial laser (TOPTICA DL Pro, 28 mW, 671 nm). Fig. 3.5 shows the modified setup. To eliminate the use of excess optics and increase stability, a commercial fiber-coupler called FiberDock was installed at the output port of the laser. It has an integrated coupling lens, and is equipped with alignment screws for a standard fiber coupling procedure[100].

TA Pro: This is used to generate the MOT, slower, and the beams required for optical pumping during spin polarization (see section 3.1.4). A commercial laser (TA Pro) was used for this purpose. During the course of this thesis, its TA chip degraded, and hence the TA unit had to be replaced by a new one followed by a re-alignment of the whole laser. It provides a total specified power of 0.5W[4]). The laser head also features a rear output with an output power of couple of mW, which is used for locking it using the offset-lock method.

Home-built TA: The ground state splitting of 803 MHz ^{7}Li required an additional AOM in double pass configuration to be added to the repumper beam. Following the low diffraction efficiency in this double pass and consequently a lack of available optical power, an additional TA setup was built[101]. It is seeded by the light generated by TA Pro $\approx$ 50 mW and outputs a total power of $\approx$ 280 mW. A detailed discussion on power requirements and detunings are found in[93].

[4]Specified power on the data sheet. The mode however is not perfectly Gaussian, and about 7-10% of the total power is not usable, leaving $\approx$ 350-400 mW for practical use.

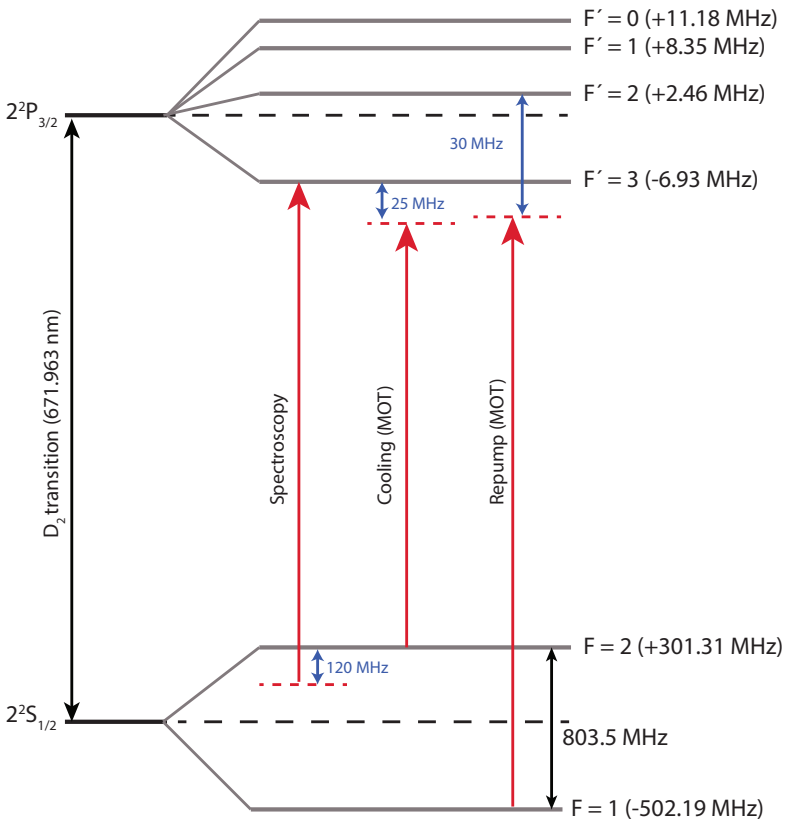

Figure 3.3: Energy level diagram for ^{7}Li with detunings of spectroscopy, cycling and repump transitions for MOT. The cooling and trapping is performed on D2 line at 671.963 nm. The spectroscopy signal is locked onto $F = 2 \rightarrow F' = 3$ with the laser being blue detuned by 120 MHz with respect F=2.

The lithium spectroscopy cell is home-built, containing both ^{7}Li and ^{6}Li[99]. The heating of the cell is regulated by a temperature control setup consisting of a K-type thermocouple, a commercial thermocouple amplifier circuit(ADAFRUIT, AD8495), an arduino YUN, and NS-80 phase-angle dimmer, and a band heating clamp. While the extent of the heating provided by the heater is externally controlled by NS-80, the dimmer itself also contains an input provision to be controlled. The thermocouple in combination with the amplifier, monitors the temperature continuously. The amplified voltage [5] is then fed to the analog input of the arduino[6], which is programmed to be a PID controller. The operating temperature of the cell is the set-point of the PID and is specified in the .ino script along with the rest of the parameters needed for temperature control. The arduino PID generates an internal error signal, and sends out the control signal to NS-80, which then regulates the heating of the cell accordingly. The cell is heated to 450°C during normal operation, and reduced to 350°C at night, when not in use. More information on the characterization of the spectroscopy setup is given in [99].

[5]Voltage to temperature conversion is given by temperature, T = $(V_{out} - 1.25)/0.005V$. The range of measurement is -250°C to +750°C (powered with 5V DC) and -250°C to +410°C (powered with 3.3V DC).

[6]When the setup was first installed, the PID regulation was done using Arduino UNO, but was later replaced by YUN simply for technical convenience. While the UNO boards require a serial to USB cable for control, YUNs can be accessed over Ethernet.

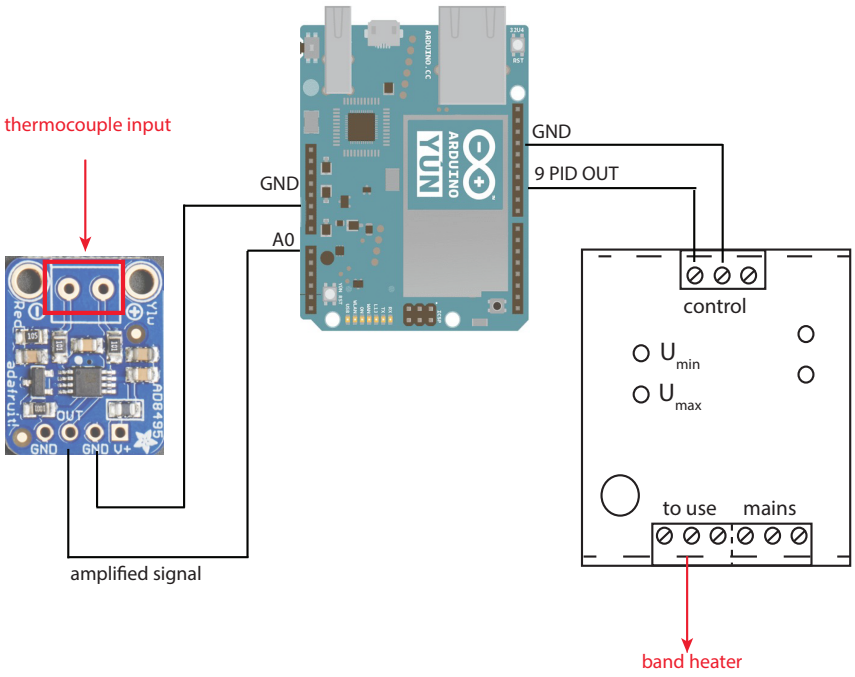

Figure 3.4: Simplified diagram of Li-temperature control. Heating of the spectroscopy cell is controlled by NS-80, which is a phase angle dimmer and it is controlled using an external control voltage. A K-type thermocouple attached to the spectroscopy cell(not shown in the figure) monitors the temperature. This signal is amplified using the thermocouple amplifier board(shown in red) and sent to the analog input A0 of Arduino YUN, whose task is to perform the control action. The PID generates the error signal and subsequently the control voltage required for the NS-80.

The Doppler free spectroscopy is carried out for lithium in the same way as it is done in the case of sodium. The pump beam is shifted in frequency by a 120 MHz AOM in -1 order, and double pass configuration. The TA Pro on the other hand, is locked by an offset lock, sometimes also called the beat lock. The general idea of this method is to overlap two laser beams of similar frequency, polarization and power onto a photo-diode and obtain their beat signal, which is further processed electronically with the help of a feedback loop[102]. The detailed implementation and characterization of the offset lock is found in [103]. Slight changes were made to the setup described therein. The original setup used a combination of beam splitters to overlap the beams from the master and the TA Pro. In the revised setup, the beam-splitters were replaced by a fused Fiber Optic Coupler (Thorlabs, TN670R5A2) that consists of four fibers, two for input and two for output. The two beams to be manipulated are coupled to the input ports, and the coupler combines them with a splitting/mixing ratio of 50:50, see Fig. 3.5. The resulting beat signal is then monitored on a photo-diode. Upon further mixing it with a stable reference from a local oscillator[7], an error signal is generated, whose zero-crossing can be used as a lock point. In the MOT phase, it corresponds to an offset of 65 MHz. Lithium also goes through a compressed MOT stage (see section 3.1.3) to increase the density during which the offset lock frequency changes to 45 MHz.

[7] A voltage controlled oscillator is used for this purpose.

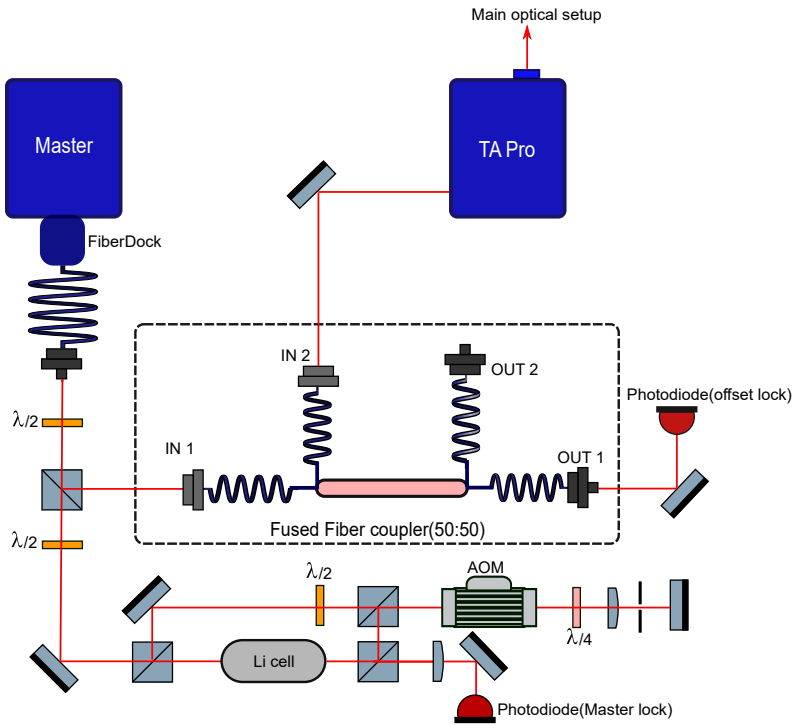

Figure 3.5: Schematics of the updated spectroscopy setup of ^{7}Li. Li cell is heated to 450°C under normal operation. The master is locked to the transition $F = 2 \rightarrow F' = 3$ via saturated absorption method. The pump beam and hence the laser frequency is shifted down by 120 MHz with respect to $F = 2$. The laser beams from the master and TA pro are combined using a fused fiber coupler to produce a beat signal. Subsequently, it is processed in an electronic setup to generate an error signal.

3.1.3 Zeeman slower and MOT

The deceleration of the atomic beams is typically the first step to be undertaken when it comes to laser cooling[104]. It can be accomplished with either a 2D MOT, or a Zeeman slower[105]. The Na-Li experiment uses a dual species spin-flip Zeeman slower that features a big slower coil and a small slower coil. Any excess gradient created by the slower coils is counteracted with the help of another coil called the compensation coil. The design and implementation of the slower is found in [106]. The laser beam that cools the atomic beam from the oven is called the slower beam. Sodium setup consists of one slower beam ($\approx$ 90 mW) and the same is modulated with an EOM to produce side-bands needed for the repumper transition. The EOM operates at a frequency of 1713 MHz. The lithium setup features two separate slower beams for cycling and repump transitions. A CCD camera (Allied Visions GUPPY[8]) is mounted against a viewport next to the glass cell which monitors the fluorescence emitted by the atoms that interact with the slower beam. A typical raw image of slower fluorescence of sodium as seen by Guppy is displayed below in Fig. 3.6[9]. This was particularly useful for a quantitative assessment of the slower alignment; the fluorescence was quantified by taking two images, one with fluorescence, followed by a reference picture[10]. The latter was acquired

[8] It is controlled via a software called Vimba Viewer.

[9] Such a clear atomic signal was never obtained for lithium. Hence, only sodium was used to benchmark the camera counts.

[10] As the reference image should contain the same amount of light, but no fluorescence, the slower coil current was reduced to zero.

to cancel the contribution of stray light or reflections, which could be mistaken for fluorescence counts. A minimal python script was then used to calculate the counts in arbitrary units, by subtracting the two pictures. Even though this is a rather simplistic method, it proved vital in troubleshooting, especially when the oven started showing the signs of depletion.

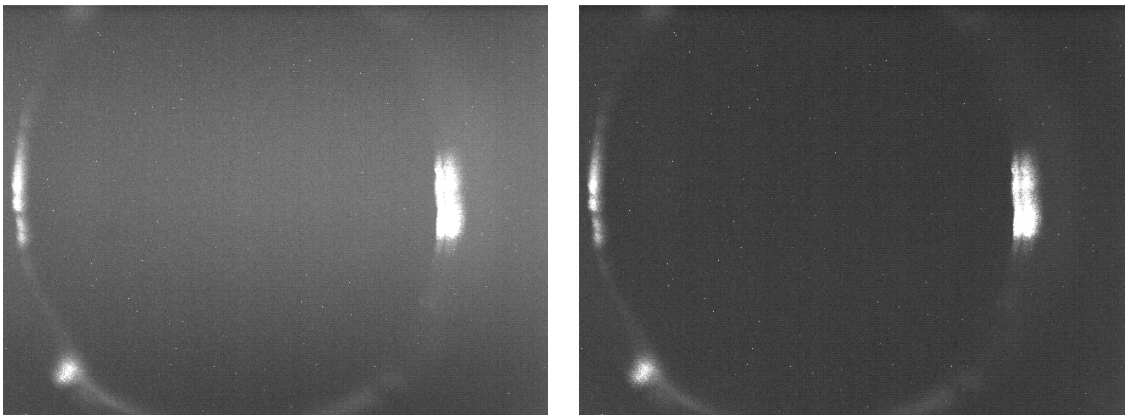

(a) F luorescence image **(b)** Reference image

Figure 3.6: Raw images of slower fluorescence of sodium. (a). Image with fluorescence taken after a few months of oven filling, with the oven being heated to 280°C. The central grey hue marks the collected fluorescence. With an appropriate value of current through the slower coil, and a stable laser lock, a maximized fluorescence stands for the best possible alignment. **(b).** Reference picture, where the slower coil is off. In both the pictures, the central, bright round structure is the reflection of the light at the boundaries of the viewport.

The decelerated atoms fly towards the MOT, where pairs of counter-propagating beams with circular polarization are crossed at the center of a quadrapole field. The MOT gives rise to a velocity frictional force that cools the atoms, and a position-dependent radiation pressure to trap them[107]. In the Na-Li, a dual species MOT is devised. The magnetic field gradient is generated with a pair of coils called antibias and curvature (see 3.1.4). There are six beams in total for each species, namely upper, lower, front and back beams. Upper and lower ones are retro-reflected to form four beams. Front and back beams are separately installed and are counter propagating. For both species, they are red-detuned using appropriate AOMs with respect to the cycling transitions shown in Fig. 3.2 and Fig. 3.3. The frequency shifts enforced on the different beams is found in table 3.1. Furthermore, MOT beams of both species are coupled into common fibers before being guided onto the main experimental table. The lithium setup consists of additional four repumper beams and are coupled through the same fibers used for the MOT. Repumping in sodium on the other hand, is carried out with only one beam. The large frequency shift needed for this is achieved with the help of so called big AOM (TEF-1700-100-589, Brimrose Corp) in its +1 order, spanning 1.7 GHz. Its diffraction efficiency lies in the range 5-10%. This beam is further coupled into two more paths, the final repumper beam and umpump repumper beam, required for spin purification (see section 3.1.4). In depth explanations about optical layouts are provided in [90][98].
Both the MOTs employ two different techniques to increase their initial density. A dark spot MOT is employed for sodium, wherein the repumper beam is shone through a central black spot into the glass cell[108]. In the case of lithium, the MOT is compressed, right before the spin polarization process. Typical loading times in the sequence are 8s and 16s for Na and

Li respectively.[11] In a typical BEC experiment, lithium is loaded first, followed by sodium. This is because lithium MOT loads much slower compared to sodium, however it is blessed with a longer lifetime. Accordingly, the experiment is initialized with lithium parameters. Post loading the lithium MOT, the magnetic field gradients and currents are lowered to load a much larger sodium MOT. For a preparatory monitoring of MOT loading, a camera (Allied Visions Mako) is mounted on top of the glass cell, which collects the MOT fluorescence in a steady-live mode. For an efficient loading of the MOT atoms into the magnetic trap, it is essential that the position of the MOT is optimized for the transfer. This is mainly done by the small slower coil and the compensation coil. A small but necessary contribution in this regard also comes from another three pairs of coils called the offset coils.

Path	Sodium(MHz)	Diffraction order (sodium)	Lithium(MHz)	Diffraction order (lithium-7)
Spectroscopy^{d}	70.8	+1	120	-1
Slower	200.2	-1	271.3	-1
MOT cycling	82.3	+1	80.3	-1
MOT repumper	112.7	+1	150.2	+1
MOT repumper^{d}	–	–	290	+1
Umpump	76.0	+1	23.9	+1
Umpump repumper	80.0	+1	–	–
Imaging	105.3	+1	80.6	-1
EOM (^{23}Na slower)	1713	+1	–	–
big AOM	1699.1	+1	–	–

Table 3.1: Laser frequency manipulation using AOMs. The frequencies laser beams are sent through AOMs to up-shift or down-shift the frequencies, depending on the order of diffraction. Subscript d indicates a double path configuration.

3.1.4 Magnetic trap

Magnetic trapping in combination with the technique of forced evaporative cooling is a standard procedure employed to reduce the temperature of the atoms and increase their phase space density. Magnetic trap essentially makes use of a spatially varying potential, that is created due to the Zeeman shift experienced by the neutral atoms when subjected to an external magnetic field. Depending on the atomic hyperfine state and hence the magnetic moment, the magnetic potential energy might decrease or increase, meaning that the force the atoms experience may drive them either towards the regions of higher field or lower field. The states whose energy decreases with the intensity of the magnetic field are termed *high-field seekers* and the ones whose energy increases with field intensity are called *low-field seekers*. Since it is forbidden to create a local maximum in the magnitude of magnetic field as per Earnshaw's theorem[109], the magnetic trap is always constructed to trap the low-field seekers. In sodium, generally $|1, -1\rangle$ is favoured because of its low three body collision rate[110]. However, taking into account the possible mixture experiments, and magnetic field configurations, it is more favorable choose the stretched state $|2, 2\rangle$ in the case of the Na-Li experiment[47][98]. There

[11] 8s was a generous loading time for the dark spot MOT of sodium, however, when the oven started depleting, it had to be loaded for as long as 30s. A bright MOT on the other hand loads much faster[90].

exist different possible geometries and methods to realize magnetic traps[111]. The early setups on the Na-Li implemented a plugged quadrapole trap[89, 112], which was later changed to Ioffe-Pritchard type cloverleaf trap[113]. The cloverleaf assembly consists of four pairs of coils (see Fig. 3.7) to obtain a 3D harmonic confinement and they are situated in two coil holders on either side of the glass cell. The four coils are termed *gradient* (green), *curvature* (red), *finetune* (yellow) and *anti-bias* (blue). The gradient coils provide the radial confinement. The axial confinement is provided by the curvature coils. The curvature coil along with anti-bias coil bring the trap bottom close to zero. To avoid the Majorana losses at the zero crossing in the axial direction, a bias current is driven through the curvature coils. The current flow through the coil assembly is controlled through a set of power transistors called IGBTs. The implementation of the coil assembly, and the mechanism of control using the IGBTs are explained in detail in [90]. During the course of this thesis, the IGBT circuit was simplified without compromising the performance.

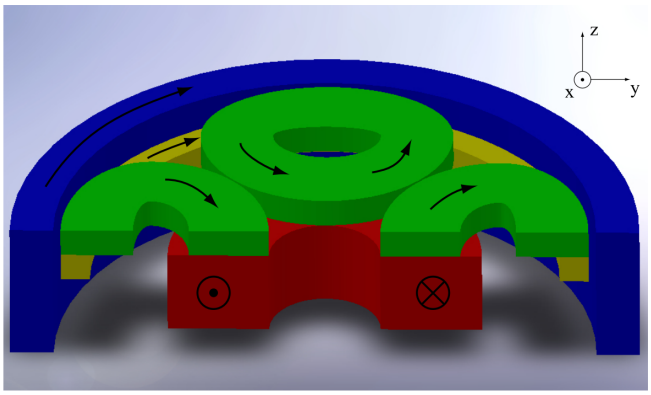

Figure 3.7: Cross section of the coil assembly. A total of eight coils (four pairs) are housed in a coil holder and are situated on either side of the glass cell. They are named gradient (green),anti-bias (blue),curvature (red) and finetune (yellow). They are used to produce magnetic field during MOT (curvature and anti-bias), spin polarization(finetune), and magnetic trap (see text). Image taken from [90].

The loading to the magnetic trap is preceded by another stage called spin polarization[114, 115]. This is a technique to enhance the transfer efficiency of the magnetic trap, by driving all the atoms in the MOT to the stretched state $|2, 2\rangle$, which were otherwise trapped in F=1 state because of the dark spot technique. It is comprised of two steps: first, a homogeneous magnetic field is applied through a set coils called finetune which results in the separation of magnetic substates. Subsequently, two laser beams named *umpump* and *umpump repumper* optically pump the atoms in the unwanted substates of $F = 1$ and $F = 2$ to the desired $|2, 2\rangle$. Lithium undergoes the same procedure, except that there's no separate umpump repumper beam for ^{7}Li, and its role is replaced the regular repumper beam.

MOT	Spin polarization	Magnetic trap	Spin purification	Evaporative cooling
	• fine-tune ramp, optical pumping to $\|2,2\rangle$	• curvature, gradient and bias ramps	• MW sweep to remove atoms in $\|2,1\rangle$	• Two MW ramps to couple $\|2,2\rangle$ and $\|1,1\rangle$
	t = 600 µs	t = 3 ms	t = 1.9 s	t = 9 s + 9s

The currents in the magnetic trap coils are ramped up subsequently. An additional step called spin purification is performed in the magnetic trap to ensure that the residual atoms in the unwanted substates are removed to prevent any further spin-exchange processes leading to heating of the sample. This is achieved by coupling any atoms remaining in $|F = 2, m_F = 1\rangle$ to the untrapped states $|F = 1, m_F = 1, 0\rangle$ via an MW sweep.

Evaporative cooling

Evaporative cooling is a method in which, the hottest atoms in the cloud are removed, allowing the remaining atoms to collide and thermalize to a colder temperature than before[96]. In the Na-Li experiment, only sodium is subjected to evaporative cooling, where an MW ramp drives the hottest atoms in $|F = 2, m_F = 2\rangle$ to $|F = 1, m_F = 1\rangle$. The latter Zeeman state is untrapped and hence the atoms are lost from the trap. The respective values of frequencies are given in table 3.2. All the processes involving such MW/RF coupling, be it a single frequency pulse or a ramp, are controlled via a home-built microwave setup. It is comprised of an Arduino DUE, two DDS (Direct Digital Synthesis) boards for generating well defined frequency signals, a couple of frequency mixers, and an adjustable PLL (Phase Locked Loop). All these components provide a flexible and a versatile unit, that can output signals anywhere between 0.3 MHz - 4.4 GHz with a power of $\approx$ 3 W. Fast switches are installed wherever necessary to ensure a better control. To facilitate the generation of all the relevant frequencies, a stable clock reference is provided for all these components by a rubidium clock. Detailed description on exact parts used, the timescales, working principle and characterization of the setup is found in [98].
Every ramp is composed of several steps as shown below:

- The Arduino accepts the following ramp parameters in ASCII fahsion: duration t, start frequency (F), stop frequency (f), amplitude (a). The times are accepted in microseconds, frequency in Hertz, amplitude in default units of DDS. For example, the first cooling ramp is written as,

  `rt900000F1900000000f18000000a1000z`.

  The Arduino identifies the letters `r` as ramp and `z` as the end of communication. It can take multiple ramp commands written end to end. These ramps are specified in the beginning of the experimental sequence (see *Experiment.py* in Appendix B), which are sent to the arduino during the compilation of the shot. The parameter values are added as globals in runmanager and subsequently in the script.

- Upon receiving the strings, the arduino automatically selects the DDS board to be used and calculates the time steps of the ramp to be given. It is programmed in such a way that, once the first TTL is received, it follows the timings closely by starting its own hardware clock and controls the rest of the DDS setup to start the ramps at appropriate instances.

- At the end of every cycle, the arduino is reset via the experimental control[12].

[12]This is a crucial step, as otherwise the Arduino fails to read the commands from the next compiled shot.

Once again, due to the constraint that ^{6}Li doesn't allow for evaporative cooling at low temperature, sympathetic cooling was implemented, so that the lithium is cooled by the thermal contact and subsequently with elastic collisions with the large sodium cloud[116][117]. To this end, two consecutive cooling ramps are carried out each lasting for 9s. It is only after this stage that any reliable information about the density and atom numbers in the magnetic trap are obtained, which can be further used to benchmark the mixture. Speaking from a diagnostic point of view, the quality of the magnetic trap is not only decided by the parameters of the trap and the cooling itself, but also by the MOT and the slower. Hence, the quantitative improvement of MOT and slower are performed such that the atom number and density in the magnetic trap are maximized. They are measured in terms of arbitrary counts of optical density, which is deduced from the absorption images taken after the final cooling (see section 3.1.6), as shown in Fig. 3.9a.

Process	Transition	Start Frequency(f) (MHz)	Stop frequency(F) (MHz)
Spin purification	$\|2,1\rangle \rightarrow \|1,0\rangle$	1870	1810
Evaporative cooling I	$\|2,2\rangle \rightarrow \|1,1\rangle$	1900	1800
Evaporative cooling II	$\|2,2\rangle \rightarrow \|1,1\rangle$	1800	1776
RAP	$\|2,2\rangle \rightarrow \|1,1\rangle$	1774	1778

Table 3.2: Frequency table for MW transitions. After the MOT stage, several MW transitions are performed to get a better transfer efficiency and less three-body losses in MT and ODT (see text). These signals are generated by a home-built microwave setup. The frequency values, amplitudes and phases are programmed into the device to be emitted upon receiving an external trigger.

3.1.5 Optical dipole trap

While many experiments have managed to reach degeneracy directly after evaporative cooling in the magnetic trap[118], some have done so by all optical means [119][120]. However, the Na-Li experiment implemented both stages. As the early focus of research in the Na-Li experiment was on polaron physics, it aimed at achieving a large condensate of sodium with $\approx 10^5$ atoms[90]. Hence, it implemented magnetic trap as an intermediate stage, where the atoms are cooled enough to be trapped in a subsequent optical dipole trap, as the trap depth created by a ODT is shallower. This is because, the electric dipole interaction in ODT, is much smaller than its magnetic counterpart. The sign of detuning decides the sign of the dipole potential created by ODT, i.e. a red detuned beam creates an attractive potential that traps the atoms in its intensity maximum, while a blue detuned beam creates repulsive potential, and traps the atoms in the regions of intensity minimum. The potential scales as I/δ, and the photon scattering rate scales as I/δ^2, where I is the intensity of the laser beam and δ is the detuning. Hence, to avoid heating atoms by the absorption of photons, the dipole trap beams are typically far-detuned. The traps can be fashioned either in a single beam trap[121][122], or a crossed dipole trap, which is created by two or more laser beams crossing at their foci, typically at an angle of 90°[123].
The Na-Li experiment initially used an infrared laser (DiNY cwQ 50, 1064 nm, 30W) to implement a crossed ODT. Its optical power was split into two dipole beams called the *waveguide* (horizontal) and the *dimple* (vertical). The trap was constructed such that the waveguide is

oriented at an angle of 8° with respect to the axis of the magnetic trap, meanwhile the dimple was shone diagonally from bottom to top, tilting the plane of the trap by 40° with respect to the horizontal plane. During the course of this thesis, DiNY was replaced due to its faulty cooling system, and was replaced by an industrial laser (IPG Photonics,1070 nm, 50W)[13]. The latter features a fiberized output, and is additionally equipped with a guide beam at 780 nm for alignment purposes. The underlying schematics is shown in Fig. 3.8. As only the laser was replaced, the rest of the optical layout was kept similar to the original setup[112][93].

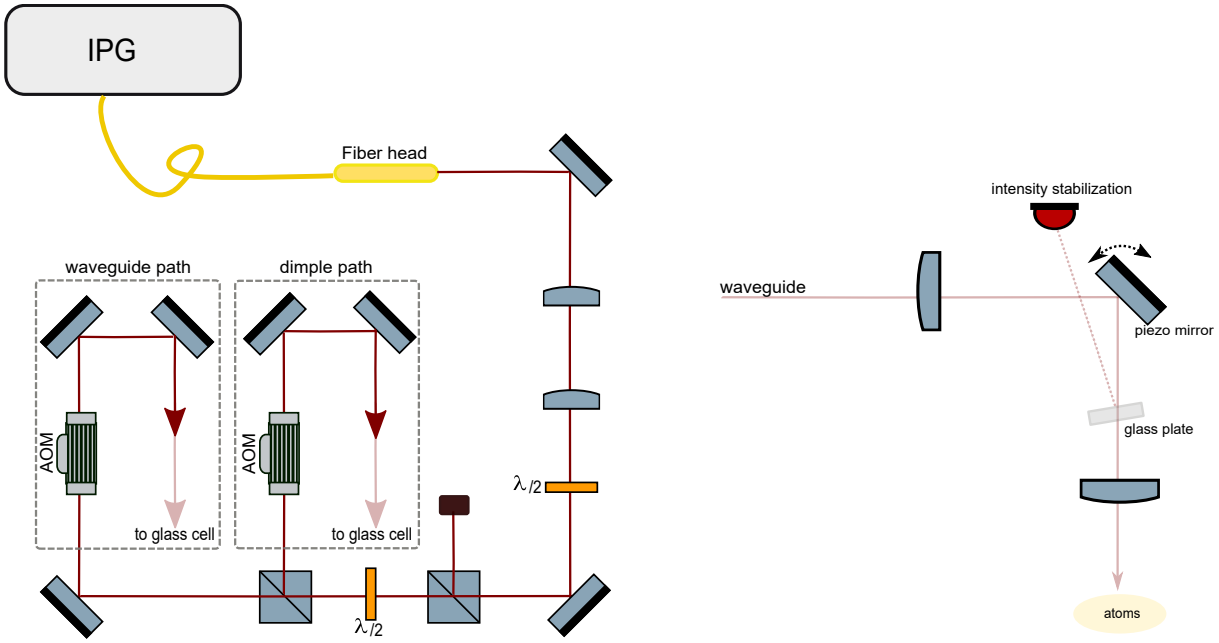

Figure 3.8: Simple schematics of the ODT setup with IPG laser. The telescope reduces the beam size to avoid clipping on the AOMs which are installed for intensity stabilization. The intensity of the beams are controlled by the half-wave plates. The transparent red arrow indicates the fact that the laser beams are guided out of the box, onto the glass cell. Before the beams enter the glass cell, they pass through the intensity stabilization setup (see text). Moreover, both the paths are equipped with piezoelectric mirrors that allow for fine-adjustments of the beams.

Alignment and intensity stabilization

The setup shown in Fig. 3.8 is situated inside a box that's kept closed at all times due to laser safety reasons. The two beams are sent through two AOMs (80 MHz, +1 order for waveguide and -1 for dimple) prior to their path towards the glass cell. Since these beam are of very high power, their paths are physically enclosed in aluminium pipes. Before entering the glass cell, they are reflected off mirrors with piezo actuators, which are controlled via the experimental control system. As shown in Fig. 3.8, a pick-off glass plate in each beam path is used to collect a small amount of light onto a quad photodiode for intensity stabilization. A standard PI controller is used to regulate the RF power (VCO amplitude) of the AOM driver. Upon installing the IPG laser, the optical setup was re-aligned to restore the intensity stabilization, followed by optimizing the loading from the magnetic trap. In a typical alignment procedure, the last two mirrors in the box (setup on the left) in the path of each beam were tweaked to get the first signal on the photodiode, and then on-wards beam walked to maximize the signal. The

[13] DiNY was intact and fully functional during the SCC experiment.

error signal was monitored, and the alignment was performed such that throughout all the amplitude levels needed for the experiment, the error signal stayed at zero. To obtain the first atomic signal after loading from the magnetic trap, each beam was displaced by manually tweaking the piezo mirrors, thus obtaining a course scan of the position. Once a weak signal was obtained, the piezo mirrors were scanned more systematically with the experimental control, to get an improved alignment.

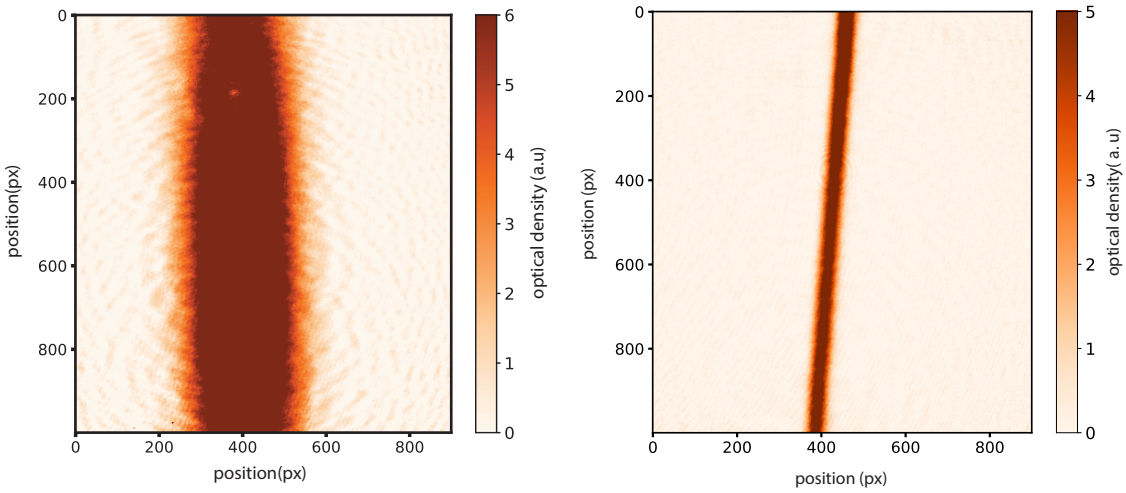

(a) sodium in magnetic trap

(b) sodium in waveguide

Figure 3.9: Absorption images of sodium atoms. These are the final images obtained after processing the three images taken during imaging stage (see 3.1.6). The optical density is evaluated as per equation (3.1). Both the images are captured by the standard top imaging path. **(a)** atomic cloud after evaporative cooling. **(b)** subsequently in the first dipole beam, the waveguide.

Loading the atoms into the dipole trap in an experimental run takes place in several steps. The waveguide beam is ramped up first as it provides a horizontal and an elongated confinement similar to magnetic trap. After the evaporative cooling in the magnetic trap, a 'hold' stage is included during which, the magnetic confinement is reduced by ramping down the coil currents, and the power of the waveguide beam is ramped up to $\approx$ 10 W. It is crucial that the waveguide is positioned slightly below the magnetic trap in its vertical plane, since the atoms fall when the confinement of the magnetic trap is reduced. At this stage, the atoms still reside in $|2,2\rangle$, and are prone to increased three-body collisions. Hence, the process of Rapid Adiabatic Passage (RAP) is employed to transfer them to the lower manifold of $|1,1\rangle$[124]. The transfer is achieved by sweeping the frequency across the resonance, while keeping a fixed magnetic field[14]. This process is carried out in two steps: first, a homogeneous magnetic field of $\approx$ 2G is applied using the offset coils along y-axis (along the Zeeman slower direction and perpendicular to the waveguide). Once the field is ramped up, the DDS setup starts the MW ramps with defined frequency ranges. As soon as the atoms are transferred to $|1,1\rangle$, the dimple beam is ramped up close to 7W, creating a crossed ODT. Once again, evaporative cooling is employed where the power of the waveguide is reduced to 1W, thus lowering the trap depth. This stage lasts for about 5 seconds during which the condensation is reached. The dipole beams are then switched off, and the cloud is imaged either in-situ or via Time of Flight (TOF).

[14]RAP requires the adiabatic change of detuning. In principle, it can also be done keeping the frequency fixed, and ramp the magnetic field up and down.

3.1.6 Imaging

In most experiments, the information about the trapped atoms or condensates is obtained by probing them optically, i.e., by making use of light-matter interaction. Depending on the optical density of the cloud, and the intensity of the imaging beam, there exist different techniques to extract information about the atoms[125]. In general, it is possible to image the atomic cloud via two methods: i) in-situ imaging, that probes atoms in their trapped state, thus revealing the spatial distribution in real space. ii) TOF imaging, that captures the state in which the atoms undergo a ballistic expansion. It is particularly useful to identify the onset of condensation. The same observation in-situ would require a much higher resolution. The imaging system of the Na-Li is optimized and calibrated for absorption imaging in TOF[126]. This method relies on the principle of Beer-Lambert law of absorption of light traveling through a medium. The standard procedure involves sending a resonant laser beam to be absorbed by the atoms, which causes a shadow in the spatial profile of the beam due to the missing photons. Knowing the initial and final intensities of the beam, the optical depth is calculated. It is typically done by acquiring three images: i) image with atoms, ii) without atoms, and iii) dark image. The third picture is subtracted from the first two to obtain the initial and final intensities of the imaging beam, thus removing any background illumination or faulty pixels,

$$I_i = I_{atoms} - I_{dark} \quad ; \quad I_f = I_{ref} - I_{dark}$$

The three images are then used to calculate the optical density as per,

$$n_c(x,y) = -\frac{1}{\sigma_0}\left[\alpha^* \ln\left(\frac{I_f(x,y)}{I_i(x,y)}\right) + \frac{I_i(x,y) - I_f(x,y)}{I_0^{sat}}\right] \tag{3.1}$$

where $\sigma_0 = 3\lambda^2/2\pi$ is the resonant scattering cross section for a two-level transition, I_0^{sat} is the saturation intensity and α^* is a dimensionless parameter arising from experimental imperfections, polarization effects, residual detuning etc. The first term in the brackets equation (3.1) dominates for low intensity imaging, when the imaging intensity $I_i \ll I_0^{sat}$ and the second term can be neglected. The latter is a saturation correction, and becomes important only in the case where the intensity of the imaging beam is much higher than I_0^{sat}. In either case, α^* should be calculated in order to calculate the correct density.
The imaging system of the dual species of Na-Li is constructed in a cage system, in the form an elongated tower situated below the glass cell. The imaging setup and its characterization is is explained in detail in [127][93]. The imaging beams for both the species are resonant to the cycling transition (see Fig. 3.2 and Fig. 3.3). Two cameras (Sodium: Q-Imaging Retiga EXi, Lithium: Nüvü HNü 512 EMCCD) are mounted outside the tower on 3-axis translation stages. During an experimental run, they are put in trigger mode, such that they capture an image whenever they receive a TTL signal. The respective imaging beams are switched on for 25μs and the atomic signal is detected by the cameras. In addition, repumper beams are shone as the condensates are created in $|1,1\rangle$. In the case of sodium, the repumper beam is shone 25 μs beforehand because of an optically thick cloud. The atoms are lost after the first image due to the destructive nature of the imaging procedure. The reference image is then taken 200 ms afterwards, followed by a dark image 400 ms afterwards.

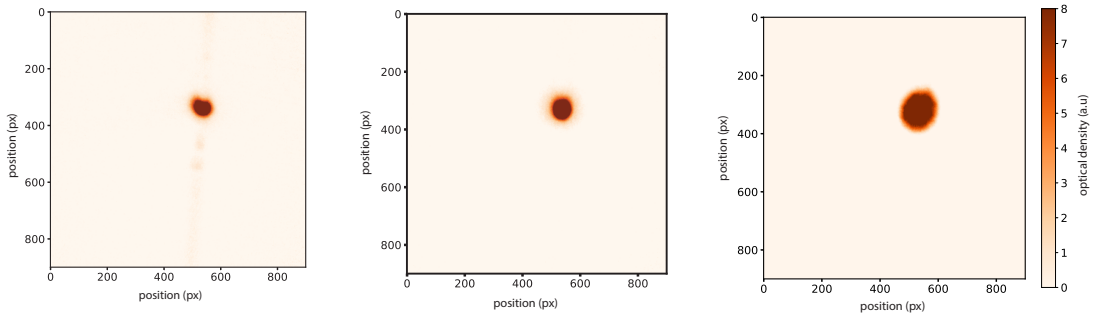

Figure 3.10: Absorption images of sodium BEC in crossed dipole trap. The imaging beam is accompanied by the repumper beam as the BEC is created in $|1,1\rangle$. **(a)** in-situ **(b)** TOF = 5 ms **(c)** TOF = 10 ms.

The values of I_0^{sat} and α^* should be determined prior to the estimation of n_c as given in (3.1). The absolute atom number is then calculated by integrating the column density in the xy direction. An imaging calibration was performed for both species as explained in detail in[1]. The method presented therein is based on three major steps:

- calibration of imaging magnification.
- calibration of I_0^{sat}: Different images were captured by scanning the optical power of the imaging beam and the resulting intensities are calculated in units of camera counts per pixels per μs.
- calibration of α^*: For a series of numerical value of α^*, imaging intensity was scanned, and the atom number N_{at} was evaluated. For every such measurement, the standard deviation of N_{at} was calculated. As the value of N_{at} is a genuine property of the atomic cloud itself, and has nothing to with imaging, only that value of α^* was deemed to be correct which corresponds to the measurement with minimum fluctuations.

The values resulted from the above evaluation is listed in table 3.3.

Path/Species	Magnification, M	I_0^{sat}(counts/(px$\times\mu$s))	α^*
Sodium	6.58$\pm$0.04	20.3	3.6
Lithium	15.44 $\pm$ 0.12	11.2	3.1

Table 3.3: Results of imaging calibration. These values are necessary to be able to use equation (3.1) to calculate the atom numbers.

The intermediate stages such as the magnetic trap or the ODT prior to generation of the BEC serve as the best diagnostic tools. The absorption imaging scheme, even though not calibrated for those stages, still provides realistic estimations which can be benchmarked. Hence, typically it all comes down to improving the number of trapped atoms, and increasing the phase density, until condensation is reached.

3.1.7 Experimental control

For many years, including the times when the SCC experiment was performed, a MATLAB based software was responsible for controlling the experiment. It contained a custom written editor named SDFF, where all the instructions needed to initialize and control the required devices were stored[106]. Upon initialization of an experimental shot, these instructions were sent to the National Instruments (NI) cards which are responsible for the actual control on the hardware level. In toal, there are three NI 6733 cards and one NI 6254 card, and all are housed in a PXI- 1033 chassis[106, 128]. The cards consists of multiple analog and digital channels. The analog channels provide a continuous voltage range of 0-10V. They are typically used to provide the VCO amplitudes in AOM drivers, control voltage for the trap coils etc. The digital ones are fixed in the form of 0 or 5V TTL, and are used as trigger signals to control shutters, switches etc. While the previous MATLAB control provided all the necessary features of a control system, it was based on a constant-rate clock. Hence, whenever a command was issued, say with a time step of 5 µs, the compilation of the sequence was chopped in steps of 5 µs, leading to a sluggish performance. With a typical mixture BEC cycle in the Na-Li experiment taking more than 45 seconds, this called for an alternative solution.
The new control *labscript suite* is based on Python. It was originally developed, specifically keeping ultracold experiments in mind[129, 130]. It is a control framework designed for automatic hardware control, optimization and analysis[131]. The instructions are handled by a variable frequency clock, i.e., it changes the clock output only when a clocked device needs to update an output. Hence, the need for redundant instructions is removed. It combines the high-level instructions with the help of scripts and GUIs and compiles them to low-level instructions appropriate for the hardware. Along with the user defined functions, logical instruction and parameters it aids in forming an experimental sequence. The overall functionality of the labscript suite springs from its different parts as described:

- It is composed of six programs, namely, labscript, runmanager, runviewer, BLACS, lyse and BIAS.[15] These programs can be further divided into two groups: i) those which are used for the preparation stage, ii) those which carry out the hardware binding and execution in real time. Fig. 3.11 shows how they all function together as one unit to execute an experimental shot. Each of these tools are discussed briefly in the following text.

- The heart of execution of the experiment lies in two python scripts, namely, *connectiontable.py* and *Experiment.py*. The former establishes the device integration to the control system by physically defining the hardware connections. The latter contains the experimental sequence itself, where the commands are written to carry out a specific task.

Other devices that were added to the labscript suite include,

- The NI cards, DDS setup and Mako camera.[16]

- An FPGA based psedoclock(Opal Kelly XEM3001), which acts like a master clock.

[15] BIAS is not discussed in the scope of this thesis, since it is not used in the actual experimental control.
[16] labscript provides pre-written support for the NI cards. The DDS setup and Mako were manually integrated.

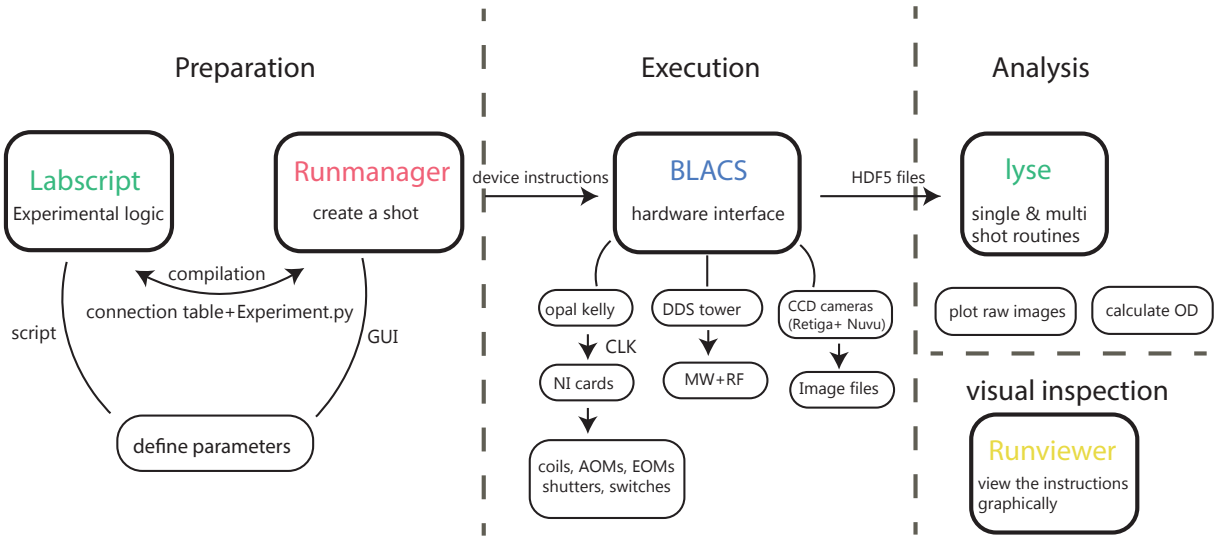

Figure 3.11: Flow of an experimental shot through the environment of labcript suite. Five of the six available tools are used in the Na-Li experiment. Labscript complies the user-written software instructions in python into device readable instructions. Runmanager is a GUI, where the user can define the global parameters. BLACS receives the instructions from labscript and communicates directly with the devices which have been integrated into it. It is responsible for initializing the experiment, and upon completion, for saving all the parameter values associated with the shot in a HDF5 file. The executed shot is automatically sent to lyse, which again executes a user written analysis script. Runviewer, if enabled, graphically represents every instruction across time.

Labscript

Labscript is text-based, and functions fully on the software side, where it provides an interface for the actual action a device should perform. It consists of two separate parts, the connection table and sequence code. The connection table consists of a complete description of all the devices such as their name, connecting port. In the example snippet shown in Fig. 3.12, it shows how the NI 6733 card is connected and clocked. Furthermore, since it is possible to define analog and digital channels on this card, the connection table shows how those channels are physically assigned to certain pins.

```
from labscript import *
from labscript_devices.NI_DAQmx.models import NI_PXI_6733

NI_PXI_6733(name='Frodo_card_6', parent_device=clock.clockline, clock_terminal='PFI7', MAX_name='PXI1Slot6')

AnalogOut(name='A1_1_Na_img_int', parent_device=Frodo_card_6, connection='ao0')
DigitalOut(name='D1_2_Na_MOT_AOM',parent_device=Frodo_card_6, connection='port0/line1')
```

Figure 3.12: Example snippet of a connection table. The connection table contains a set of information about all the devices present in the experiment. Labscript uses the connection table to generate the instructions to be given to the devices.

The primary task of labscript is to take such a connection table and create python objects for the specified hardware. Furthermore, it provides the associated functions to define the state of output channels as per experimental logic. For example, the `DigitalOut` function

allows for two methods namely `go_high(t)` and `go_low(t)` to toggle a certain channel at a given time t. `AnalogOut` on the other hand has the method `constant(value,t)` to set the channel to a fixed value.

Runmanager

Runmanager is a graphical user interface (GUI) for managing the input parameters of the experiment and to generate the shot files. To make the different stages of the experiment easily accessible, one can define different groups of parameters, each responsible for a certain stage of the experimental cycle.

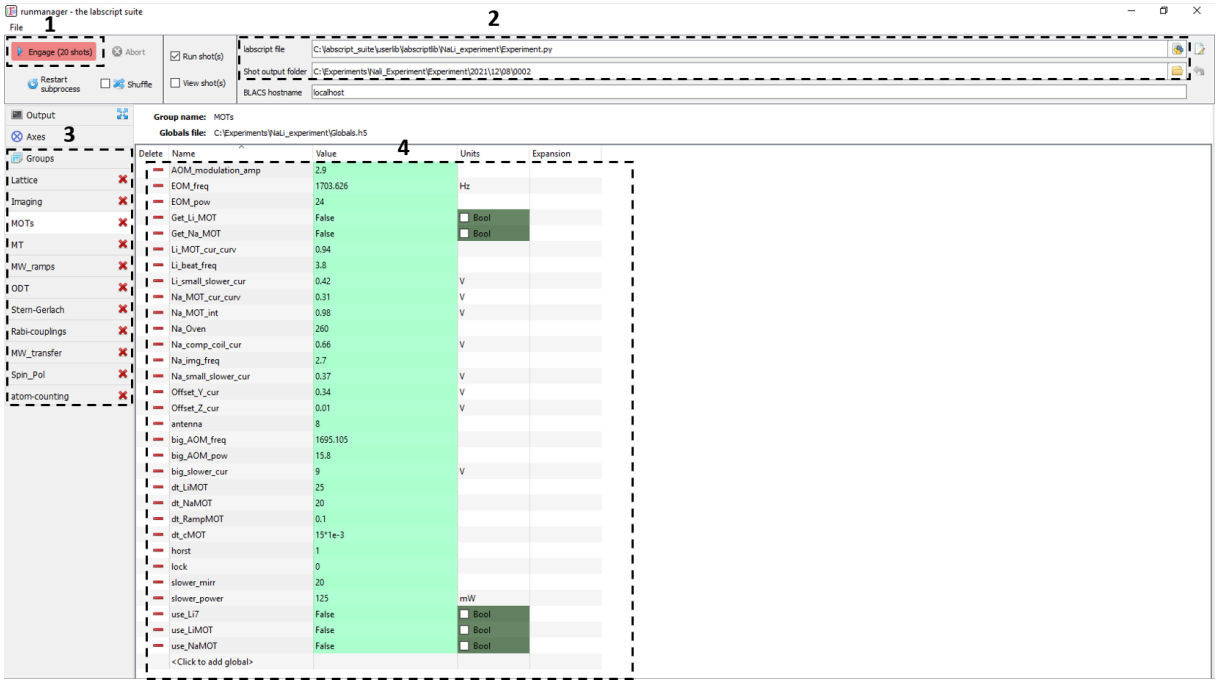

Figure 3.13: Runmanager GUI. labscript and runmanager compile the shots when Engage is clicked **(1)**. The user defined instructions for the experimental cycle are fed via *Experiment.py*. A new folder is created everyday, starting from the first shot **(2)**. The variables are defined in separate groups corresponding to each stage of the experimental cycle **(3)**. Each group contains global variables which may or may not be connected to the hardware **(4)**.

As shown in Fig. 3.13, each group contains as many parameters as required to complete that stage. Upon *Engage*, Runmanager, together with labscript produces a shot in the form of an HDF5 file. This file contains all the user defined parameters which are saved as *globals*. For example, in Fig. 3.13, the global `big_slower_cur` stores the value of the control voltage given to the power supply connected to the big slower coil. Physically, this is the analog channel at port 0 of the NI 6733 card, which is connected to the external control pin of the power supply. The values of globals can be changed as desired from shot to shot, and they can also be looped over a certain range using standard python commands such as `arange(start,stop,steps)`. In that case, a separate file for each value of the parameter is created. If two or more parameters are specified for looping, it automatically generates the Cartesian product of all the parameter arrays. Moreover, any dummy global variable can be added in the runmanager GUI. For example, the global `slower_power` is simply a variable that has no direct hardware

connection, but is only created to store the value of the optical power of the sodium slower beam on a given day. Adding such variables lets one keep track of the changes occurring on the experimental setup. Runmanager also allows Boolean variables, which are useful when creating conditional statements. For example, instructions written to create a sodium MOT are carried only when the global `use_NaMOT` is set to TRUE.

BLACS (Better Lab Apparatus Control System)

BLACS is a hardware interface, whereby it communicates with all the devices integrated into it. It launches separate Python processes to initialize each device. A detailed account on how to integrate a device can be found in[129]. While it comes with pre-written support for some devices such as NI cards, the DDS setup for MW/RF generation (more in section 3.1.4) and the Mako camera for monitoring the MOT had to be manually integrated. The cameras used for the absorption imaging (see section 3.1.6) did not need to be integrated, because they are installed in such a way that they only need an external trigger to capture an image.

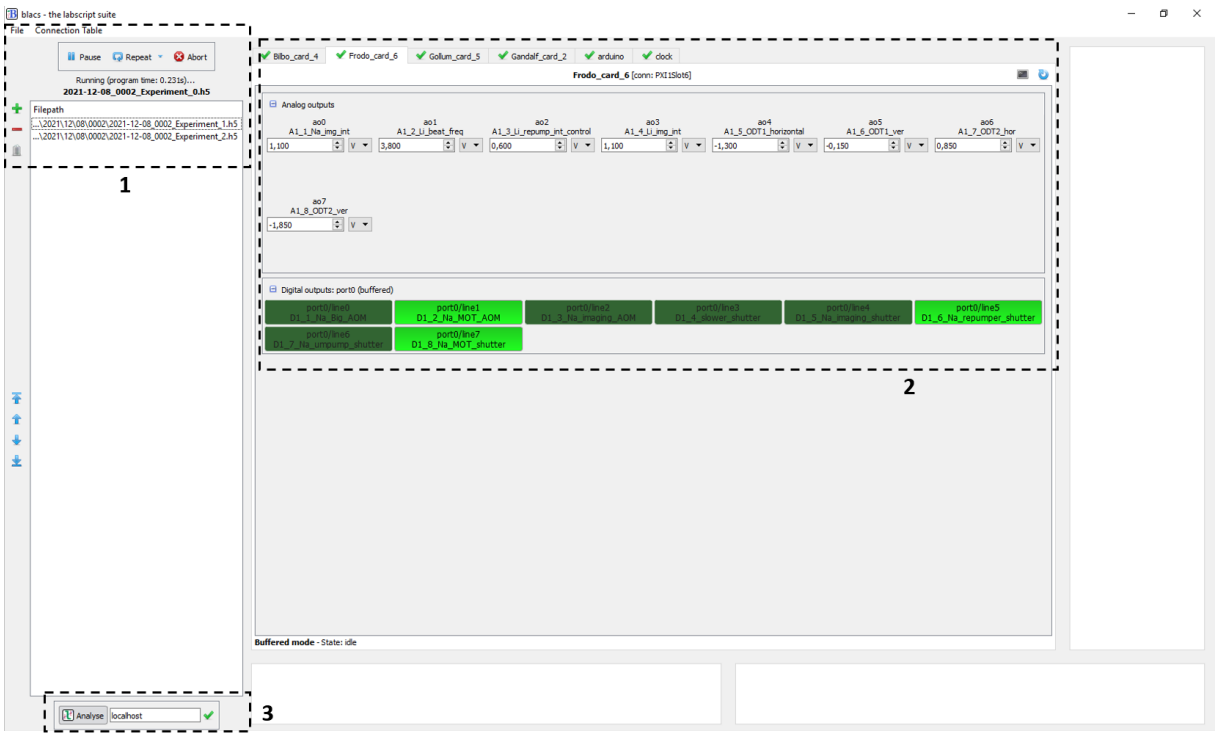

Figure 3.14: BLACS GUI. It is responsible for hardware communication and shot execution. Shots compiled in the form of HDF5 files are queued on the left **(1)**. It has the provisions to pause, abort, repeat the last compiled shot. When the connection table is uploaded, all integrated devices appear as device tabs, along with the associated globals **(2)**. Each device can be initialized individually, by refreshing the tab on the upper right corner. Next to the refresh button, it also features a terminal, where errors or outputs of the devices are printed. The shots can be sent to lyse directly after execution**(3)**.

Every device has a widget in the form of a tab in the BLACS GUI where the associated globals are displayed. Their values are taken directly from runmanager. But they can also be manually changed in the static mode, i.e., when the shots are not running. This feature is extremely helpful in debugging individual devices. The device tab can also be refreshed to physically reset the device. In a continuous operation mode, BLACS queues up the compiled

shots, and executes them consecutively. Once each shot is completed, it is saved to the HDF5. The GUI has options to pause or abort the entire queue, or to repeat them. The shots can also be deleted, and they can be added back again only after re-compiling in the runmanager.

Lyse

Lyse is a tool that performs an automated analysis immediately after the shot has been finished. BLACS passes the HDF5 file to lyse upon completion, where the analysis routines await. They are user written, standard Python scripts. Every shot added to lyse maintains a tabular structure, where all the globals are shown. Lyse offers two types of analysis routines namely *single-shot* and *multi-shot* routines. Single shot routine takes every shot as input, reads the raw data from the HDF5 file and produces plots and images if required. The same for a series of shots is handled by a multi-shot routine.

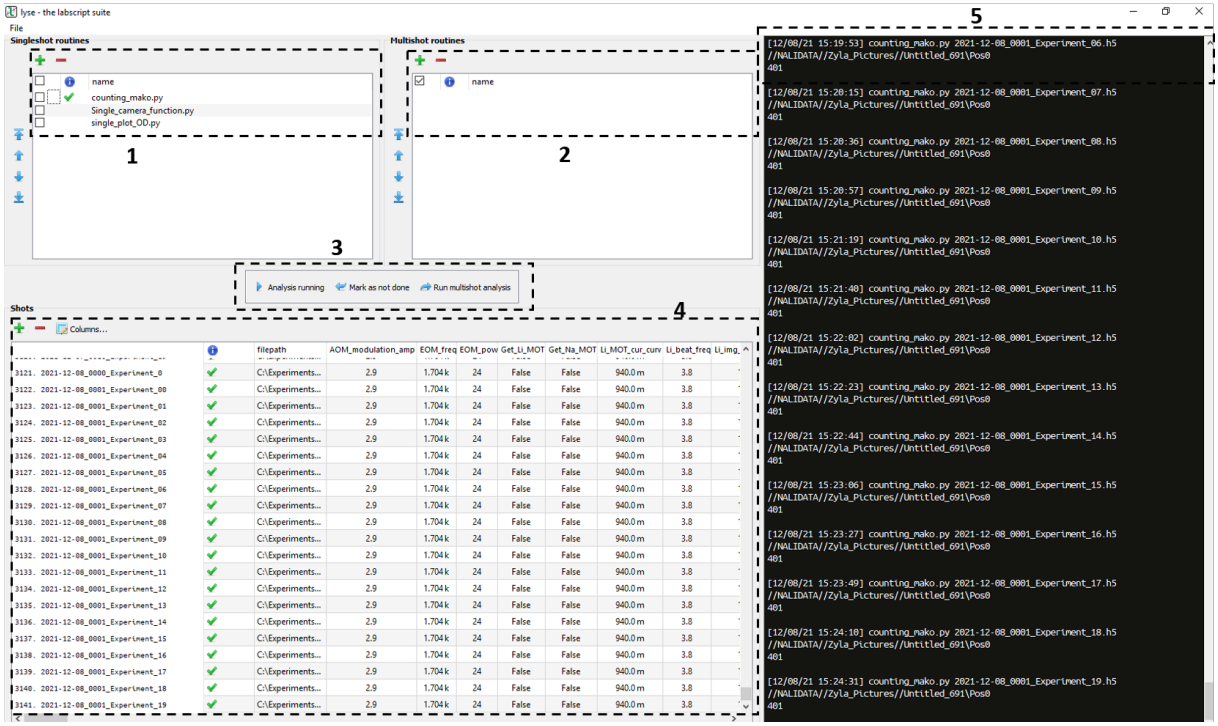

Figure 3.15: Lyse GUI. Lyse is an analysis program of the labscript suite. Analysis routines can be python scripts either for a single shots or for a series of shots**(1,2)**. In both cases, when more than one script is added, they run consecutively. The HDF5 files are displayed in a tabular form so that the parameters are visible**(4)**. A single shot can be selectively analysed by clicking *mark as not done*(**3**). Any text output of the analysis is displayed in the terminal on the right**(5)**.

There are two important single shot routines used in the Na-Li experiment. The two single shot routines run consecutively, achieving the following purposes:

- First routine to add the raw images into HDF5 file: at the end of each experimental cycle, each camera captures three raw images which are saved on a separate PC dedicated for the camera. The lyse routine grabs these images and saves them in a separate group of globals called *images*. Furthermore, it plots the three images for visual inspection.

- Second routine to calculate the atom number: this routine accesses the raw image data saved from the first routine and evaluates the optical density and the atom number according to the absorption imaging formula (more in section 3.1.6). Alongside, the calculated optical density is plotted as a final absorption image. Furthermore, it saves the images in the same directory where the HDF5 files are stored.

Since lyse can also be installed as a standalone program, large scans are typically analysed on a separate instance of lyse on a separate PC. As the values are stored in data frames, the scanned parameter can be specifically accessed by its name.

Runviewer

Runviewer is designed for graphically viewing the experimental logic. When an HDF5 file is loaded, it automatically plots the behavior of each channel across the time axis, thus displaying the signals to be given to the hardware during the execution of the shot, see Fig. 3.16. It is important to note that it only shows what the hardware would do during execution and not to be mistaken as a confirmation of actual execution, i.e., it does not differentiate between a mere compiled shot and a fully executed shot. Nevertheless, it proves to be a critical debugging tool as it is a low-level representation of the experimental cycle.

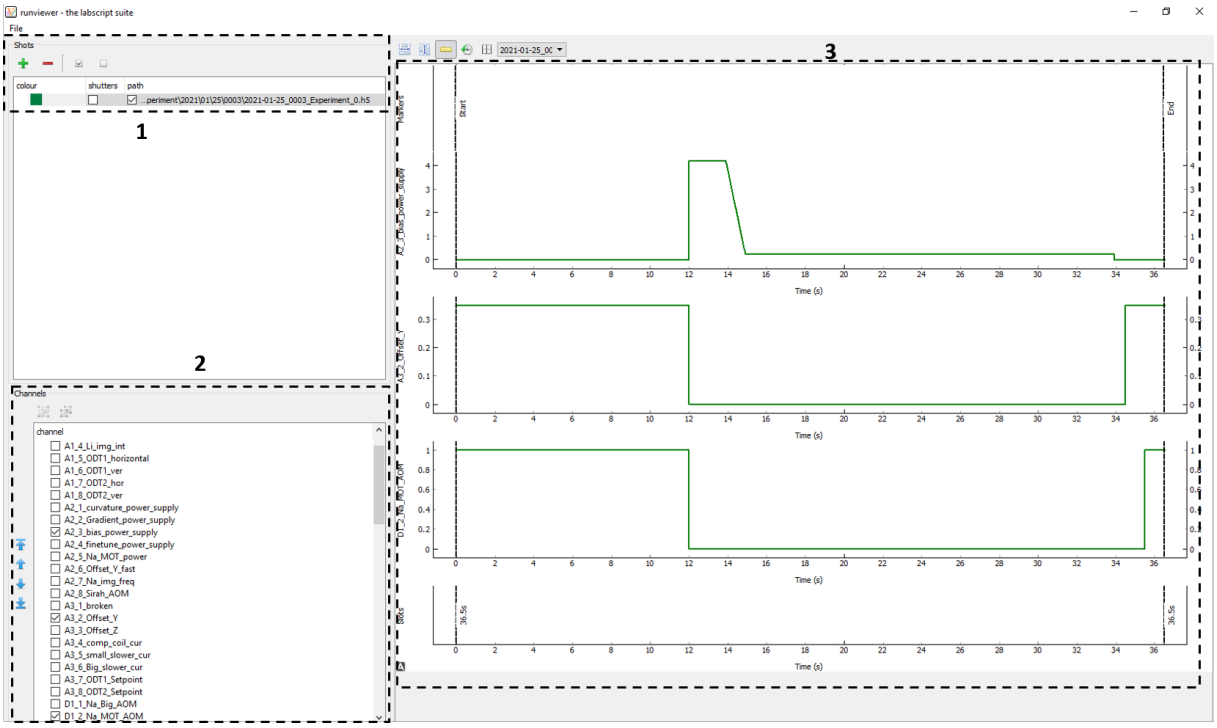

Figure 3.16: Runviewer GUI. A graphical representation of a single executed shot. The shots are either automatically added right after being compiled by the runmanager or manually **(1)**. All the variables with hardware connections show up on the bottom left corner **(2)**. They can be selectively viewed with their values plotted against time **(3)**. The plots can be zoomed to the resolution of the NI cards themselves, i.e. up to 1 s scale, thus making it feasible to troubleshoot as precisely as possible.

For example, the experiment of creating a sodium BEC begins with the MOT loading which takes place during the first 12 seconds of the cycle. Accordingly, the channel `D1_2_Na_MOT_AOM` stays high only until the loading is finished. Similarly, the control voltage for offset-y coil

needed for the MOT is set to 0.37 with the analog channel `A3_2_Offset_Y` and is switched off as soon as the MOT is loaded.

3.1.8 Characterization of BECs

As discussed in section 2.2, a BEC is characterized by condensate fraction, temperature and trapping frequencies. For the $^{23}\mathrm{Na} - {}^{7}\mathrm{Li}$ mixture, this was carried out in the previous thesis [1]. The first step in this regard was the imaging calibration (see 3.1.6) from which the atom numbers in each cloud after the final evaporation in crossed ODT were evaluated, resulting in $\approx 300\times\ 10^3$ (sodium) and $\approx 35\times\ 10^3$ (lithium). These values fluctuate from shot to shot, which is an important aspect that shall be discussed in section 4.2.3. Furthermore, the two co-existing modes in the density distributions, i.e., the condensed and the non condensed atoms were examined. By fitting the thermal part with a Gaussian profile, and the macroscopic occupation with a Thomas-Fermi profile, the atom numbers occupying the two modes were calculated, thus leading to the determination of condensate fraction. The temperature of the condensates then followed directly from equation (2.6), resulting in $\approx$ 641 nK for sodium and $\approx$ 626 nK for lithium. As the atom number and the condensate fraction fluctuate due to several experimental uncertainties, they are subjected to slight deviation on the order of $\pm$20 nK. Nevertheless, these numbers fall on the right order of magnitude. The trapping frequencies of sodium were measured in the ODT in a separate experimental sequence. The resulting values were $\omega_x^{Na}/2\pi = 243.7 \pm 1.5$ Hz, $\omega_y^{Na}/2\pi = 179.6 \pm 0.4$ Hz, $\omega_z^{Na}/2\pi = 410.4 \pm 6.5$ Hz. The same for lithium is given by $(\omega_x^{Li}, \omega_y^{Li}, \omega_z^{Li})$ = 2.08 $(\omega_x^{Na}, \omega_y^{Na}, \omega_z^{Na})$[92].

3.2 Spin-Changing Collisions between $^{23}\mathrm{Na}$ and $^{7}\mathrm{Li}$

The process of achieving condensation is the first step in accessing the spin physics and all that it has to offer. Both species are initially condensed in the same dipole trap in their respective $|1,1\rangle$ state. As discussed in chapter 2, the internal states of the two species, $|1,1\rangle$ and $|1,0\rangle$ are proposed to simulate the minimal model of U(1) LGT, via interspecies SCC. In this section, all the necessary steps employed to manipulate the spin states, as well as their reliable detection are briefly explained. Furthermore, the sequence of the SCC measurements is outlined, followed by data acquisition.

3.2.1 Initial state preparation

With sodium taking the role of the gauge field, it is necessary to implement an appropriate initial state, by creating a superposition in the lower hyperfine states of sodium $|1,1\rangle$ and $|1,0\rangle$ (see section 2.5). Given that these are magnetically sensitive, a detailed first analysis based on the Breit-Rabi description was performed[132][93]. This analysis predicted that the $^{23}\mathrm{Na}$ - $^{7}\mathrm{Li}$ mixture undergoes resonant oscillations at a critical homogeneous field of B_0 =1.953 G. This is energetically allowed, only when the energy difference of the two internal states of the two species vanishes, leading to what is termed as the spin changing collision resonance,

$$\Delta E_{Na} - \Delta E_{Li} \approx 0 \tag{3.2}$$

where $\Delta E_{Na} = E_{N,1}(B_0) - E_{N,0}(B_0)$ and $\Delta E_{Li} = E_{L,1}(B_0) - E_{L,0}(B_0)$. This condition establishes that, for a successful realization of SCC, one has to be able to create a reliable

initial state. Important technical aspects involved in dealing with these spin states are briefly described in the upcoming text.

Magnetic field stabilization

The magnetic field of 1.953 G is applied during the RAP stage using offset coils, resulting in a Zeeman splitting of 1.37 MHz between the internal states of each species. The energy with respect to the magnetic field for ^{23}Na-^{7}Li scales as 650 MHz/G according to the analysis in [93], indicating that a stable operation of the SCC experiment requires the field to be stabilized on the order of a mG. Hence, an active field stabilization scheme is employed. The basic setup is displayed in Fig. 3.17.

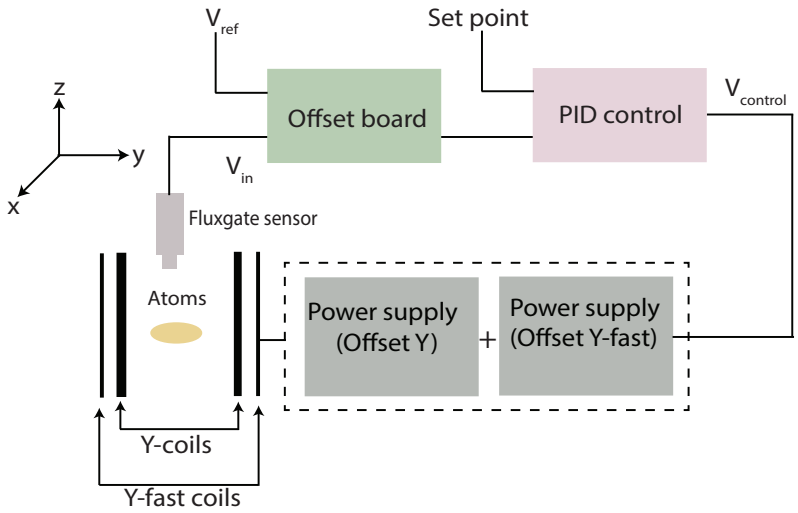

Figure 3.17: The setup for magnetic field control. This setup is employed to actively control the offset field of 1.95G that's required for conducting the SCC experiment. While the field created by Y coils is large and fixed, Y-fast create a small additional field which is stabilized. A Fluxgate sensor produces a voltage V_{in} proportional to the field value. This signal is further processed(subtraction from reference signal V_{ref} and amplification) and fed to a standard PID control board, which is connected to the analog control knob of the power supply of the Y-fast coil.

The offset magnetic field is created by two pairs of coils, namely Y and Y-fast. The latter gets its name as it contains only one winding. Both the coils are controlled by independent power supplies in CC (current control) mode. The power supplies themselves are controlled by an analog voltage given by BLACS. The underlying principle of active field stabilization is the following: The Y coils are capable of creating a larger field value (0.9G/V) and hence, they are used to create an initial offset field with a magnitude very close to that of the critical field. An additional field is then created in the same direction using the Y-fast coils, however with much lower magnitude(40 mG/V). This is the field that's actively stabilized during the SCC experiment. A fluxgate magnetometer is situated at the bulls eye of the front coil holder, which produces a voltage signal proportional to the total field value. This is fed to an offset board that is equipped with a reference voltage and an amplifier. Its function is to pre-process the fluxgate signal by subtracting the reference and amplifying it. Given that the fluctuation of the field is much smaller than its absolute value, this method efficiently tackles only the fluctuations. The final signal is then fed to the PID controller, which in turn controls the power supply of the Y-fast coil. The original setup that was in operation during the SCC experiment is

described in[133]. The offset board and the PID controller were replaced afterwards, following an incident that resulted in a faulty performance of both.

Spin-sensitive detection

While conventional absorption imaging is one of the best approaches to probe the macroscopic condensate, it alone cannot probe a multi-component BEC. Most experiments dealing with spinor condensates utilize various techniques to investigate the individual occupation of the spin states, as well as to understand coherences between those states. Some methods are so versatile that they can resolve all the spin states[134]. Such techniques often make use of spin-dependent forces either optically or through magnetic interactions[135]. In the Na-Li experiment, the latter is used, via a technique called Stern-Gerlach (SG) imaging. Originating from the analogy of the historic experiment on silver atoms by Stern and Gerlach[136], it makes use of the spin state-dependent force the atoms experience due to the magnetic moment, when placed in a region of magnetic field gradient,

$$\vec{F} = \nabla(\vec{\mu}.\vec{B}) \tag{3.3}$$

where $\mu = m_F g_F \mu_B$ is the magnetic moment of the atom in the internal state m_F, g_F is the gyromagnetic factor, and μ_B is Bohr Magneton. Thus, the above equation indicates that the atoms in different spin states are pushed in different directions. During the BEC cycle, a magnetic field gradient is applied using the MOT coils for 1.75 ms, right before the atoms expand in TOF which successfully separates the two spin states. Detailed analysis on the directions of splitting are found in[93].

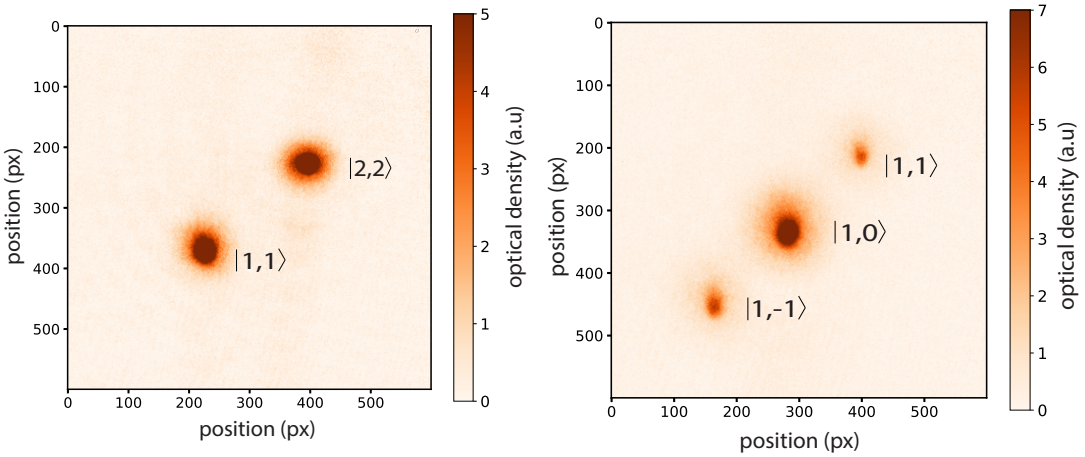

(a) $|1,1\rangle \rightarrow |2,2\rangle$ **(b)** $|1,1\rangle \rightarrow |1,-1\rangle, |1,1\rangle \rightarrow |1,0\rangle$

Figure 3.18: Demonstration of Stern-Gerlach technique. A magnetic field gradient is applied using the curvature coils, which results in a state dependent force on the atoms. The spin states with opposing magnetic moments fly in opposite directions. The extent of separation depends on the duration and the strength of SG pulse.

Two-pulse sequence

It is possible to couple sodium internal states $|1,1\rangle$ and $|1,0\rangle$ directly with an RF pulse. However, it is not the best method, given that Zeeman energy splitting is the same for both

species at the critical field. To avoid the simultaneous coupling of both the species, a procedure called two-pulse sequence is adapted, see Fig. 3.19.

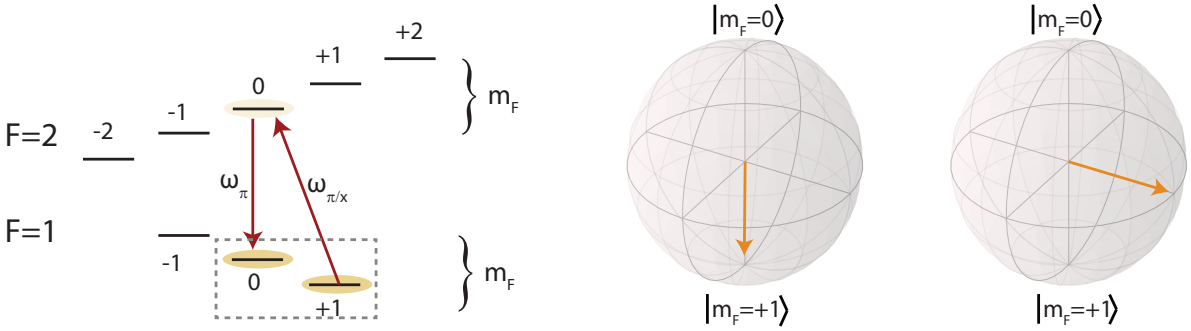

(a) Two pulse sequence in sodium with respective visualization of the spin vector on the Bloch sphere.

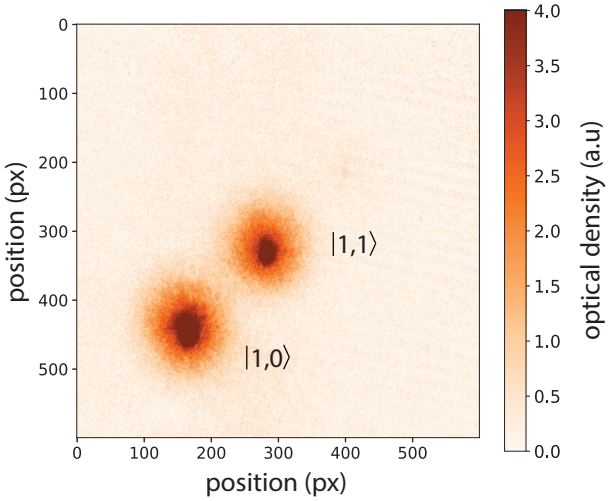

(b) TOF absorption image of sodium superposition created using two-pulse sequence.

Figure 3.19: Scheme of two-pulse sequence. Sodium BEC is created in $|1,1\rangle$. As a two-level system, it is equivalent to the spin vector oriented along the south pole of the Bloch sphere. It is superposed with $|1,0\rangle$ in two consecutive steps: the first pulse, which drives $|1,1\rangle \rightarrow |2,0\rangle$ is given by the DDS setup and its duration is variable. The second pulse has a fixed duration, and transfers all the atoms down to $|1,1\rangle$. For 50-50 superposition ratio, the spin vector lies on the equator as shown on the Bloch sphere on the far right.

It makes use of an intermediate state $|2,0\rangle$ to achieve the final superposition. It consists of sending in two consecutive pulses, where the first pulse is of variable duration, and the second pulse is a fixed π-pulse. Since lithium is off resonant to these two transitions, it stays unaffected during this stage. The DDS setup that handles the rest of the RF/MW processes is used only partly to implement the above process. This comes from the limitation of the DDS board itself, it possesses a dead time of ≈ 0.5 ms between two consecutive pulses. Atoms cannot be held in $|2,0\rangle$, as it leads to losses within milliseconds as compared to other states at the same density. Hence, the DDS setup is used to give only the first pulse, and the second pulse is given by another microwave source (HP-8657B). The different possible superpositions are accessed simply by changing the length of the first pulse as shown in Fig. 3.20.

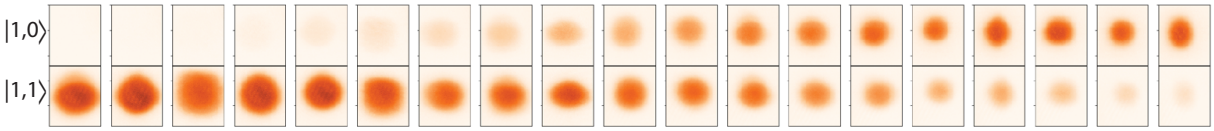

Figure 3.20: Absorption images of sodium in a typical superposition scan. Starting from $|1,1\rangle$, the duration of the first pulse is varied, leading to a change in the superposition ratio. The duration of the first pulse ranges from 0-200 μs, with the 200 μs corresponding to a complete reversal of population.

3.2.2 Interspecies SCC

Several measurements were performed to study the interspecies SCC interaction. As shown in Fig. 3.21, every such measurement incorporated a series of standard steps, following the formation of condensates.

- Applying a homogeneous external magnetic field, corresponding to the critical field $\approx$ 2G. This is done during the RAP stage and the field is actively stabilized. It is at this field, the lower hyperfine Zeeman levels of both species become degenerate, thus energetically allowing the spin exchange. It is experimentally tunable and is stabilized throughout the sequence.

- Preparing the initial state, as explained in section 3.2.1. Two consecutive MW pulses bring sodium in $|1,1\rangle$ into superposition with $|1,0\rangle$, while lithium stays in $|1,1\rangle$, unaffected. This is performed after the last evaporation ramp of the waveguide, i.e immediately after the BEC is formed. It lasts for a total of $\approx$ 300 μs, which is rather short compared to the timescale of the dynamics and hence, can be termed as a superposition quench. As the first pulse is of variable duration, the initial sodium imbalance is experimentally tunable. In the upcoming sections, it shall be denoted by $\eta_0 = N_{0,N}/N_N$.

- Evolution of the four atomic states following the sodium quench. This is provided by simply adding a waiting time in the experimental sequence. The interaction time is also tunable, since it is managed directly by the experimental control.

- The states are spatially separated using a SG gradient and are imaged in TOF .

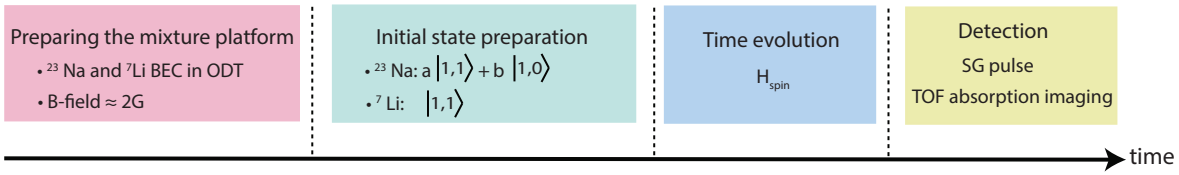

Figure 3.21: A standard experimental cycle designed to study the interspecies SCC. Once the initial preparations are satisfied, the coupled spin Hamiltonian evolves leading to spin dynamics.

The first signal of SCC in lithium due to its interaction with sodium was observed at 2.118G. A simple visual inspection of the TOF image of lithium confirmed that the lithium atoms underwent a clearly visible transfer from a fully polarized state of $|1,1\rangle$ to $|1,0\rangle$, which wasn't populated earlier. This spin exchange process was not observed in the absence of sodium, which reinforced the fact that it is indeed a mediated interaction. The SCC experiment was

performed in several parameter regimes, by making use of all the parameters that were experimentally well controlled. In all the experiments conducted, only a small portion of atoms, on the order of 6-8% were found to be transferred to $|1,0\rangle$ (see section 3.2.3 and 3.2.4). Additionally, an unwanted noise signal was always present on the images, in the form of interference fringes that resulted from the imaging beam itself. Moreover, the mechanical vibrations during the experiment caused such fringes to become nonuniform in time. To circumvent this problem of low signal-to-noise ratio, and to remove the possible imaging artefacts, an image processing method called *defringing* was applied to lithium images[137][138]. The central idea of defringing is the following: instead of using the reference image that was taken as a part of the imaging procedure in every shot, it involves manually constructing a reference image, whose fringe patterns match that of the image with atoms. This method reduced the standard deviation of the absolute counts in the no-atom region by $\approx 50\%$. To this end, only lithium images were defringed[17]. The methodology and application of defringing to the SCC data is explained in [1]. The rest of the analysis, such as calculating the atom numbers was performed in the standard way (see section 3.1.6).

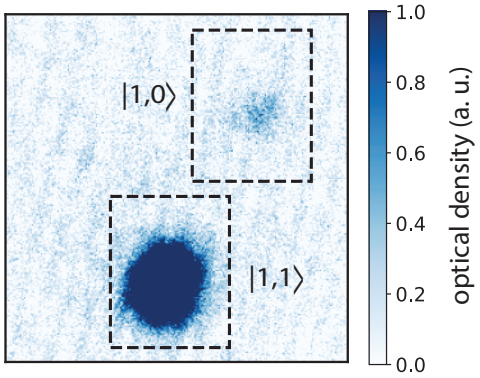

Figure 3.22: Onset of spin changing collision in lithium. Following the superposition quench in sodium that results in a certain imbalance η_0, the mixture was allowed to evolve for a certain duration. An SG magnetic gradient prior to imaging separated the two spin states. Lithium showed clear signs of spin transfer, where some atoms were transferred from $|1,1\rangle$ to $|1,0\rangle$.

3.2.3 Time evolution measurements

In this type of measurement, every shot was taken with a fixed imbalance in sodium, while the evolution time was varied from shot to shot. One complete SCC sequence consists of hundreds of shots with their evolution time ranging from 0-100 ms. Such sequences were repeated multiple times for statistical accuracy. In addition, the shots were executed in a shuffled manner to avoid any systematic drifts in the observed signal. There exist two time evolution measurements in total, with differing initial state as shown in table 3.4. The offset field for both was kept at 2.118 G and the evolution time was scanned up to 100 ms. Raw absorption images were analysed to obtain the optical densities. The occupation number of each spin state was determined by carefully selecting the regions of interest where the atomic signals were found. The final absorption images for the first 10 shots in the data set I are

[17]The observable in question in an SCC experiment is always the lithium ratio. Absorption images of sodium are four times larger in size than that of lithium, and the defringing becomes computationally heavy. Besides, due to its large atom number, signal-to-noise ratio is not as big of an issue.

displayed in Fig. 3.23 and Fig. 3.26. As these figures are intended only as an example of the onset of SCC, the rest of the shots in the data set are not shown here for the sake of clarity.

Date	Data set	Imbalance in sodium (η_0)
18.04 + 23.04.2019	I	0.407
24.04.2019	II	0.293

Table 3.4: Time evolution data set. In these types of measurements, the evolution time is scanned. Each data set corresponds to a fixed sodium imbalance η_0.

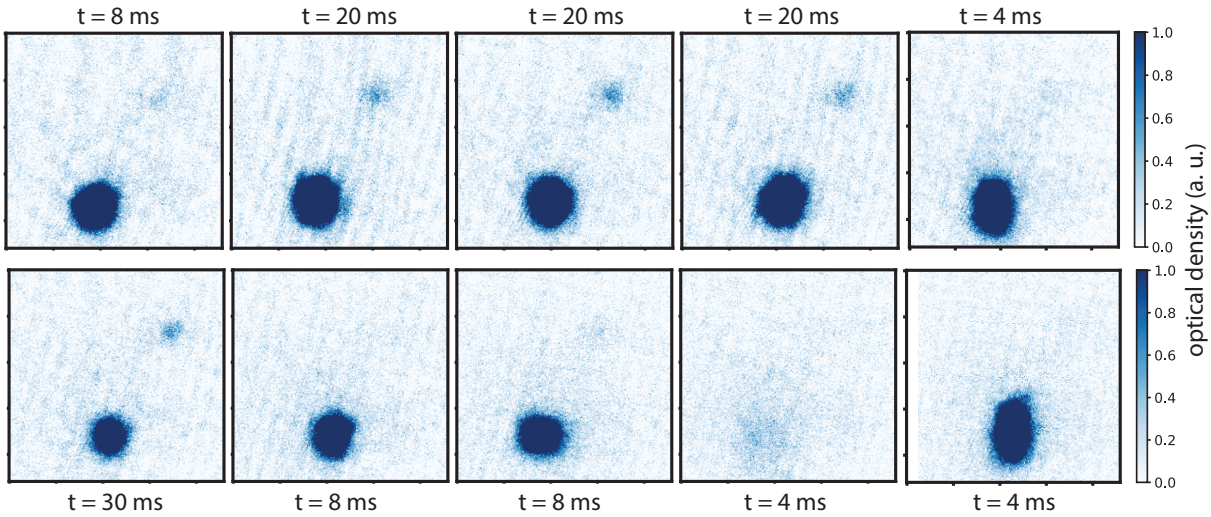

Figure 3.23: Absorption images of lithium from time evolution data set I. Images corresponding to the first 10 shots are displayed for visual inspection of the SCC process. The images are arranged based on the order in which they were taken. While the spin transfer is observed for an interaction time of as small as 4 ms, they are more pronounced at 20 ms and 30 ms. Several faulty shots occurred as well, such as the one at t= 4 ms in the bottom row, due to experimental imperfections (see text).

A careful visual inspection of the shots revealed that, 10-20% of the total number of shots were unusable due to the fact that the region of interest did not contain any atomic signal at all (see Fig. 3.23). This could have been due to any experimental imperfection that led to the escape of lithium atoms from the trap during the intermediate stages, and hence failing to form a BEC. Similarly, there existed yet another class of unusable shots where sodium was missing, or the superposition wasn't created as desired. All such shots were discarded before the preliminary analysis. The amount of lithium spin transfer, which is main observable of interest, is then calculated as $N_{0,L}/N_L$. It represents the fraction of atoms transferred with respect to the total number. Every data set was segregated according to the scan parameter, which in this case is the evolution time. The raw data is displayed in Fig. 3.24. For each value of interaction time, the mean of $N_{0,L}/N_L$ is displayed in Fig. 3.25. Two striking features are observed in Fig. 3.24 and Fig. 3.25: i) in both data sets, the spin transfer shows a sharp rise at early times, followed by an oscillatory behavior. The first maximum in the amplitude of the oscillation is found at 25 ms, followed by another maximum at 70 ms. The visibility however, falls after 40 ms indicating a damping at late times, ii) at a given evolution time, the shots are spread out upon repetition, indicating some kind of fluctuation. The results pertaining to the latter constitute the major part of chapter 4.

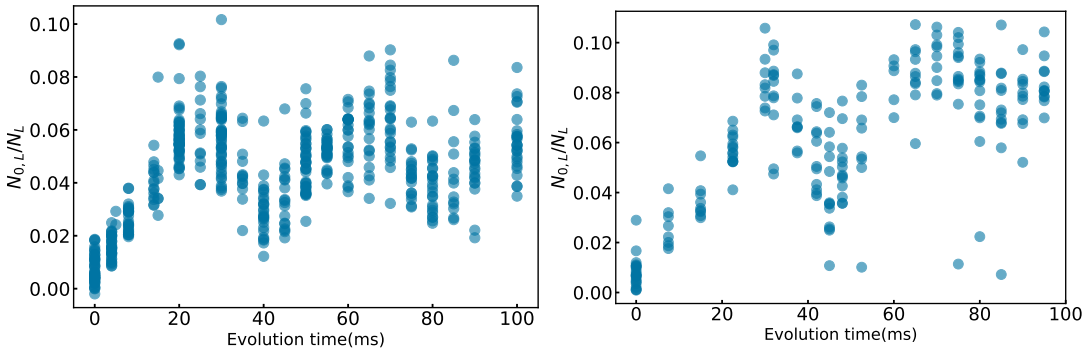

(a) Data set I, $\eta_0 = 0.407$ **(b)** Data set II, $\eta_0 = 0.293$

Figure 3.24: Analysis of the lithium absorption pictures of time evolution data set I and II. Every data point in blue represents one experimental run. These plots do not contain any data point corresponding to a faulty shot (see text). The atom number is calculated by evaluating the optical density in the region of atoms. The ratio of spin transfer in lithium is then calculated. The data is segregated and plotted as a function of the scan parameter, the evolution time.

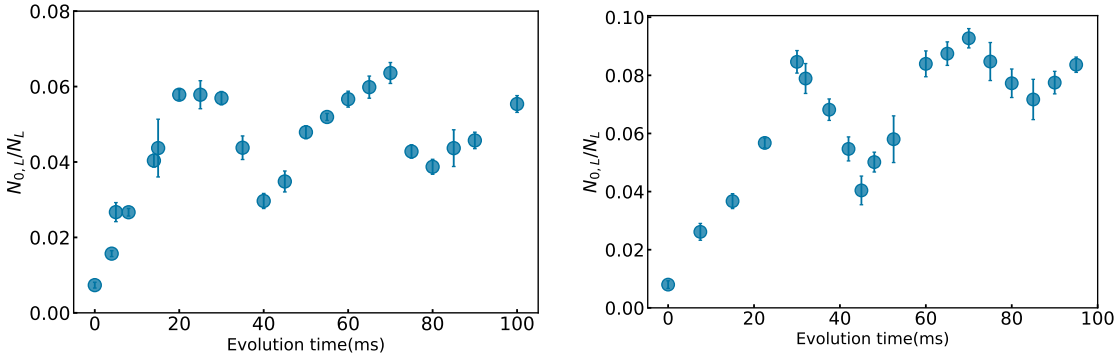

(a) Data set I, $\eta_0 = 0.407$ **(b)** Data set II, $\eta_0 = 0.293$

Figure 3.25: Mean spin transfer of lithium in time evolution data set I and II. Mean of $N_{0,L}/N_L$ follows an oscillatory trend as a function of evolution time. Rising sharply at initial times, the oscillations persist up to 100 ms. The amplitude of oscillation shows a reduction when approaching late times. The error bars are the standard errors on the mean.

The same analysis was repeated for the absorption pictures of sodium, where the optical density is calculated as displayed in Fig. 3.26. The figure reveals that the internal states of sodium show spatial distortions as they evolve in time, unlike lithium where the clouds seem to be intact. Moreover, the imbalance created in sodium is expected to stay constant for all the shots, and for all evolution times. However, the clouds in either states do not show such a perfect uniformity. It becomes more obvious when the ratio $N_{0,N}/N_N$ is evaluated from the images as shown in Fig. 3.27. In both data sets, the ratio decays over time.

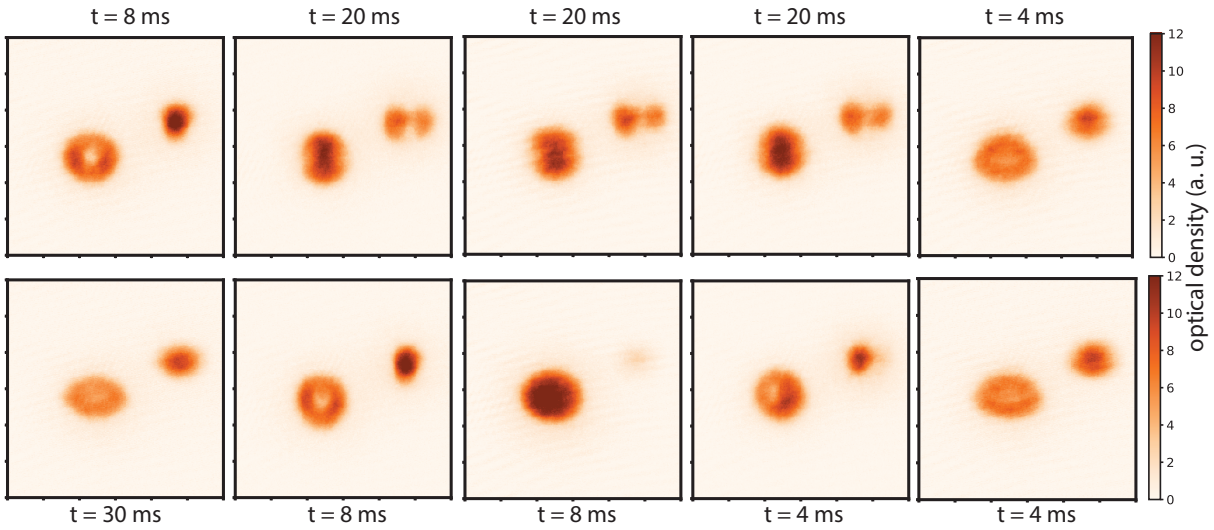

Figure 3.26: Absorption images of sodium from time evolution data set I. Sodium states evolve differently compared to lithium. When quenched into superposition and allowed to remain so throughout the evolution time, $|1,1\rangle$ state of sodium clearly exhibits some spatial dynamics (see text). It was also found that $|1,0\rangle$ decays over time with a lifetime of 500 ms (see subsection in 3.2.5).

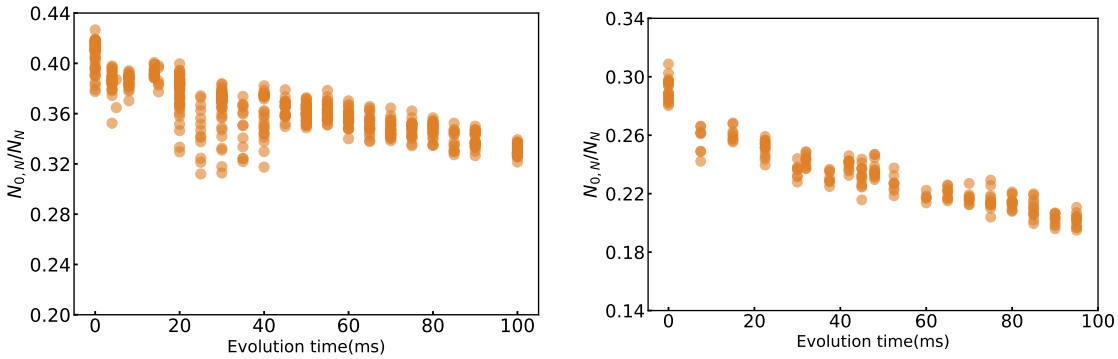

(a) Data set I

(b) Data set II

Figure 3.27: Analysis of the sodium absorption pictures of time evolution data set I and II. The ratio of atoms in the two spin states are evaluated as a function of evolution time. The imbalance η_0 is reduced over time due to the atom loss in $|1,0\rangle$ (see subsection in 3.2.5).

3.2.4 Imbalance measurements

Being able to scan the initial sodium imbalance is a very important aspect that reflects on the tunability of the experiment, as it represents the different values of the gauge field L_z. In these types of measurements, the sodium imbalance η_0 changed from shot to shot, ranging from 0 to 1. The evolution time was fixed to 30 ms. Imbalance data I was also taken at 2.118G. As the time evolution data from Fig. 3.25 quite clearly indicates a near maximum amplitude of spin transfer in lithium at 30 ms, this was chosen for the rest of the measurements involving the scan of η_0. The time evolution measurements, being the first ones taken, indicated that repetitive shots with supposedly the same η_0 do not actually contain the same imbalance ratio. This could be due to several reasons, such as fluctuations in the offset field, or in the properties of the first pulse in the two-pulse sequence which creates the superposition. Hence, the lithium

data obtained from all the imbalance scans was grouped prior to analysis. The ratio $N_{0,N}/N_N$ was evaluated for every shot, followed by binning using 40 equidistant bins. The lithium ratio was then grouped accordingly, thus rewriting the scan parameter as a binned scale η_0.
For smaller values of η_0 up to 0.2, only 20% of the total sodium atoms are $|1,0\rangle$ and hence the spin transfer in lithium is quite low. However, it shows a steep increase at $\eta_0 = 0.2$, followed by a rather consistent drop towards the larger η_0 where most sodium atoms are in $|1,0\rangle$.

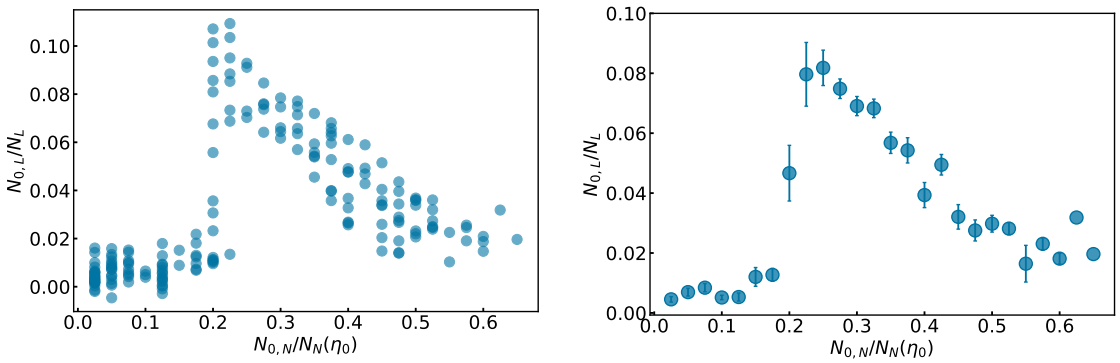

(a) Raw data, B=2.118 G

(b) Mean spin transfer

Figure 3.28: Analysis of imbalance data set I. Different initial states are created in sodium, by scanning the duration of the first pulse. The evolution time is kept fixed at 30 ms. The lithium data is binned according to sodium data, and hence, the spin transfer in lithium is plotted as a function of the binned sodium imbalance η_0. The observed spin transfer shows a sudden rise at $\eta_0 = 0.2$.

3.2.5 Magnetic field measurements

The previous two types of measurements were performed with a fixed magnetic field of 2.118 G. Scanning through the evolution time and initial state exposed the trend of inter-species interaction, and provided the first insights into the spin dynamics in different parameter regimes. The magnetic field was yet another well controlled quantity, and a possible channel to understand how such an interaction would look like at a slightly different field. To this end, six different measurements were performed at varying magnetic field values. Prior to every such measurement, the two pulse-sequence was re-calibrated to create the right imbalance in sodium, owing to the change in Zeeman splitting between the internal states. The sodium imbalance was scanned again as explained in section 3.2.4, keeping the evolution time fixed to 30 ms. Fig. 3.30-Fig. 3.33 show that a decreasing magnetic field also decreases the amount of spin transfer in lithium. Moreover, the peak of the resonance feature shifts to smaller η_0.

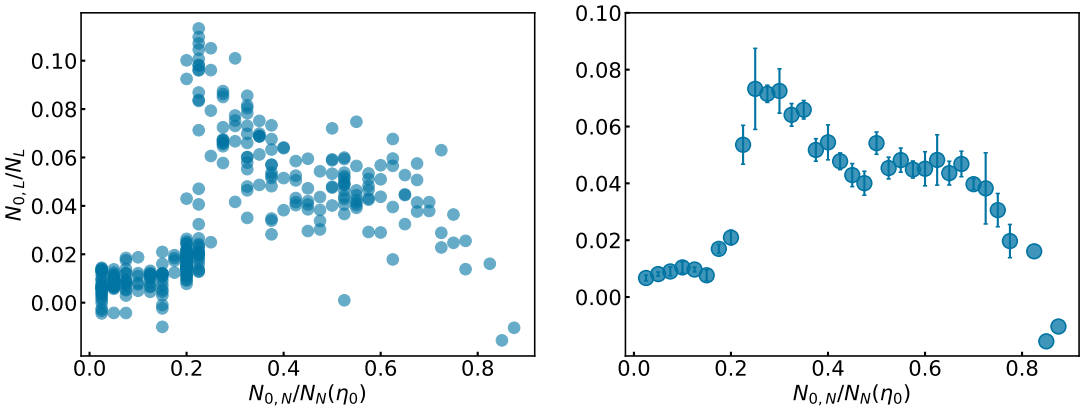

Figure 3.29: Offset field = 2.137 G

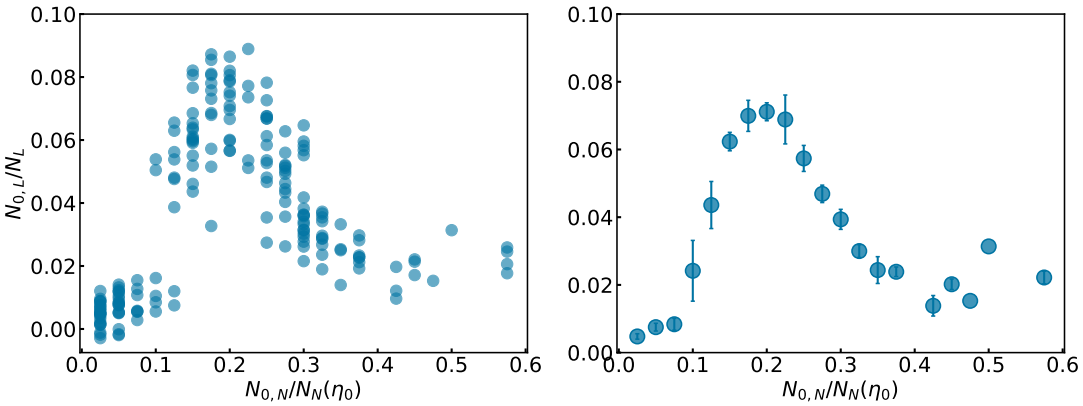

Figure 3.30: Offset field = 2.068 G

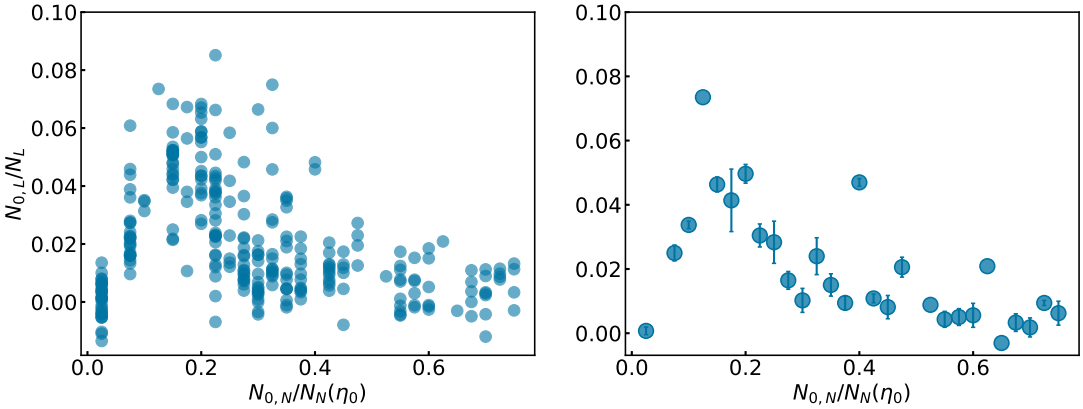

Figure 3.31: Offset field = 2.019 G

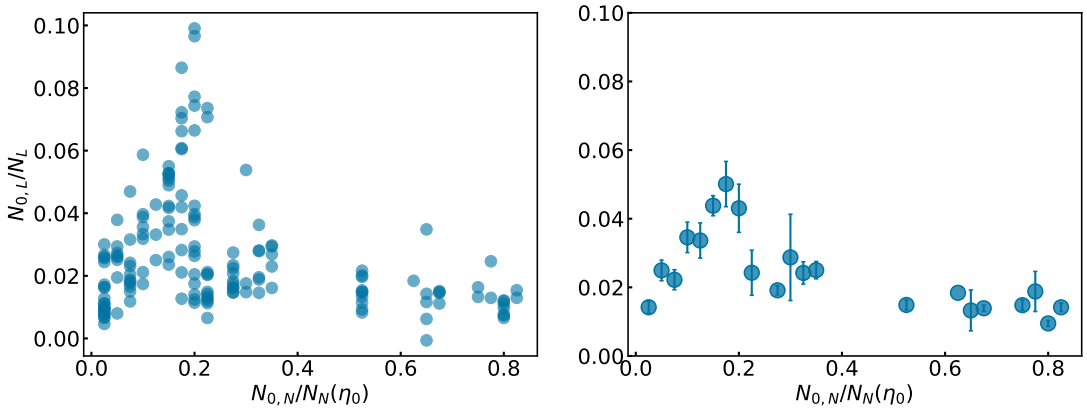

Figure 3.32: Offset field = 2.009 G

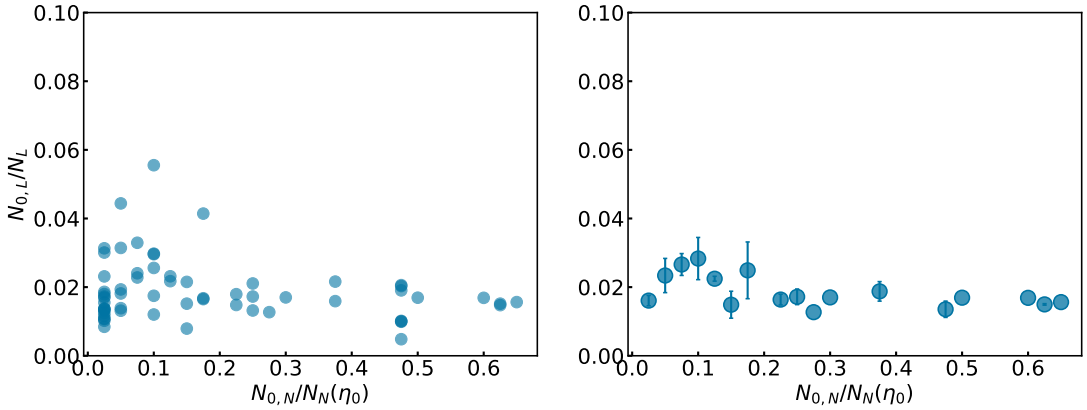

Figure 3.33: Offset field = 1.968 G

Remarks on experimental observations

- The spatial dynamics in sodium as shown in Fig. 3.26 occurred in all the measurements and it was observed only when the internal states of sodium were in superposition. Whenever the $|1,0\rangle$ state was densely populated, $|1,1\rangle$ showed a ring like structure where its central region was devoid of atoms and vice versa. The timescale of such a deformation was faster compared to the time scales of SCC. Moreover, the shape of deformation changed with evolution time. This behavior was attributed to the *miscibility* condition, that occurs due to the intra-species interaction between the two components of the condensate[139]. It is spin dependent, and can be ferromagnetic or antiferromagnetic depending on the scattering lengths of the internal states. This makes the states either miscible or immiscible. In the latter case, the components avoid each other. The sodium states used to simulate SCC happen are immiscible, with the criterion,

$$\sqrt{g_{11}g_{10}} > g_{10}^2 \tag{3.4}$$

where index notations of interactions strengths is specified as given in the microscopic description in section 2.5.1. The numerical simulation performed to obtain the ground states of mean field GPE also correctly predicted the onset of such a separation[81]. More details on the experimental studies in this regard are explained in[84].

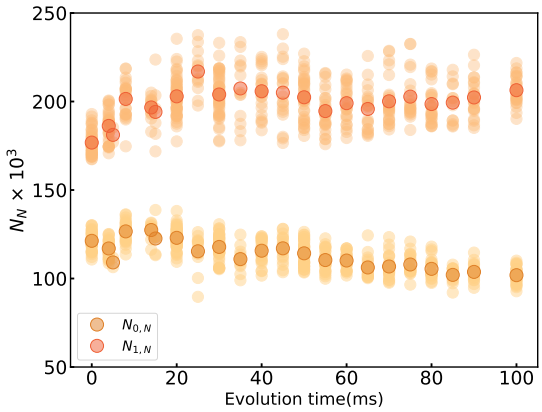

Figure 3.34: Technical fluctuation and atom loss in sodium components for the time evolution data corresponding to $\eta_0 = 0.407$. The number of atoms present in each cloud is plotted as function of evolution time. While the atom number in $m_F = 1$ (red circles) fluctuates from shot to shot, the overall mean doesn't decay. The atom number in $m_F = 0$ (orange circles) on the other hand shows a reduction in the mean due to atom loss at longer evolution times.

- Loss of atoms was observed in the $|1, 0\rangle$ state of sodium, leading to a fluctuating η_0 in the case of time evolution measurements. An exponential curve fit to the data seen in Fig. 3.27 deduced a lifetime of ≈ 508 ms (Data set I) and ≈ 240 ms (Data set II).
- As discussed in the previous sections, lithium atoms undergo the spin transition because of sodium atoms, which act as the mediator by undergoing the exact opposite transition as depicted in Fig. 2.4. However, such a relative change in sodium was not resolvable due to the fact that its a large cloud, where the order of magnitude of the spin change is much lower than in lithium. In addition, due to the spatial dynamics and the atom loss of the spin states, it was not possible to get systematic hold on it.

3.3 Summary

- This chapter was dedicated primarily to the technical aspects, such as experimental setups and sequences used to generate the SCC data. Different stages of sequential cooling and trapping that were employed to reduce the temperature of the thermal gases of $^{23}\mathrm{Na}$ and $^{7}\mathrm{Li}$ were discussed. Furthermore, it was shown how the condensates were obtained in the same ODT, thereby stressing the importance of their spatial overlap. Imaging techniques and calibrations were revisited, which resulted in a faithful determination of the final atom numbers contained in both the clouds to be $\approx 300\times 10^3$ (sodium) and $\approx 35\times 10^3$ (lithium).

- The techniques to manipulate the internal states $|1,1\rangle$ and $|1,0\rangle$ were described, as this is crucial to the realization of the QS. The steps undertaken to facilitate the SCC interaction were discussed such as,

  1. The scheme for tuning and stabilizing the external magnetic field to ≈1.95 G, where the magnitude of the Zeeman splitting between $m_F = 0$ and $m_F = 1$ is the same for both the species.
  2. The method for creating an appropriate initial state in sodium, i.e., a superposition of the two internal states, which corresponds to the gauge field term. The underlying scheme of a two-pulse sequence was discussed, along with its technical implementation with a programmable MW setup.

- The experimental sequence to realize SCC dynamics was described. Starting from an initial condition, where the lithium is fully polarized in $m_F = 1$, and sodium in superposition, the two were species shown to interact, resulting in SCC. Such a mediated interaction was attributed to the realization of Gauss' law in the bulk BEC. The measurements undertaken to explore different parameter regime were described. They highlighted the control and tunability of the experiment. To that end, it was shown how the SCC resonance manifested itself when the sodium imbalance η_0 was scanned. Moreover, the robustness of the gauge invariance was demonstrated through magnetic field measurements, where it was clearly seen that the SCC resonance shifted to smaller η_0 with decreasing magnetic field.

- Raw images taken using TOF absorption imaging were shown for visual inspection. They revealed other rather undesired processes where the $|1,1\rangle$ state of sodium developed spatial structures due its immiscibility condition with $|1,0\rangle$, while the latter underwent losses.

- All the raw data was displayed, and a noticeable observation was that the spin transfer in lithium $N_{0,L}/N_L$ exhibited fluctuations up to a maximum of 4% of the total $N_{0,L}/N_L$. It could be seen that the effect is particularly strong at the resonance flank in the case of imbalance measurements. The quest to understand the origin of these fluctuations hence paved the way to an extended data analysis presented in the next chapter.

Chapter 4

Data analysis and results

This chapter presents the theoretical description of the data acquired in the SCC experiment. All the raw data is displayed in the last section of the previous chapter. The first part here is dedicated to a brief explanation of the main results obtained from the previous analysis based on mean field theory[84]. Starting from the coupled spin Hamiltonian described in section 2.5.2, the analysis provided the first faithful representation of the experiment. The equations of motion for the evolution of the individual spin components of both species were derived from the Hamiltonian. Furthermore, they were numerically solved, thereby providing a physical picture to describe the data. Having briefly discussed the mean field approach, the raw data is revisited to emphasize that there are certain aspects such as fluctuations in the lithium spin transfer ratio, that require further attention. The remaining sections are further divided into two parts. They begin with data analysis, where the raw data is subjected to detailed inspection with respect to fluctuations observed in experimental parameters such as initial atom numbers in the BEC and the fluctuations in sodium imbalance. These are nothing but spin length and spin projection fluctuations respectively. Their consequences on the mean field representation and the model parameters are evaluated. Furthermore, a classical statistical method is employed in the form of truncated Wigner method, where the fluctuations are deliberately included in the initial state. The resulting predictions are compared with the data to draw conclusions on the nature and origin of the fluctuations. In the final section, different types of interpretations of the data are explored, such as long time behavior of the system, followed by a basic discussion on thermal fluctuations in the context of classical thermodynamics.

4.1 Simple mean field approximation

The evolution of spin operators was investigated in order to understand the interspecies SCC dynamics. Starting from the effective spin Hamiltonian given in equation (2.68), equations of motion for all the spin operators were derived via a Heisenberg-type equation. Using the relations $\hat{L}_+ = \hat{L}_x + i\hat{L}_y$ and $\hat{L}_- = \hat{L}_x - i\hat{L}_y$, the equation (2.68) was rewritten as,

$$\hat{H}_{spin}/\hbar = \chi \hat{L}_{z,N}^2 + \Delta \hat{L}_{z,L} + 2\lambda \left(\hat{L}_{x,N}\hat{L}_{x,L} + \hat{L}_{y,N}\hat{L}_{y,L} \right) \tag{4.1}$$

In its simplest approximation, this theory assumed the mean-field limit. The operators were replaced by their expectation values in the limit of $N \to \infty$ and the $1/\sqrt{N}$ uncertainty was neglected. Within this framework, the Ehrenfest theorem was employed to derive the equations

of motion for the spins,

$$\partial_t L_{x,N} = -2\chi L_{z,N} L_{y,N} + 2\lambda L_{z,N} L_{y,L} \tag{4.2a}$$
$$\partial_t L_{y,N} = 2\chi L_{z,N} L_{x,N} - 2\lambda L_{z,N} L_{x,L} \tag{4.2b}$$
$$\partial_t L_{z,N} = 2\lambda (L_{y,N} L_{x,L} - L_{x,N} L_{y,L}) \tag{4.2c}$$
$$\partial_t L_{x,L} = -\Delta L_{y,L} + 2\lambda L_{z,L} L_{y,N} \tag{4.2d}$$
$$\partial_t L_{y,L} = \Delta L_{x,L} - 2\lambda L_{z,L} L_{x,N} \tag{4.2e}$$
$$\partial_t L_{z,L} = 2\lambda (L_{y,L} L_{x,N} - L_{x,L} L_{y,N}) \tag{4.2f}$$

A noticeable feature in the data displayed in section 3.2, Fig. 3.25 is that the experimentally observed oscillations exhibit damping at later times. While the processes such as spatial dynamics, atom loss, and fluctuations in the experimental parameters are few of the many possible reasons for the damping, it is hard to locate the underlying cause exactly. Hence, this was effectively accounted for by introducing a phenomenological damping term γ in the theory. It was conceptually treated as dephasing of spins in the x-y plane with a decay rate given by γ. The equations were then modified as,

$$\partial_t L_{x,N} = -2\chi L_{z,N} L_{y,N} + 2\lambda L_{z,N} L_{y,L} - \frac{\gamma}{2} L_{x,N} \tag{4.3a}$$
$$\partial_t L_{y,N} = 2\chi L_{z,N} L_{x,N} - 2\lambda L_{z,N} L_{x,L} - \frac{\gamma}{2} L_{y,N} \tag{4.3b}$$
$$\partial_t L_{z,N} = 2\lambda (L_{y,N} L_{x,L} - L_{x,N} L_{y,L}) \tag{4.3c}$$
$$\partial_t L_{x,L} = -\Delta L_{y,L} + 2\lambda L_{z,L} L_{y,N} - \frac{\gamma}{2} L_{x,L} \tag{4.3d}$$
$$\partial_t L_{y,L} = \Delta L_{x,L} - 2\lambda L_{z,L} L_{x,N} - \frac{\gamma}{2} L_{y,L} \tag{4.3e}$$
$$\partial_t L_{z,L} = 2\lambda (L_{y,L} L_{x,N} - L_{x,L} L_{y,N}) \tag{4.3f}$$

4.1.1 Model parameters for fixed initial atom numbers

The interaction dynamics that originate from the above equations of motions is essentially governed by the microscopic model parameters χ, Δ and λ (see section 2.5.1):

- $\boldsymbol{\chi}$: contains interaction strengths for inter-species and intra-species non-SCC interactions.
- $\boldsymbol{\lambda}$: contains inter-species SCC interactions strength. It stems directly from the overlap integral given in equation (2.57). Hence, for fixed values of the atom numbers and the trapping potentials, this quantity is assumed to be fixed, i.e. any changes in the spatial modes of the atomic clouds were neglected.
- $\boldsymbol{\Delta}$: defines the energy offset in terms of Zeeman splitting of the two internal states (see Fig. 2.4); to this end, it was necessary to differentiate the different contributions as they proved to be crucial from the point of view of tunability. By rearranging (2.70), the expression for Δ is re-written as,

$$\begin{aligned} \Delta &= \Delta_0 + \Delta_L \frac{L_{z,N}}{L_N}(t=0) + \Delta_B \frac{(B - B_0)}{B_0} \\ &= \Delta_0 + \Delta_L (2\eta_0 - 1) + \Delta_B \frac{(B - B_0)}{B_0}; \quad (B_0 = 2.118G) \end{aligned} \tag{4.4}$$

While Δ_0 is a fixed quantity for fixed atom numbers, the remaining terms highlight the tunability of the experiment. For instance, the scan of the initial condition η_0 as discussed in section 3.2.4 is equivalent to scanning the $L_{z,N}$ term (see section 3.2.1 for technical implementation). Similarly, the third term accounts for the energy shifts caused by a change in the applied offset field as it was done in the experiment (see section 3.2.5).

These parameters were first estimated from first principles, given the relevant experimental parameters such as trapping frequencies and atom numbers. By determining the ground state wave functions, the density distributions of the two species were obtained, which were further used to calculate the overlap integrals presented in equations (2.57). A rigorous discussion on ab-initio estimates is found in [84]. A second method of parameter estimation was closely developed through the standard curve fitting procedure. Equations (4.3a)-(4.3f) were numerically solved and the model parameters were obtained from the best fitting curve between theory and data. The numerical simulation contained the following aspects:

- The initial atom numbers were treated as fixed quantities,

$$N_N = 300 \times 10^3 \quad ; \quad N_L = 35 \times 10^3.$$

- The initial magnetization is assumed to be fixed for a given population imbalance in sodium. Since lithium is polarized in $m_F = 1$ prior to the time evolution, its initial value of the z-component is treated like a fixed offset and is given by $L_{z,L} = -L_L = -N_L/2$.

- The initial conditions for the simulations are appropriately chosen,

$$(L_{x,L}, L_{y,L}, L_{z,L})_{t=0} = (0, 0, -1)\times L_L \quad ; \quad (L_{x,N}, L_{y,N}, L_{z,N})_{t=0} = (\cos\theta, 0, \sin\theta)\times L_N$$

  where the value is $\theta = [-\pi, \pi]$ is decided according to the initial superposition quench.

- The damping γ was estimated to be $\gamma/2\pi = 3.9 \pm 1.2$Hz by fitting an exponential decay to the data shown in Fig. 3.25a.

- Following the numerical evolution of the spin components, the transfer ratio in lithium $N_{0,L}/N_L$ was calculated as,

$$N_{0,L}/N_L = (L_{z,L} + L_L)/N_L \tag{4.5}$$

- The protocol for parameter estimation was done in the following way: the imbalance data set shown in Fig. 3.28b was fitted to extract χ, Δ_0, Δ_L and λ. These values were then used as initial guesses for the mean field prediction for the time evolution data shown in Fig. 3.25. With all these values fixed, a second fitting procedure was performed to determine Δ_B. The resulting values are summarized in table 4.1.

Parameters	Time evolution Data set I	Time evolution Data set II	Imbalance Data
$\chi/2\pi$ (mHz)	9.52 $\pm$ 0.09	9.525$\pm$0.00023	9.559$\pm$0.010
$\lambda/2\pi$ (μHz)	17.6$\pm$ 1.0	18.7$\pm$0.8	16.7$\pm$0.5
$\Delta_0/2\pi$ (Hz)	2$\pm$7	2$\pm$7	3.9$\pm$2.1
$\Delta_L 2/\pi$ (kHz)	2.919$\pm$ 0.017	2.919$\pm$ 0.017	2.9168$\pm$ 0.00015
$\Delta_B 2/\pi$ (Hz)	-517.10$\pm$ 0.28	-517.10$\pm$ 0.28	-519.3$\pm$ 0.3

Table 4.1: Values of model parameters. These are the results of the fitting procedure as described in the main text.

4.1.2 Results of numerical simulations of SCC

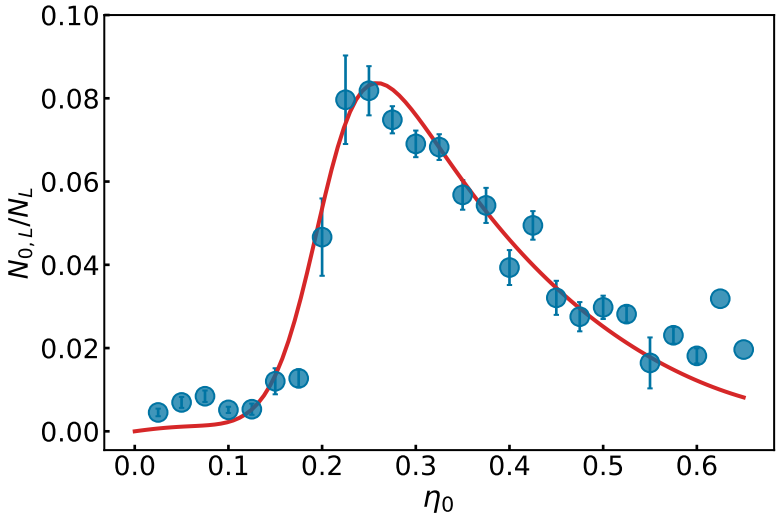

Figure 4.1: Scan of initial sodium imbalance η_0 and comparison with mean field predictions. The data shown in Fig. 3.28b is fitted with equations (4.3a) - (4.3f) (solid red line). The sharp resonance feature observed around $\eta_0 \approx 0.2$ in the data is well explained by the numerical result. The parameters χ, λ, Δ_L and Δ_0 are extracted from the best fitting simulation.

The resonance manifested in the form of an initial sharp rise followed by a reduced transfer towards higher imbalance values is captured very well by the mean field theory. The parameters thus obtained also successfully capture the oscillatory behavior observed in the time evolution dynamics, see Fig. 4.2. The reduced visibility therein is also accounted qualitatively by γ. The damping is the strongest in the first 40 ms of spin transfer dynamics, with the amplitude of the oscillation reducing from ≈ 0.06 to half as much. However, as the dashed lines in Fig. 4.2 indicate, the transfer ratio remains high at 30 ms where the imbalance data I was recorded. Hence, the damping term is not as critical for the imbalance data.

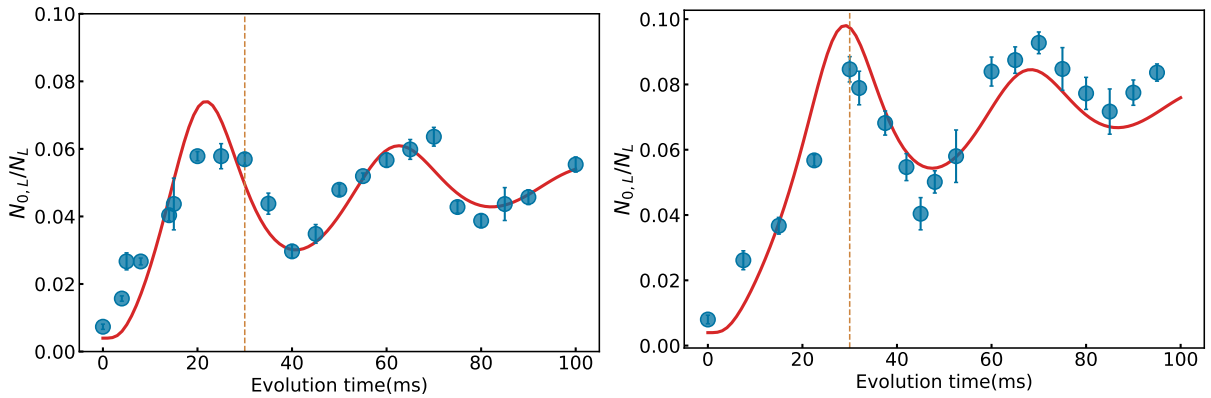

(a) Time evolution Dataset I, $\eta_0 = 0.407$

(b) Time evolution Dataset II, $\eta_0 = 0.293$

Figure 4.2: Comparing the time evolution measurements to the mean field predictions. The parameters extracted from Fig. 4.1 are used to predict the dynamics as a function of interaction time. With the damping term added, the theory predictions match the data reasonably well.

The remaining data sets at various magnetic field values as outlined in section 3.2.5 were subjected to similar theoretical treatments. The distinct shape of spin transfer, i.e., the resonance condition is prevailed at all magnetic field values. Remarkably, the resonance peak shifts towards either lower or higher imbalance values with respect to decreasing or increasing values of magnetic field. This agrees perfectly well with the resonance condition (2.76) of the coupled spins, that a change in Δ demands a change in $L_{z,N}$. Going back to the HEP model of U(1), scanning Δ is analogous to scanning the mass term and associated with it is the changing gauge field. Hence, it shows that this is in excellent agreement with the gauge invariance principle. Moreover, in accordance with the conservation of magnetization, the amplitude of the observed transfer is consistently reduced when the resonance peak is moved closer to smaller η_0. The coefficient of change with respect to the offset field is given by Δ_B, which is determined by yet another fit to the curves shown in Fig. 3.29 - Fig. 3.33. As the other parameters χ, λ, Δ_0 and Δ_L are kept constant in this fitting, the change in the magnetic field value in all the data sets is accounted for only by Δ_B.

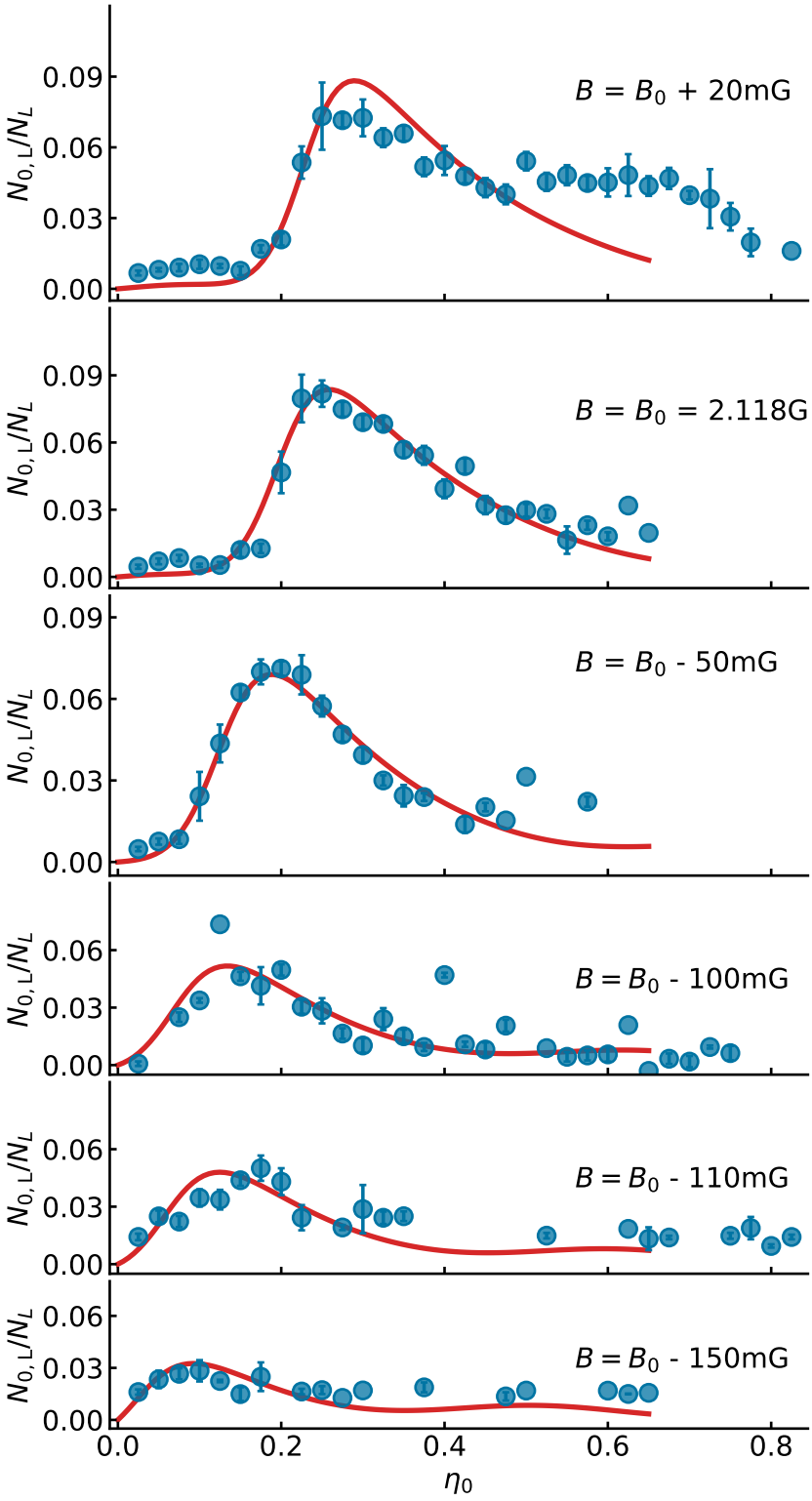

Figure 4.3: Mean field predictions for the imbalance scans at different values of offset field B. The fitting procedure is the same as in Fig. 4.1, with the addition of Δ_B that accounts for the changes in the total Δ with respect to the value of the magnetic field. Mean field predictions (solid red lines) clearly capture the onset of resonance for all the data sets. Moreover, shifting of the resonance feature where the peak moves to the left (right) for decreasing (increasing) field values is also captured by the theory. Furthermore, the reduction in the amplitude of the peaks due to the conservation of magnetization is also captured.

4.2 Fluctuations: data analysis

This section addresses the fluctuations observed in the raw experimental data presented in section 3.2. Throughout this thesis, the fluctuations are quantified by extracting the standard deviation of the spin transfer ratio in lithium $N_{0,L}/N_L$, with respect to the scanned parameters. The error bars on the std values are the results of the error propagation of numbers with uncertainties. These fluctuations persist at all interactions times and imbalances. Comparing Fig. 4.1 and Fig. 4.4a, it can be seen that the fluctuations spike up as high as half of the mean itself at the resonance peak where $\eta_0 = 0.2$, and reduce again towards smaller η_0. A similar comparison between Fig. 4.2a and Fig. 4.4b leads to the observation that the initial rise of $N_{0,L}/N_L$ at short evolution times is accompanied by an initial rise in the std as well. In this case, while the mean itself is damped at later times, fluctuations witness a fall and rise after 30 ms.

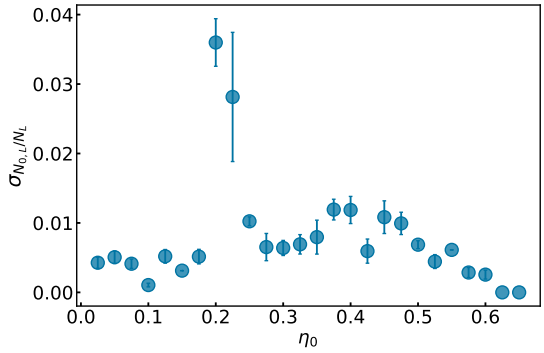

(a) Standard deviation of the imbalance data I. Fig. 3.28a displays the corresponding raw data.

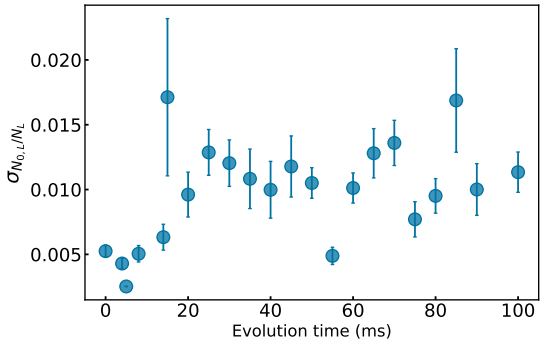

(b) Standard deviation of the time evolution data I. Fig. 3.24a displays the corresponding raw data.

Figure 4.4: Fluctuations observed in the spin transfer ratio of lithium $N_{0,L}/N_L$. The standard deviation is extracted from the corresponding raw data. **(a)** the imbalance data shows a strong rise exactly at the point of resonance, followed by a bumpy feature towards higher imbalances. **(b)** fluctuations in the time evolution data show an initial rise up to 30 ms, followed by a rather small change after that.

This section is organized as follows: detection noise present in the raw pictures of lithium is evaluated prior to all other investigations to show that the observed fluctuations are noticeably higher, and that it is not the result of the measurement procedure itself. Having shown that, the next section focuses on understanding the shortcomings of mean field theory with respect to fluctuations and aims to tackle the issue by exploring several possible sources of fluctuations in initial atom number fluctuations and in the spin projections.

4.2.1 Readout noise in lithium

An absorption image without an atomic signal does not contain any information but only the noise resulting from the detection procedure. Typically, it occurs due to interference fringes from the optics used in the setup, photon shot noise from the imaging light and the noise of the camera itself. These noise sources result in slightly incorrectly read atomic densities, which then contributes as readout noise. As explained in section 3.2, defringing already reduces the detection noise greatly. However, the fluctuations are observed despite of defringing. To estimate the level of detection noise relative to the experimental data, the atom number is calculated in the empty, defringed pictures of lithium from the imbalance data set using the

saturated absorption formula given in equation (3.1). It varies slightly among the different data sets. Nevertheless, the estimation given by the example analysis here provides the right order of magnitude. Fig. 4.5a shows an image where both the atomic clouds are present and the ROIs shown are the same as those used in the original analysis presented in 3.2. This is an important consideration, because the detection noise is not homogeneous over the entire picture.

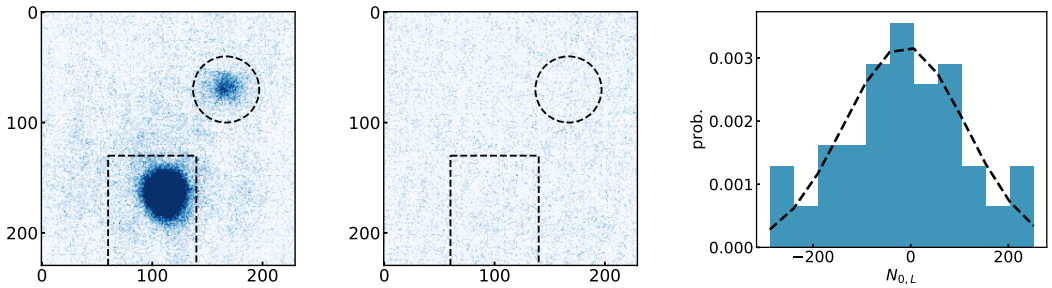

(a) Image with atoms.

(b) Image without atoms.

(c) Noise distribution of multiple empty images.

Figure 4.5: Readout noise analysis in lithium. **(a)** ROIs where the atoms are present are shown in the dashed rectangular box ($m_F = 1$) and dashed circle ($m_F = 0$). **(b)** ROIs for empty images are chosen exactly as in the images with atoms in panel **(a)**. Running the atom number evaluation routine with fixed imaging parameters for a series of empty images provides a rough estimate on the noise. **(c)** the detection noise approximately resembles a Gaussian distribution, displayed by the fit (black dashed) to the histogram.

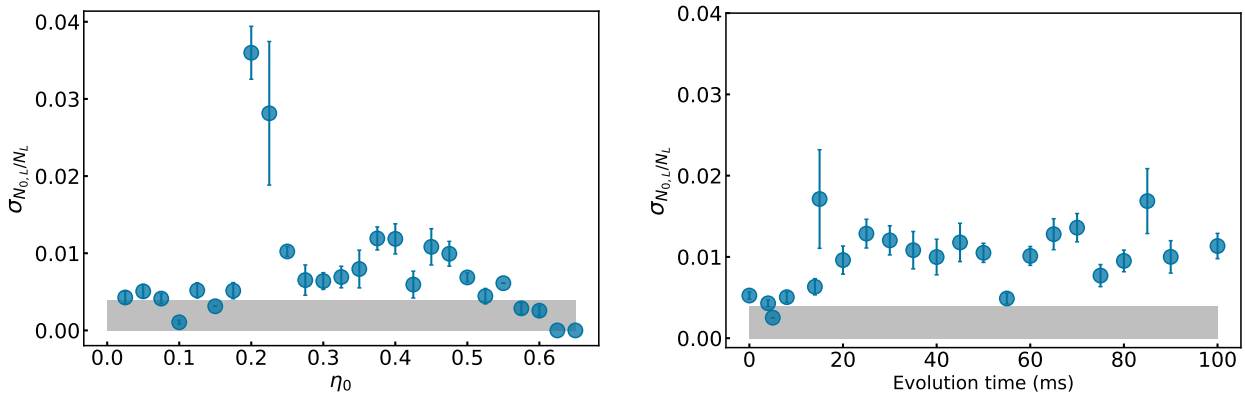

(a) Fluctuations in imbalance data set I with readout noise.

(b) Fluctuations in time evolution data set I with readout noise.

Figure 4.6: Comparing the level of readout noise to the observed fluctuations in $N_{0,L}/N_L$. The grey area represents the standard deviation of the noise distribution analysed from the empty images for each data set respectively. In both cases, the level of fluctuations observed in the data is clearly higher than the detection noise.

The observed level of fluctuations in Fig. 4.4a and Fig. 4.4b is compared against readout noise, see Fig. 4.6. In Fig. 4.6a, even though the data points at around $\eta_0 = 0.12$ and 0.6 are somewhat submerged in the noise floor, the rest of the key features, such as the high

std near the resonance region is clearly much above the level of readout noise. Moreover, a similar analysis on the time evolution data set I estimates a very similar value of readout noise, see Fig. 4.6b. It's important to note that this analysis is only meant to serve as an approximate method of estimating the readout noise and it does not claim the characterization of the imaging system in general.

4.2.2 Fluctuations in spin length

While mean field theory successfully explained the data on the mean field level by including an overall damping term, it fell inadequate in describing these fluctuations. This is due to the fact that shot-to-shot fluctuations as shown in section 3.2 were neglected. Even though the experiment setups are optimized to give an ideal performance in general, it seldom happens so in a real experiment. From a technical point of view, a few quantities that adversely affect the perfect operation of the experiments are fluctuations in laser powers, room temperature, coil currents, and so on. When deviated from their ideal values, they typically affect the loading of the MOTs. This is turn affects the intermediate processes involved in a BEC experiment, resulting in non-uniform condensate fractions, and varying atom numbers from shot to shot. Mean field theory described in section 4.1 treated the spin lengths, i.e., the initial atom numbers of N_N (sodium) and N_L (lithium) as fixed quantities, whereas they are spread out in the raw data sets. Their initial atom number distributions of both species exhibit a standard deviation of approximately 5-20%. It is rather nontrivial to draw a straightforward conclusion on how the mean field predictions would change in accordance with fluctuating initial conditions. Moreover, the original values of model parameters themselves differ slightly among different data sets (see table 4.1), which is all the more reason to investigate the underlying cause. A preliminary example is shown in Fig. 4.7 to stress that the behavior of the data is not reproduced anymore, even for the mean spin transfer, when the theory is subjected to fluctuating initial atom numbers.

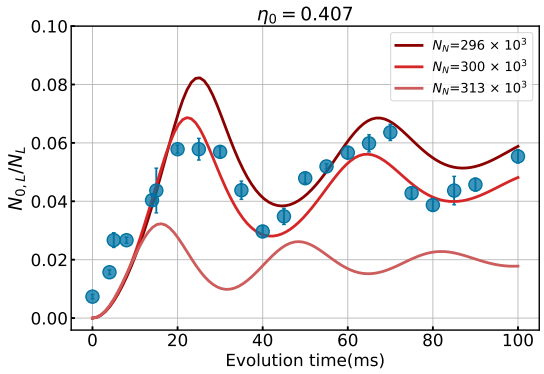

(a) Data set I with mean field prediction for varying N_N.

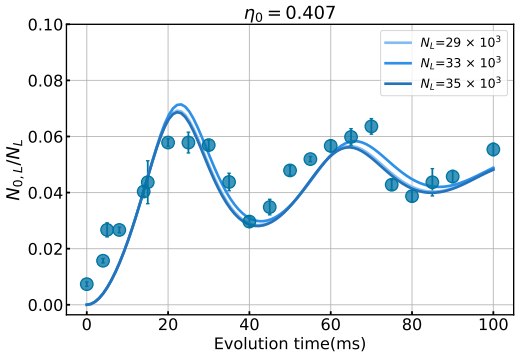

(b) Data set I with mean field prediction for varying N_L.

Figure 4.7: Mean field prediction with varying initial atom numbers. (a) the solid curves from top (solid brown), middle (red) to bottom (light red) correspond to different N_N in increasing order. The middle curve corresponds to the original as shown in Fig. 4.2a, where $N_N = 300 \times 10^3$. The values of N_N used in the top and the bottom curve then differ relatively by 2% and 5%. Such changes in the initial conditions not only lead to changes in amplitude of the mean field prediction, but also a shift in oscillation frequency. **(b)** the solid curves in light blue, blue, and dark blue correspond to different N_L in increasing order. N_L has negligible impacts on the mean field prediction, unlike N_N.

As displayed by the multiple bluish solid curves in Fig. 4.7b, the effect of varying lithium atom number is negligible, whereas a changing N_N has a relatively larger impact on the predictions of mean field theory, see Fig. 4.7a. This is also supported by the fact that N_N is much larger than N_L. Changes as small as 2% in N_N produce a noticeable change in the theory prediction, whereas a change of 5% leads to a drastic reduction in amplitude and even a shift in the oscillation frequency, that is not comparable with the data anymore. While this quick check clearly shows that the fluctuations in the initial atom number cannot be neglected, it also strongly indicates the need to perform this analysis on a quantitative level and hence provide a consistent and a more precise redefinition of the model parameters. To this end, the consequences of changing initial atom numbers are first explored via a post selection analysis of the experimental data.

4.2.3 Post selection of experimental data

The initial atom number measured in all experimental shots of all data sets form a distribution characterized by a mean and std, see Fig. 4.8. Here, shots are simply plotted with their respective atom numbers for both species, followed by their individual histograms to highlight the spread of the data points. The standard deviation in sodium is approximately 5.5% of mean N_N, while that of lithium is about 8% of mean N_L. The relatively fewer shots and the asymmetry of the distribution in lithium as shown in Fig. 4.8b is attributed to the fact that there exist more faulty shots in lithium than in sodium (see section 3.2 for explanations on raw data). The post selection alalysis was performed, first in sodium for the imbalance data set shown in Fig. 3.28a. To this end, two different methods were followed, as outlined below. Both methods employed the same first step, where the data shown in Fig. 4.8a was divided into different bands, with each band characterised by a certain offset and width. They were then separately analysed to calculate the lithium spin transfer ratio $N_{0,L}/N_L$ and its std.

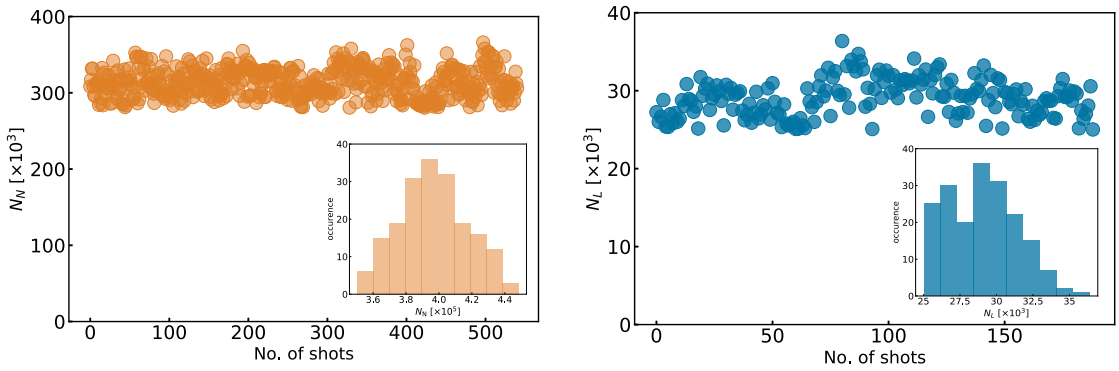

(a) Distribution of initial N_N.

(b) Distribution of initial N_L

Figure 4.8: Distributions of N_N and N_L for the imbalance data. The number of shots are plotted with respect to their measured atom number for both species. **(a)** the std of the distribution of initial N_N amounts to 5.5% of mean N_N, **(b)** the std of the distribution of initial N_L amounts to 8% of mean N_L.

Method I: Fixed mean, varying width

In the first method, the offset was fixed by the mean of the total distribution of N_N, and the width was increased in multiple steps of the standard deviation. This method is intended to investigate whether an increasing spread in N_N is directly responsible for driving the fluc-

tuations in $N_{0,L}/N_L$. However, the extracted ratio doesn't show any significant change in the level of fluctuations as a function of increasing width, see Fig. 4.10b.

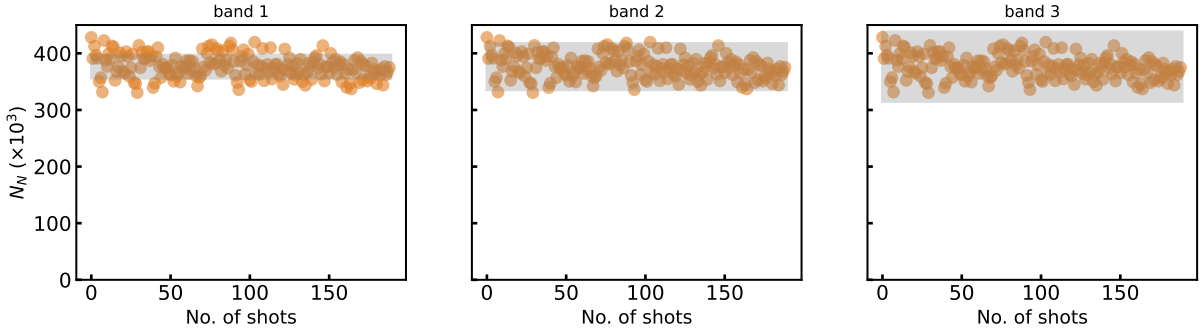

Figure 4.9: Dividing the imbalance data I into bands as per method I. The mean value of each band is determined by the mean of total N_N distribution. The width of the bands is varied from σ to 3σ.

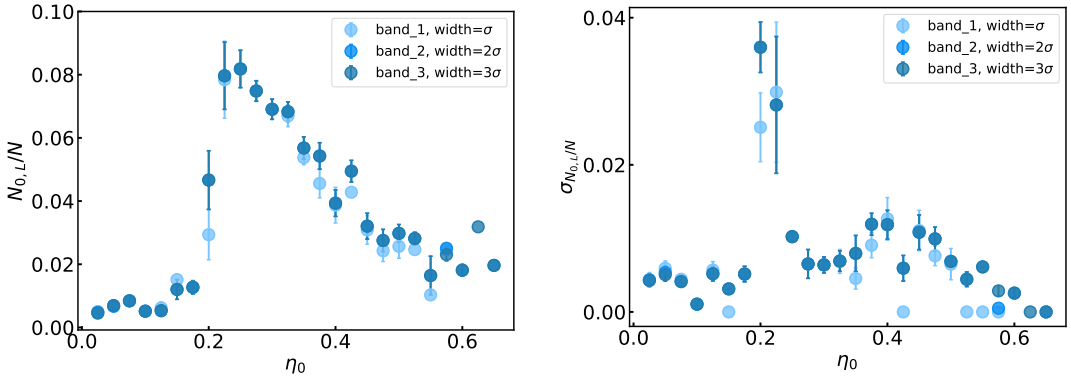

(a) Mean $N_{0,L}/N_L$ extracted for all the bands.

(b) Std of $N_{0,L}/N_L$ extracted for all the bands

Figure 4.10: Extracted statistical quantities for band data as per method I. (a) mean transfer ratio extracted from the bands of changing widths as shown in Fig. 4.10a. **(b)** stds of the ratios; neither of the images exhibits any change with respect to a changing width of the N_N distribution.

Method II: Fixed width, varying offset

The second method maintained a fixed width for each band, but varied the offset in order to change the mean of each band. In this case, the width of the bands was characterized by half the std of the total N_N distribution shown in Fig. 4.8a. The offset was changed in steps to move from the band with highest mean $\bar{N}_N$ to the one with the lowest $\bar{N}_N$ or vice versa. Hence, this method is intended to investigate the effect of varying the absolute N_N.

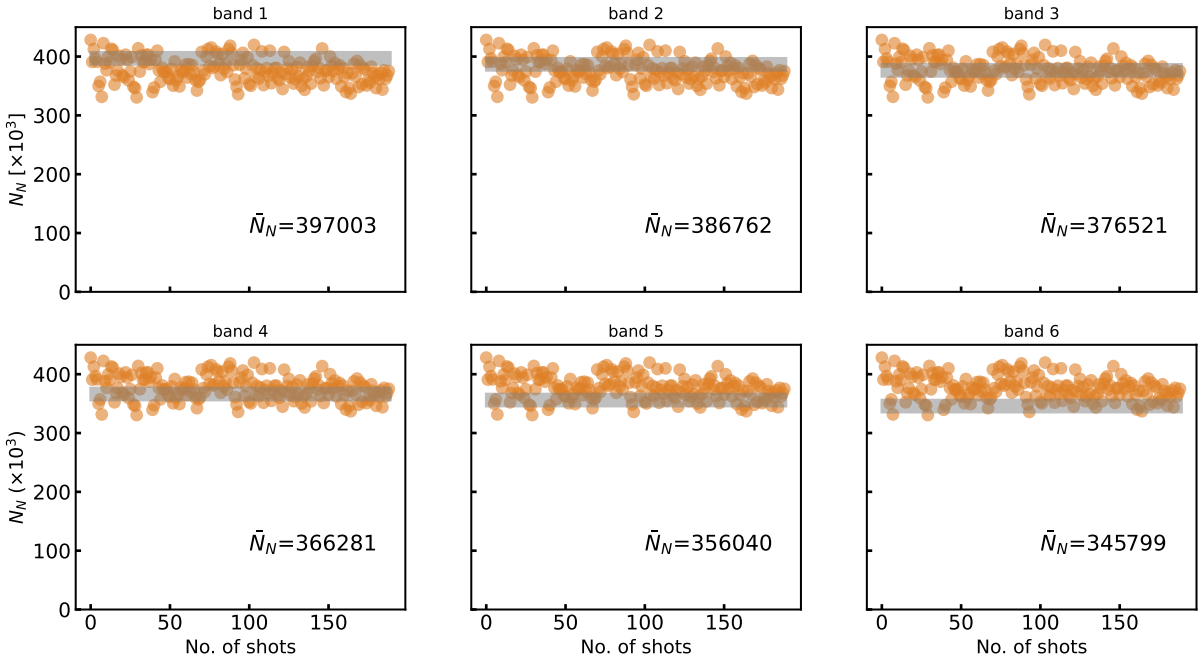

Figure 4.11: Dividing the bands in the imbalance data I as per method II. Here, the bands are characterized by a fixed width but varying offset. The width is fixed by half the std of the total N_N distribution and the offset is changed in fixed steps from band 1 to band 6. The mean atom number $\bar{N}_N$ of each band is displayed accordingly.

The statistics extracted through this method are displayed in Fig. 4.12. Even though the two plots do not seem to reveal any obvious information and look rather ambiguous, they show that the mean spin transfers extracted for individual bands slightly differ from each other, unlike in method I (see Fig. 4.10).

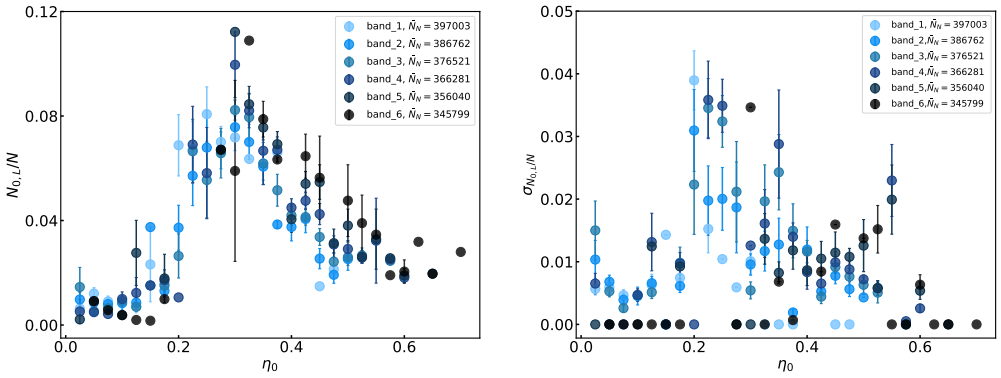

(a) Mean spin transfer $N_{0,L}/N_L$ **(b)** Std of $N_{0,L}/N_L$.

Figure 4.12: Extracted statistical quantities for band data as per method II. (a) mean transfer ratio $N_{0,L}/N_L$ extracted from the bands shown in Fig. 4.11. The mean seems to shift slightly from the highest N_N (light blue circles) to the lowest (black). **(b)** corresponding std. Bands 5 and 6 contain fewer shots compared to the rest, i.e., sometimes only one data point exists for given η_0, resulting in zero variance.

Overall, it is clear that a mere post selective inspection of the experimental data does not provide reliable insights. Hence, the same mean field theory described in section 4.1 was employed again, but selectively to each band in Fig. 4.11. To this end, the same fitting routine

used for Fig. 4.1 was performed on the mean $N_{0,L}/N_L$ pertaining to each band as shown in Fig. 4.12. For every band, the fitting functions were fed with relevant N_N, whereas N_L was fixed by the mean value of the total distribution N_L. Furthermore, the initial guesses for the parameters were changed from band to band to obtain the best agreement between theory and data, see Fig. 4.13. Band 5 and 6 suffer from scarce data points near the resonance flank. Nevertheless, the fits are reasonable, in the sense that they describe the tail region of higher η_0 well. Moreover, the steepness of the flank is not greatly altered. This analysis reveals a critical aspect about the model parameters, which was otherwise hidden when N_N was a fixed quantity. Examining the resulting fitting parameters from all the bands with respect to the changing N_N shows that the parameters Δ_L and Δ_0 are linearly dependent on N_N. The resulting dependence is summarized in table 4.2:

Parameter	Dependence on N_N
$\Delta_L/2\pi$ (Hz)	$N_N \times 0.00961 \pm 12.4$
$\Delta_0/2\pi$ (Hz)	$N_N \times (-2.10 \times 10^{-4}) + 6.68 \pm 0.5$
$\chi/2\pi$ (mHz)	9.429 ± 0.003
$\lambda/2\pi$ (μHz)	17 ± 0.5 (time evolution data), 13 ± 0.3 (imbalance data)

Table 4.2: Revised values of parameters with fluctuations included in the theory. The parameters Δ_0 and Δ_L have a linear dependence on N_N. No such behavior is seen in χ. The values of N_N between time evolution data and the imbalance data differ $\approx 25\%$, which causes λ to change. However, this dependence is not revealed in the post selection analysis (see text).

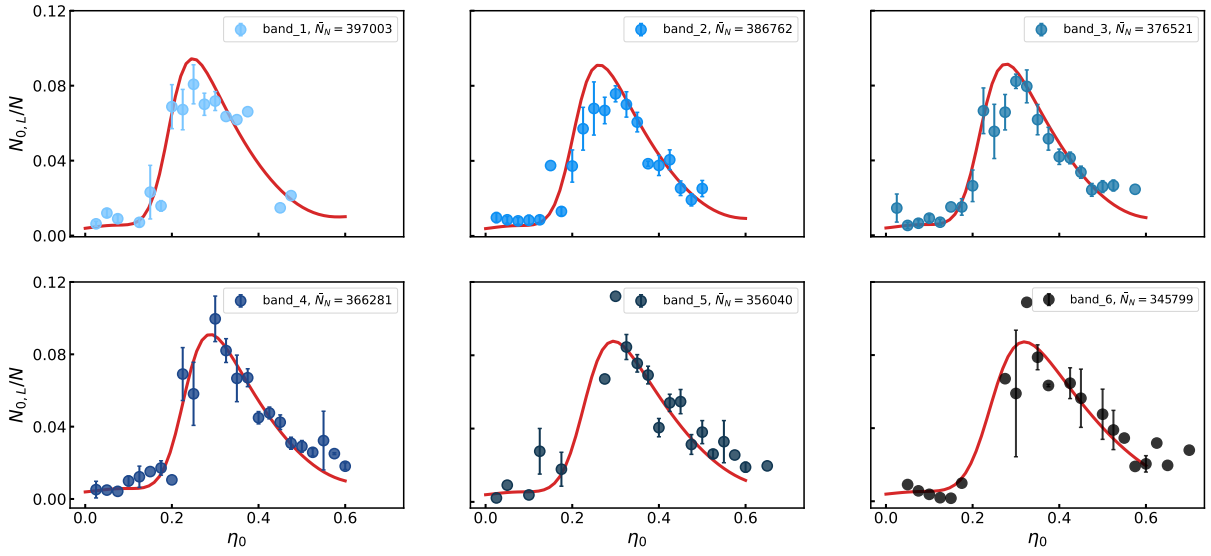

Figure 4.13: Mean field fits on the bands described in method II. The band data is displayed from top left (light blue) to bottom right(black). Solid red curves are the results of the mean field fits. The fitting routine for each band takes the respective mean $\bar{N}_N$, while N_L is fixed at its mean value $\approx 29 \times 10^3$. The initial guesses for the parameters are modified for each band to produce a best matching prediction of $N_{0,L}/N_L$.

In fact, the simplified expression for Δ given in equation (4.4) in section 4.1.1 is not particularly insightful in this regard, because fixing atom numbers is the very reason it is simplified.

The dependence is explicitly seen already at a more basic level by revisiting equation (2.70) and re-arranging the expression:

$$\Delta = \delta^N_{ext} - \delta^L_{ext} - \delta^L_{int} + \frac{\chi_{NL}}{2} N_L + 2\hat{L}_{z,L}\left(\chi_L + \frac{\chi_{NL}}{2}\right) + \chi_N(N_N - 1) - \frac{\chi_{NL}}{2} N_N + 2\hat{L}_{z,N}\left(\chi_L + \frac{\chi_{NL}}{2}\right) \tag{4.6}$$

where $\delta^s_{ext} = (E_{s,1} - E_{s,0})$ is the single particle energy difference for species s and $\delta^s_{int} = [X^s_{11} - X^s_{00}](N_s - 1)$ is the respective mean field shift. Such a dependence on N_L is not seen in the post selection analysis performed on lithium. The rest of the parameters of the spin Hamiltonian as described in section 2.5.1 do not show any such clear dependencies. The values of χ resulting from the fits shown in Fig. 4.13 are averaged to get the final value, see table 4.2. As per λ, it remains similar for all the bands in Fig. 4.13, but becomes $\approx 30\%$ larger altogether when dealing with the time evolution data. This is naively attributed to the fact that the value of initial N_N in the two time evolution data sets are smaller by $\approx 25\%$ compared to the imbalance ones. This dependence is not seen in the post selection analysis where the relative change in N_N is a maximum of $\approx 15\%$. Moreover, the spatial dynamics described in section 3.2 are known to reduce with decreasing N_N, which could have had a positive effect on the extent of overlap between the two clouds. The strength of λ is purely decided by the scattering length a_{scc}, and the overlap integral X^{SCC} given in equation (2.54). As a_{scc} stays fixed under the given experimental conditions and magnetic field, the only quantity that's affected by a changing N_N is the spatial mode of the sodium cloud and hence the overlap integral.

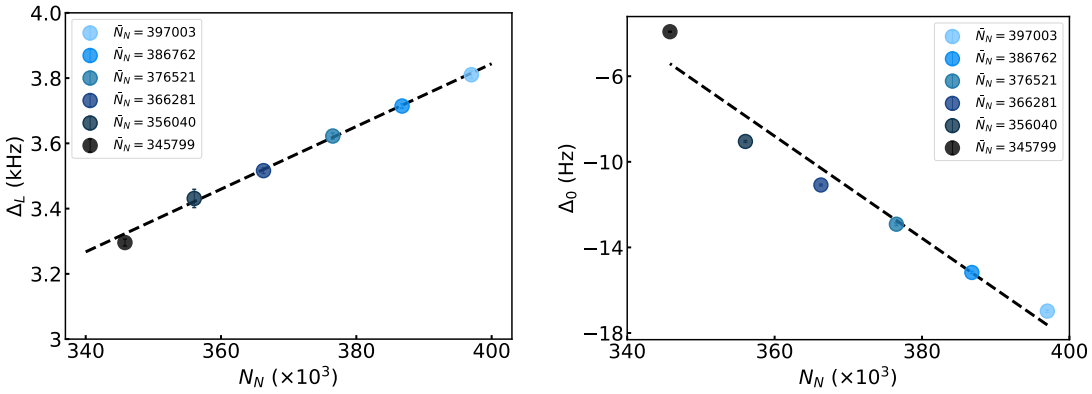

(a) Δ_L **as a function of** N_N **(b)** Δ_0 **as a function of** N_N

Figure 4.14: Values of the components of Δ resulting from the fits shown in Fig. 4.13 as per method II. The data points in both plots correspond to the results of mean field fits to different bands. They range from highest N_N (light blue circles) to lowest (black circles) in decreasing order. The error bar on each point is the uncertainty in the fit. **(a)** change of Δ_L with respect to N_N. The black dashed line represents a linear fit whose slope determines the scaling with N_N. A higher N_N results in a higher value Δ_L. **(b)** changes in Δ_0 with respect to N_N. The dependencies are summarized in table 4.2.

4.2.4 Fluctuations of a coherent spin state

The superposition quench described in section 3.2.1 creates a coherent spin state (CSS) in sodium. Fluctuations that occur in such a state can have two origins: i) quantum fluctuations, i.e., the noise originating from the quantum uncertainty associated with a coherent state, ii)

technical fluctuations resulting from the fluctuating parameters of the MW pulse used to create the superposition. In this section, these two cases are discussed and the extent of their contribution to the experimentally observed fluctuations in sodium are investigated. Hence, this method explores yet another source of noise with regards to the fluctuations seen in lithium.

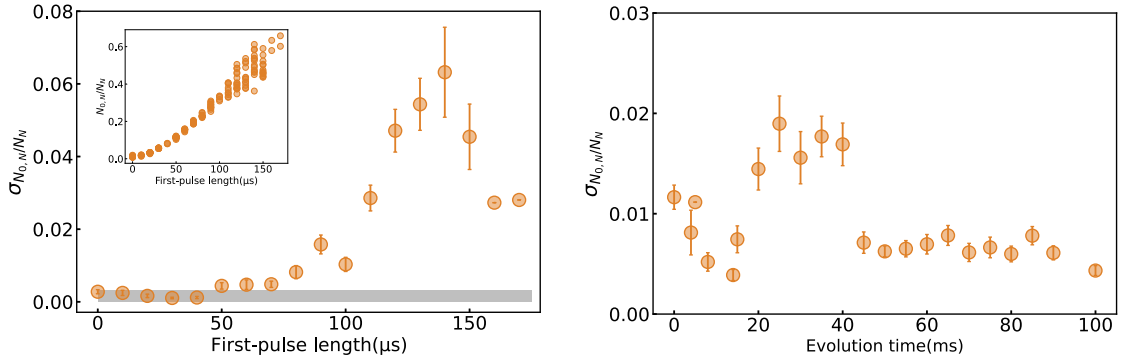

(a) Fluctuations in imbalance fringe of sodium for $|1,1\rangle \rightarrow |1,0\rangle$

(b) Fluctuations in time evolution data set I, $\eta_0 = 0.407$

Figure 4.15: Experimentally observed fluctuations in sodium CSS. (a) scanning the length of the first pulse results in a Rabi like fringe in sodium (see inset). Repeated shots taken at a fixed parameter values of the pulse do not result in the same transfer ratio. The std corresponds to more than 6% of transfer ratio. The grey area represents an approximate level of detection noise. **(b)** similar behaviour is present in the time evolution data set I.

Quantum projection noise

Quantum projection noise (QPN) arises from the inherent nature of indeterminacy of quantum mechanics. Consider a two level system composed of two states $|A\rangle$ and $|B\rangle$ prepared in a state of superposition $\psi = c_A |A\rangle + c_B |B\rangle$, with $|c_A|^2$ and $|c_B|^2$ being the probabilities of finding the system in $|A\rangle$ and $|B\rangle$ respectively. When subjected to measurement, the resulting eigenstate is either $|A\rangle$ or $|B\rangle$. As long as c_A and c_B are not zero, the outcome of this measurement cannot be predicted with certainty. The state vector $|\psi\rangle$ gets projected onto one of the states randomly, regardless of how accurately the state is prepared and measured. Hence, this constitutes a source of noise that's purely due to the quantum nature of the state. In the case of a pseudo-spin system, i.e., an ensemble of N independent two-level atoms as explained in section 2.5.3, QPN translates into characteristic fluctuations in the measured populations of two states[140]. The individual probabilities of the atoms to be in a given state can be combined according to a binomial distribution. Considering the two levels in sodium, the probability of measuring $N_{0,N}$ particles in state $m_F = 0$ is given by,

$$P(N_{0,N}; N_N, p) = \frac{N_N!}{N_{0,N}!\,(N_N - N_{0,N})!} p^{N_{0,N}} (1-p)^{(N_N - N_{0,N})} \tag{4.7}$$

where p is the individual probability of an atom to be in $m_F = 0$ and $(1-p)$ is that of an atom to be in $m_F = 1$. The variance of this distribution is then given by,

$$\sigma^2 = p(1-p)N_N \tag{4.8}$$

The variance is zero when $p = 0$ or $p = 1$, and is maximum when $p = 1/2$, i.e. when the states are equally populated.

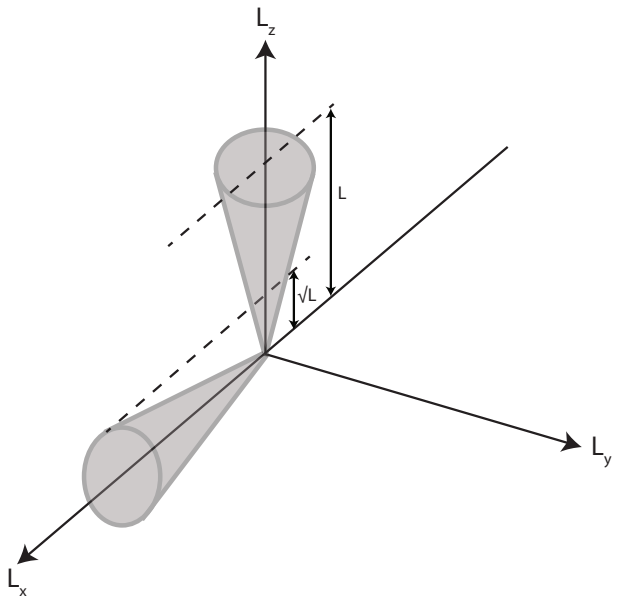

Figure 4.16: Visualization of the projection noise in a CSS. The cone represents a set of state vectors that comprise a collective spin vector L. The uncertainty in its third L_z component corresponds to the quantum uncertainty. It is zero when the cone is along L_z, and maximum when it is orthogonal (see text).

For example, a collective state vector $|L = N/2, \theta = 0\rangle$ can be represented by a set of vectors of length $\sqrt{L(L+1)}$ with their L_z component equal to L. It is visualized in the form of a cone with a radius $\sqrt{L}$. The uncertainty is then represented by the spread in the third component, in this case L_z, for the points on the circle on the base of the cone. The uncertainty is this case zero, i.e. all the points on the base have the same value of L_z. On the hand, it hits its maximum value for a state vector $|L = N/2, \theta = \pi/2, \phi = 0\rangle$. The standard deviation of L_z is then $\sqrt{R/2} \approx \sqrt{N}/2$.

The level of QPN in sodium was approximately estimated using the mathematical definitions outlined in equations (4.7) and (4.8). Recalling from section 3.2.1, the initial superposition of $|1, 1\rangle$ and $|1, 0\rangle$ is achieved by the two-pulse sequence. Scanning the duration of first pulse essentially leads to Rabi oscillations between these two levels. These oscillations were used to estimate QPN in the following manner: A Rabi curve was fitted to the superposition ratio to determine the probabilities p of sodium atoms being in $m_F = 0$. A binomial distribution was created using these values of probabilities, with the number of samples being the number of shots taken at a given pulse length. The std of this distribution, normalized by the total number of atoms was approximated to be QPN, as per the equation (4.8). The resulting estimation is compared to the experimentally observed fluctuations, see Fig. 4.17b. Data at shorter pulse lengths ($\approx$ 50µs) are unreliable as they are buried in the detection noise. For longer pulses, the estimated projection noise is multiplied by a factor of 20 (see inset of Fig. 4.17) to show the order of magnitude by which the experimentally observed fluctuations exceed QPN. They increase with increasing duration of the pulse, which strongly suggests that these fluctuations are due to technical instabilities. As the MW setup used for the quench is quite optimized against imperfections in frequency, duration, and power of the two pulses, most of the fluctuations are attributed to the drifts in the offset magnetic field. Recalling from section 3.2.4, this was the reason behind binning the lithium data according to the sodium data in all the

imbalance data sets.

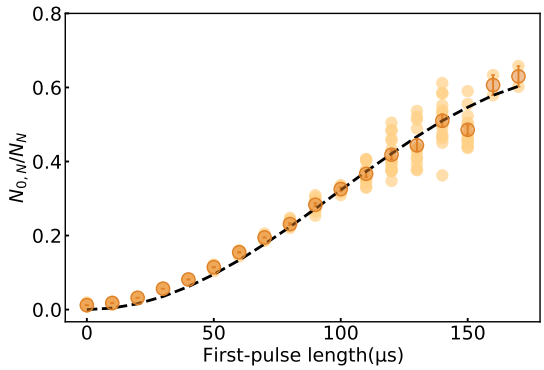

(a) Fitting half a Rabi cycle to $|1,1\rangle \rightarrow |1,0\rangle$ fringe in sodium.

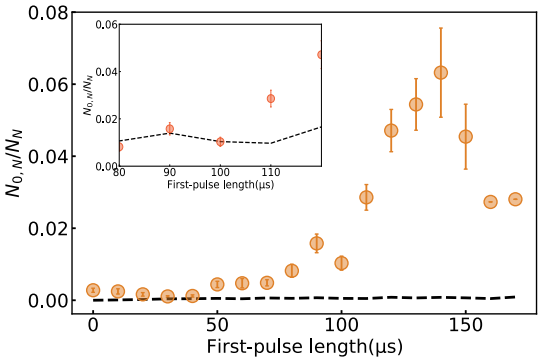

(b) Corresponding fluctuations compared to the estimated QPN.

Figure 4.17: Estimation of projection noise in sodium. **(a)** sodium imbalance plotted as a function of duration of the first pulse. The fringe corresponds to the imbalance data I shown in Fig. **??**. A two-level Rabi formula results in a sinusoidal fit (black dashed) whose values correspond to probabilities (see text). **(b)** a binomial distribution is created with these p values, whose normalized std gives an estimation of projection noise (black dashed). In the inset, the same is multiplied by a factor of 20 to highlight the order of magnitude difference relative to the regime in which the experiment operates.

4.3 Fluctuations: theory

The analysis presented in section 4.2 quantitatively differentiates between the possible sources of noise by investigating only the experimentally available inputs. It describes how the parameters change with respect to the changes in the initial atom numbers. However, a faithful representation of the system can only be produced if such fluctuating conditions are taken into account in the microscopic picture. Doing so on the level of classical GPE is not feasible since its mean field approach does not take into account the dynamical properties of the system. Hence, the approach used in section 4.1 needs to be modified. Moreover, the condensates are always at a finite temperature because of the thermal fraction of atoms, which could interact with the the internal spin degrees of freedom. With this interpretation, comes yet another source of noise, thermal fluctuations. In this section, all these aspects are investigated. It is organized as follows:

1. Section 4.3.1: *Truncated Wigner Approximation.* This part describes the theoretical approach to include the fluctuations in spin lengths (initial N_N and N_L) and in the spin projection (QPN) in the initial conditions. The results of the numerical simulations are compared with the data.

2. Section 4.3.2: *Long time predictions of TWA.* In any dynamical system, its behavior after evolving for a long time may suggest some kind of relaxation. This was studied in the SCC data using the TWA where the evolution time was changed from 30 ms to 600 ms.

3. Section 4.3.3: *Addition of stochastic noise.* This is motivated by the fact that the condensates have finite temperature because of their thermal fraction. In other words, spin degrees of freedom coexist with the atoms in the thermal wings. These noise sources

are once again incorporated into the TWA and it is closely compared with the rest of the sources of fluctuations mentioned above.

While the comparison between theory and data is carried out for all the existing data, the discussions in the main text concentrate on three data sets, **time evolution data I**, **time evolution data II** and **imbalance data I**. The rest of the comparisons are displayed in appendix A.

4.3.1 Truncated-Wigner approximation

TWA is a stochastic technique which provides a phase-space description of a given quantum system[141]. It is widely used to treat problems that lie beyond the capabilities of standard mean field GPE, i.e., for systems which possess incoherences and quantum fluctuations. In those cases, it becomes laborious to calculate the full evolution of the system Hamiltonian, and hence, higher order terms are neglected, leading to *truncation*. The main idea of this method is to have an entire distribution of initial states, represented by Wigner function[142]. This technique is valid over a large regime of dilute degenerate gases where the Wigner function is Gaussian and hence positive[143]. Consequently, it is then considered as a classical probability distribution. Each time evolution of the system begins with an initial condition sampled from it, thus bringing in fluctuations only in the initial states. Hence, this method is also known as semi-classical[144, 145]. The final expectation value of the desired observable at the end of the evolution is then given by averaging the values of the observables over the distribution of all individual trajectories.

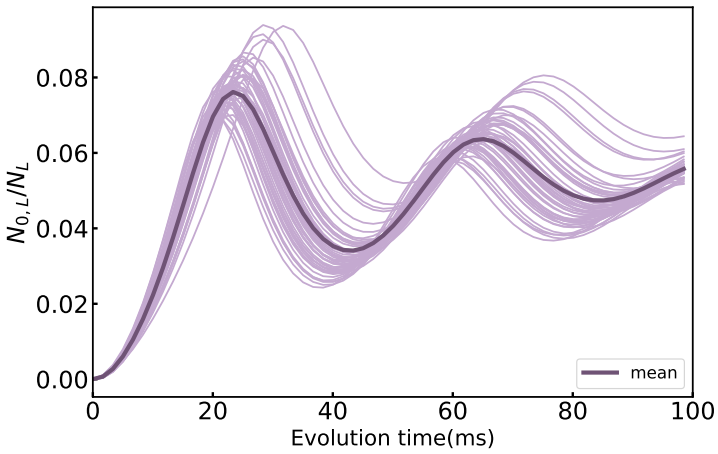

Figure 4.18: Visualization of the TWA evolution. Time evolution of $^{23}\mathrm{Na} - {}^{7}\mathrm{Li}$ mixture under specified experimental parameters was simulated. The spin transfer ratio is displayed for all 50 individual realizations evolved with 50 different initial states. The nature of the initial state fluctuations were motivated by the experimental data. The final state is averaged over all the realizations, resulting in a mean and an std.

Numerical simulation of the TWA provides the first insights of the dynamics of a system in the presence of noise, regardless of whether the fluctuations are technical or quantum in origin. A typical TWA simulation is displayed in Fig. 4.18 to visualize its underlying mechanism of including the fluctuations. 50 realizations were performed to simulate the time evolution of the spin components of both species at a fixed imbalance in sodium. The initial state was distributed according to atom number fluctuations seen in time evolution data set I. Individual

runs with different initial states evolve differently from each other, hence resulting in a final state characterized by a mean and an std. Note that this figure is intended only as an example to describe the principle behind TWA, and the actual comparison with the data is shown later in the text.
It was demonstrated in section 4.2.2, Fig. 4.7a, that the predictions of the mean field method do not agree with the data when spin length of sodium is altered, while keeping fixed model parameters. Having fixed the dependence of Δ on N_N, different simulations were performed selectively by switching on and off the noise sources, thus exploring the extent of each contribution:

- The simulation was written such that it could accommodate fluctuations both in spin length, i.e., initial atom numbers and spin projection of both species. The two noises were controlled independently, and could be switched on and off selectively, to inspect which kind of noise is dominating.
- In the case of spin length fluctuations, the initial state distribution was characterized by the experimentally observed fluctuations in the atom numbers of the condensates (see section 4.2.3).
- In the case of spin projection, which is the noise in L_z component of the spins, two different sources were discussed (see section 4.2.4). First one was the technical noise present in superposition ratio of sodium. Including it in the TWA was futile because its magnitude with which the simulation would produce reliable results had to be less than the detection noise in sodium. Hence, this was discarded and only the second kind, which is the quantum uncertainty of coherent state, QPN was considered. The initial states are then distributed around the mean spin direction with a spread equal to $\sqrt{N}/2$.
- All the spin components were evolved and averaged over 200 realizations, followed by the calculation of the mean and std of $N_{0,L}/N_L$. During each realization, the parameter Δ was appropriately updated, owing to its dependence on N_N discussed in section 4.2.3, equation (4.6).

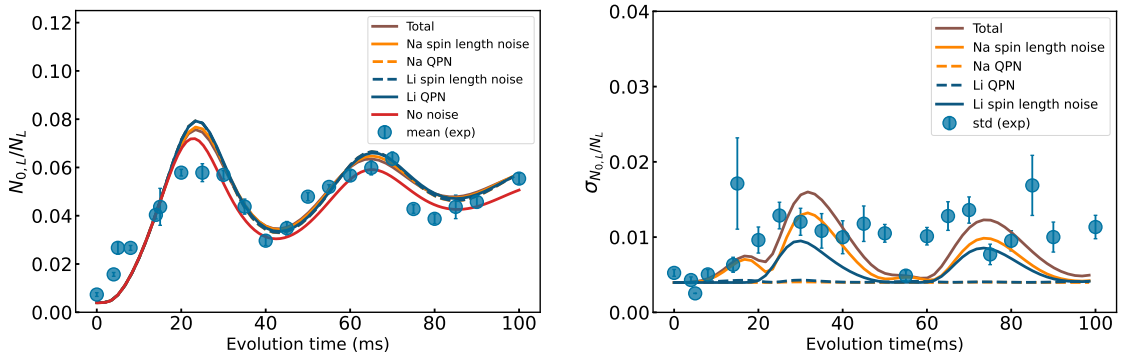

(a) TWA predictions for mean $N_{0,L}/N_L$.

(b) TWA predictions for std of $N_{0,L}/N_L$.

Figure 4.19: Comparing the time evolution data set I (η_0=0.4) with the predictions of TWA. Spin length and projection fluctuations in the spins of both species are incorporated as initial state fluctuations by means of TWA. Four different numerical simulations of TWA are displayed, each time with only one source of noise. **(a)** predictions of mean lithium spin transfer. All the curves qualitatively match the original curve with no noise (see legends). **(b)** corresponding stds. It can be seen that most of the fluctuations come from the fluctuation of initial spin length in sodium.

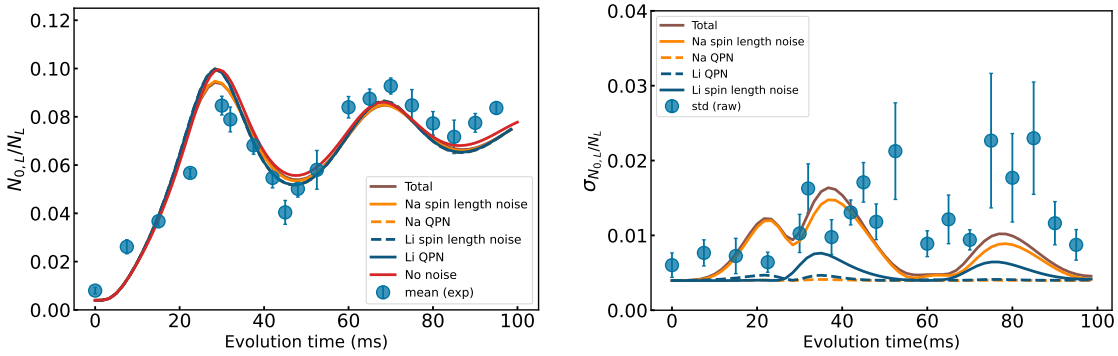

(a) TWA predictions for mean $N_{0,L}/N_L$.

(b) TWA predictions for std of $N_{0,L}/N_L$.

Figure 4.20: Comparing the time evolution data set II (η_0=0.293) with the prediction of TWA. The simulation method is followed exactly like in Fig. 4.19b. **(a)** predictions of mean lithium spin transfer. **(b)** corresponding stds. The extent of agreement between the theory and data is the same as that 0f Fig. 4.19. Once again, the maximum amount of fluctuations arises from the fluctuations in the initial N_N.

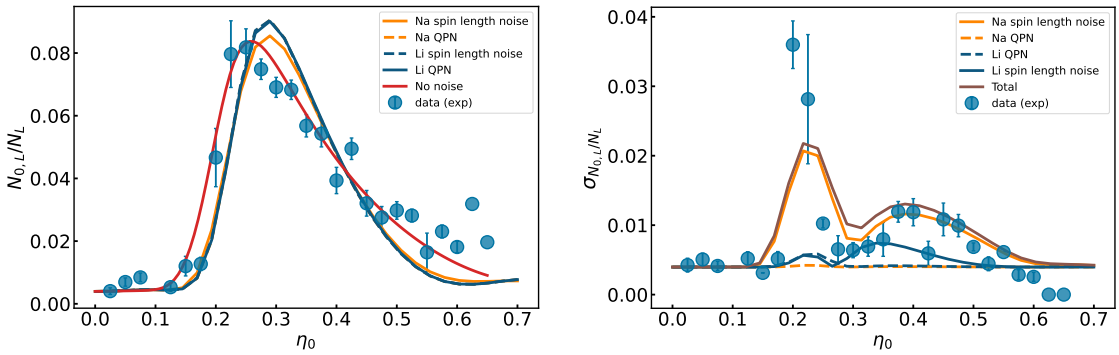

(a) TWA predictions for mean $N_{0,L}/N_L$.

(b) TWA predictions for std of $N_{0,L}/N_L$.

Figure 4.21: Comparing the imbalance data set I with the predictions of TWA. The fluctuations of different kind are included in the initial state fluctuations, same as it was done in Fig. 4.19.**(a)** the qualitative resonance behavior is reproduced by the TWA, but the presence of noise shifts the flank position at $\eta_0 = 0.2$ as well as the slope towards higher η_0s compared to the original(see legends). **(b)** the prediction of std show that fluctuations in N_N that contribute the most.

Examining the TWA results for the two time evolution data sets and the imbalance data set I, the following conclusions are drawn:

- **Time evolution data**: Fig. 4.19 and Fig. 4.20 show that the mean is effectively restored even in the presence of initial state noise, and it agrees quite well with the original prediction of the mean field, i.e., with fixed atom numbers and no noise. The fluctuations calculated over multiple realizations show that the major part of the total observed fluctuations indeed come from sodium spin length fluctuation. The overall initial rising behavior is captured well and the overall amplitude is in the right order of magnitude as well. In data set II (Fig. 4.20), they are somewhat underestimated 40 ms on wards.

- **Imbalance data I**: Fig. 4.21a shows that the shape of the resonance qualitatively well captured. However, the flank at $\eta_0 = 0.2$ is slightly smoothed out as opposed to the data,

and is also shifted in position. The tail at larger η_0 also features a different slope, thus indicating that the dynamics at 30 ms is still oscillatory. As per fluctuations, the TWA results in an unmistakable prediction by capturing the shape of std almost perfectly. What's still lacking however, is its amplitude at $\eta_0 = 0.2$.

Overall, the predictions of TWA possess a good qualitative agreement with the data without doubt. As mentioned above, there exist clear deviations which are yet to be accounted for.

4.3.2 Late time dynamics

In this case, the evolution time of the TWA routine was set to 600 ms, much longer compared to 30 ms where the imbalance measurements were performed.

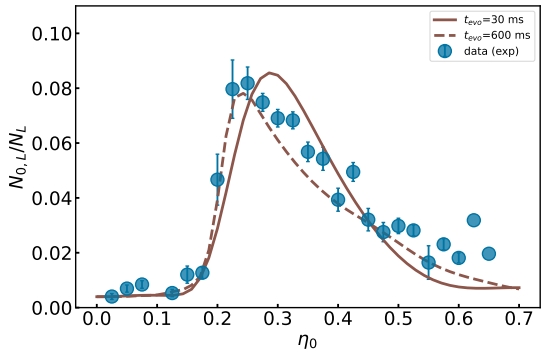

(a) TWA predictions for mean $N_{0,L}/N_L$ at $t = 30$ ms and 600 ms.

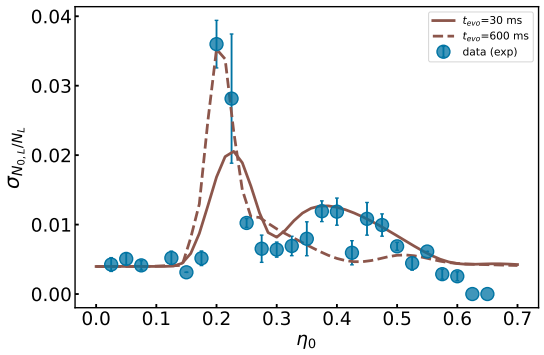

(b) TWA predictions for std of $N_{0,L}/N_L$ at $t = 30$ ms and 600 ms.

Figure 4.22: Comparing the late time result of TWA with the imbalance data I. In addition to simulation performed at t=30 ms, as shown in Fig. 4.21,late time results are plotted. Note that the data itself was taken at 30 ms. **(a)** predictions of the mean. The late time dynamics agrees quite well with the data, better than at 30 ms. **(b)** corresponding std. The level of fluctuations at the flank is in perfect agreement with the late time result in terms of the initial rise and amplitude.

Surprisingly, the agreement between the late time result of TWA and the resonance shape is exceedingly better than that with 30 ms, see Fig. 4.22a. The interactions still seem to be resulting in oscillations around the slope of the resonance at 30 ms. However, the predictions at a later time match the slope quite well and are quite robust to further increase in the duration of evolution time. Another distinct result is that fluctuations at 600 ms are considerably larger, and aptly match the data.

4.3.3 Stochastic noise

The late time characteristics of the mixture dynamics discussed in section 4.3.2 promptly encouraged further investigation of related phenomena, such as relaxations and the possibility of the system attaining thermal equilibrium. A system surrounded by a thermal reservoir can be vaguely thought of as an open quantum system. In fact, it is considered as a subsystem of the combined system, where it can exchange energy with its surrounding reservoir[146]. In such situations, the subsystem is known to change due to its interaction with the environment, resulting in decoherence and dissipation effects. This description was applied in the case of $^{23}\mathrm{Na} - {}^{7}\mathrm{Li}$ mixture, where the concept of the reservoir was attributed to the thermal degrees

of freedom of the large sodium cloud and the subsystem was attributed to the spin degrees of freedom. The latter are nothing but the four internal states of sodium and lithium, with which the gauge invariant dynamics was engineered. Furthermore, as the reservoir has a finite temperature, the presence of classical thermal fluctuations were considered. These effects were then incorporated in TWA, where the thermal fluctuations were added in the form of a multiplicative noise term to the equations of motion.

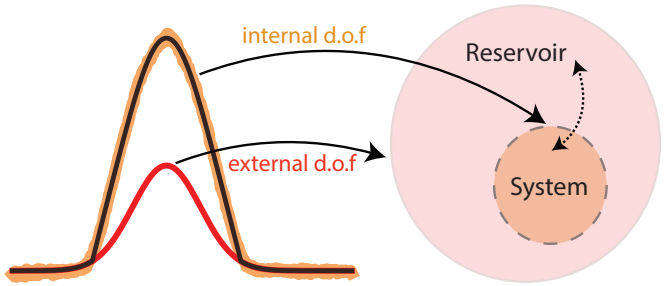

Figure 4.23: Visualization of system-reservoir coupling. This description is motivated by the the fact that the condensates possess thermal wings at finite temperature and the same is attributed to the concept of reservoir. The internal states with which the SCC was observed is considered as a subsystem.

For a statistical evolution, this means that this noise is randomly assigned at every time step of the simulation on top of the coherent evolution,

$$\partial_t L_x = (\partial_t L_x)_{coh} + \xi(t) L_y \tag{4.9}$$
$$\partial_t L_y = (\partial_t L_y)_{coh} - \xi(t) L_x \tag{4.10}$$
$$\partial_t L_z = (\partial_t L_z)_{coh}, \tag{4.11}$$

where ξ is a Gaussian noise with $\langle \xi(t) \rangle$ and $\langle \xi(t)\xi(t') \rangle = \tilde{\gamma}\delta(t-t')$. Here, $\tilde{\gamma}$ is the noise strength and $(...)_{coh}$ refers to the coherent evolution of the system. As these noise terms are added in L_x and L_y components of both species, they can be thought of as random fluctuations in the phase plane. Moreover, it was added under the assumption that the correlation times at which the reservoir affects the system are very close to each other. It is quite important to make a distinction between $\tilde{\gamma}$ that signifies the fluctuations in time and the phenomenological damping term γ that is already present in the x-y (see section 4.1). The open quantum system picture as outlined in [146], consists of both damping and the stochastic noise, which behave in a counteracting manner.
TWA simulations were repeated with the stochastic noise terms of different strengths, see Fig. 4.24. The simulations indeed showed that both stochastic noise $\tilde{\gamma}$ and the damping γ are rather effective terms and that it is necessary to include both, in order to account for two different effects; an overall damping at late times, and the random fluctuations. The best agreement that was obtained entailed an interplay between their values. In all the simulations with stochastic noise, γ was fixed at 70% of its original value of 3.9 Hz, while the level of stochastic noise was varied. The effect of adding stochastic noise is predominantly seen in the time evolution data, see Fig. 4.24b and Fig. 4.25b. A noise level of $\tilde{\gamma}/2\pi$=0.101 Hz agrees well with the level of fluctuations at all times. Increasing it to 0.358 Hz already leads to a slight overestimation in the std and leads to undesired changes in the means as well.

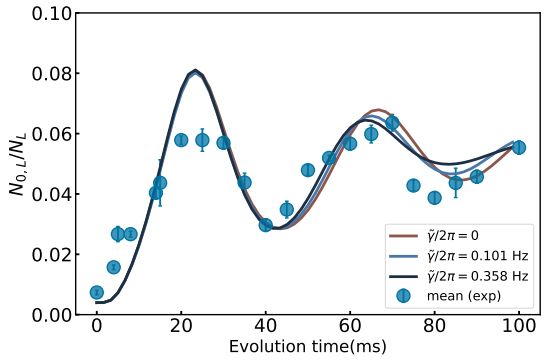

(a) Predictions of TWA with stochastic noise for mean $N_{0,L}/N_L$.

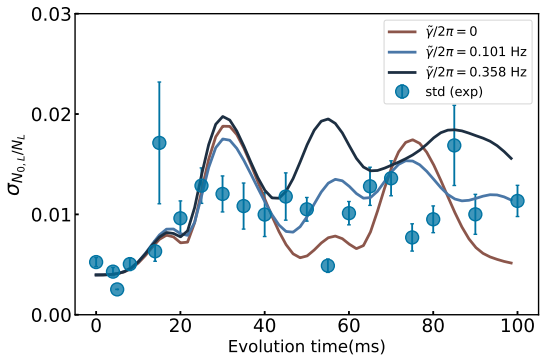

(b) Predictions of TWA with stochastic noise for fluctuations $N_{0,L}/N_L$.

Figure 4.24: Comparison of various strengths of stochastic noise with time evolution data set I. The stochastic noise terms are added to the equations of motions, which are evolved using TWA. The values of damping γ is reduced to 70% of its original value (see text), to effectively counteract the stochastic part. **(a)** means reproduced with different strengths of $\tilde{\gamma}/2\pi$=0.101 Hz (light blue), 0.358 Hz (black). **(b)** the effect on the std is improved and its consistent rise after t=40 ms is noticeable, unlike the case where $\tilde{\gamma} = 0$.

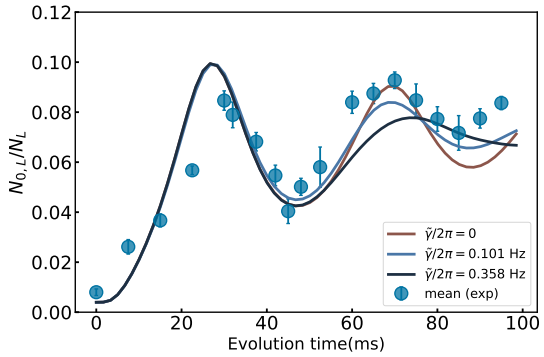

(a) Predictions of TWA with stochastic noise for mean $N_{0,L}/N_L$.

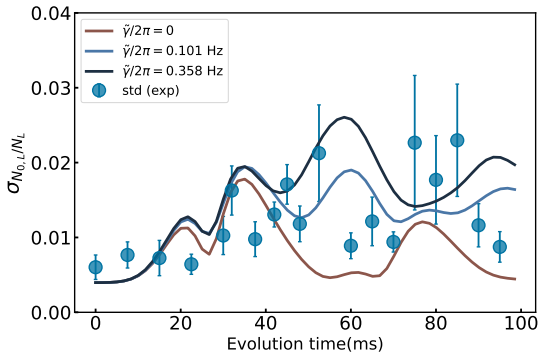

(b) Predictions of TWA with stochastic noise for fluctuations $N_{0,L}/N_L$.

Figure 4.25: Comparing various strengths of stochastic noise with time evolution data set II. The theoretical treatment is the same as that of Fig. 4.24. **(a)** means reproduced with different strengths of $\tilde{\gamma}/2\pi$=0.101 Hz (light blue), 0.358 Hz (black). **(b)** the prediction on std is much more pronounced after t=40 ms similar to Fig. 4.24b.

Similar treatment was repeated for the imbalance data set I. In this case, both early and late time simulations exhibit only minute changes in the mean $N_{0,L}/N_L$, in the presence of stochastic noise, see Fig. 4.26a. On the other hand, the results regarding fluctuations are slightly more noticeable, because all of them show an increase with increasing stochastic noise, see Fig. 4.26b. Moreover, at higher values of η_0, the early and the late time curves seem to oscillate.

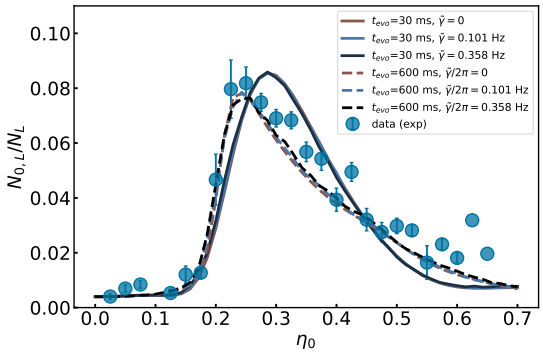

(a) Predictions of TWA with stochastic noise for mean $N_{0,L}/N_L$.

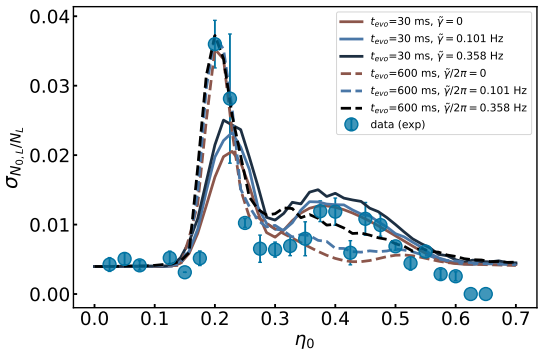

(b) Predictions of TWA with stochastic noise for fluctuations $N_{0,L}/N_L$.

Figure 4.26: Comparing the results of TWA with stochastic noise with imbalance data set I. (a) means reproduced with $\tilde{\gamma}/2\pi$=0.101 Hz (light blue), 0.358 Hz (black). **(b)** corresponding stds. The changes are are slightly more apparent, where the predicted level of fluctuations rises with increasing stochastic noise.

It was observed that $\tilde{\gamma}$ and γ could not be used independently to describe the damping seen in the mean $N_{0,L}/N_L$, as well its fluctuations. The effect was particularly strong in the time evolution data. Increasing γ led to an underestimation of the fluctuations, whereas decreasing it resulted in oscillations that were mostly undamped and hence did not capture the experimental data. The imbalance data, however, was relatively less sensitive. A further investigation is yet to be carried out, to disclose their role in describing the dynamics of the system. Moreover, the stochastic noise is closely associated with the question as to whether the data resembles a thermal like steady state at long times.

4.4 Summary

- The first part of this chapter introduced the mean field approach that was adapted in [1] to describe the SCC data. The equations of motions for the spin components of both species were numerically solved and the best matching predictions were used to deduce the values of parameters χ, Δ and λ that constitute the spin Hamiltonian. The model was able to successfully reproduce the behavior of the data. A phenomenological damping term was added, primarily to account for the decoherence effects, that resulted in reduced oscillation strength in the time evolution data.

- The raw data clearly showed that the spin transfer ratio in lithium $N_{0,L}/N_L$ exhibits fluctuations and that their level, especially in the case of imbalance data is quite striking. To this end, a post selection analysis was performed to investigate the nature and cause of these fluctuations. This analysis revealed that the parameters Δ_0 and Δ_L depend linearly on sodium atom number N_N. Furthermore, λ was also observed to increase with decreasing N_N and vice versa. This was attributed to the change in spatial overlap of the two clouds. However, these relations were not exclusively seen in the post selection analysis.

- These dependencies were then incorporated theoretically, by means of TWA. Being a semi-classical method, it accommodated the fluctuations as initial state noise. More than 200 numerical realizations were executed, each with a slightly different initial state than before. To this end, the first simulations were performed by taking two sources of fluctuations into account namely spin length and spin projection, and their contributions were independently monitored. For spin length, the initial state distributions were characterized by the experimentally observed fluctuation in the initial atom numbers. On the other hand, projection noise was attributed to the quantum uncertainty of the CSS in sodium. It was clearly seen that fluctuations seen in the spin transfer of lithium are largely due to spin length fluctuation in sodium. If such technical fluctuations are reduced considerably, one shall be able to observe QPN, which itself is paramount in the context of quantum fluctuations.

- Additionally, TWA was utilized to probe two more aspects, the long time dynamics and the effect of thermal fluctuations. The late time simulation inspected how the system would look if it were allowed to interact for a very long time. It was observed that the late time results agree significantly better with the data than the early time result. The robustness that followed the late time predictions hinted towards the presence of a steady state. In close contexts, thermal aspects were introduced based on the description of a system-reservoir coupling. The associated fluctuations were incorporated into the equations of motion in the x-y plane in the form of random stochastic phase noise. Their presence indeed changed the outcome of TWA, however by small amounts. There are several open questions with respect to the interpretation of the results. For instance, when initial state is allowed to fluctuate, the result of simulation at 30 ms exhibits slight, but clear deviations with respect to the imbalance data. Furthermore, TWA predicts the rise of fluctuations to match the data only at a later time. Hence, a complete description of the actual physical dynamics that happens in the atomic mixture is yet to be understood. Moreover, the physical meaning of the magnitude of the stochastic noise $\tilde{\gamma}$ is unclear. It remains to be seen whether the system will resemble a thermal like state in the long time limit, characterized by a temperature. The stochastic noise $\tilde{\gamma}$ in combination with the phenomenological damping term γ might play a crucial role in this regard.

Chapter 5

Conclusion and outlook

Experimental realization of a building block of U(1) LGT

The experiment aimed towards the quantum simulation of U(1) LGT, also called the lattice Schwinger model, using ultracold $^{23}\mathrm{Na} - {}^{7}\mathrm{Li}$ mixture. It essentially describes QED in one dimension, which deals with the coupling of matter and the gauge field. Hence, the experimental platform consisted of two species, whose internal states $|1,1\rangle$ and $|1,0\rangle$ were utilized to realize two main ingredients of the theory: matter (lithium) and gauge field (sodium). This mixture of spinor gases was achieved by creating BECs of the two species in a final optical trap, in their respective internal state of $|1,1\rangle$. The practical implementation of HEP formulation of U(1) LGT requires it to be rewritten in the language of spins using QLM, where the gauge field is mapped onto $\hat{L}_{z,N}$ of sodium spin, and the links connecting the lattice sites are mapped onto its raising and lowering operators $\hat{L}_{+,N}$ and $\hat{L}_{-,N}$. Moreover, QLM realizes Gauss' law in the form of an interspecies SCC resonance. Hence, the physical implementation relied on several controlled operations such as magnetic field control, manipulation of the internal spin states of the two species and their faithful detection. These aspects were realized using techniques such as two-pulse sequence and SG imaging. The two-pulse sequence enabled the creation of a tunable gauge field term $\hat{L}_{z,N}$ by quenching the sodium states into desired superpositions. Imaging with SG pulses led to the determination of population in individual spin states. Moreover, the energy offset between the states could be varied by applying a different magnetic field. Thus, this QS realized a highly tunable setup, allowing one to explore the spin dynamics in different parameter regimes.

A series of controlled steps were followed to perform the measurements of SCC. Immediately after creating both condensates in their respective $|1,1\rangle$ states, a population imbalance was created in sodium to engineer the gauge field term. Meanwhile all the lithium atoms stayed in $|1,1\rangle$, thus representing a fully filled bosonic vacuum state. The two species were then evolved, during which they underwent contact collisions resulting in SCC. About 6-8$\%$ of the total lithium atoms were transferred from $|1,1\rangle$ to $|1,0\rangle$. To this end, three different kinds of measurements were performed, spanning a wide range of parameters. First one was the time evolution measurement, where the interaction time was varied, keeping the $\hat{L}_{z,N}$ fixed. Second kind was called the imbalance measurement where the interaction time was fixed at 30 ms, but the value of the gauge field was scanned. In the final sets of measurements, the absolute magnetic field was varied in steps 50 mG, and the gauge field was scanned again, all evolving for 30 ms. All the data was comprehensively explained using an effective spin

Hamiltonian based on mean field description.

Fluctuations

All these experimental efforts and its first results served as foundations for the extended research and analysis presented in this thesis. Fluctuations that were observed in the lithium spin transfer ratio in the raw data were not a part of mean field description earlier. Moreover, the predictions of mean field theory changed drastically with changing atom numbers. Besides, the initial atom numbers in the condensates of both species were not constant from shot to shot, thus leading to a fluctuation in total spin length in every experimental shot. To this end, a post selection analysis of the raw data was carried out, which revealed that the parameters λ and Δ that constitute the Hamiltonian, indeed depend on the atom number of sodium. Furthermore, owing to the fact that a coherent spin state is created in sodium upon superposition quench, its quantum uncertainty, i.e., QPN was considered. Having quantified the orders of magnitude of these different possible contributions, they were effectively included in theoretical treatments, using the formalism of TWA. Being a classical-statistical approach, the TWA probed the interspecies dynamics by sampling over a distribution of initial conditions. On averaging over multiple realizations, it was observed that the major contribution of the fluctuation in the spin transfer in lithium comes from an initial spin length noise in sodium. These analyses were crucial in assessing the stability of the setup. They also showed that the projection noise is relatively small, which in itself constitutes a subject of interest. It remains a future task to improve the setup and reduce the technical fluctuations so that the quantum fluctuations can be observed.

There were instances, where the results of the TWA did not explain the data sufficiently, indicating that there are several aspects that are not yet understood. The theory was subjected to further scrutiny, where the TWA was utilized to investigate two more aspects, namely, the long time dynamics and thermal fluctuations. In the long time simulation, the evolution time of the spins was set to 600 ms. Surprisingly, not only its predictions bore an almost perfect resemblance to the resonance shape in the imbalance data I, but also accounted for the dramatic increase of fluctuations at the flank. While its interpretation still needs progress, it hints towards possible physical processes that are fast enough to drive the system to resemble a steady state already at 30 ms. In close contexts, the aspect of thermal fluctuations was introduced, motivated by the fact that the atoms in condensed state co-exist with those still in the thermal state. Therefore, a system-reservoir like description was adapted, guided by classical thermodynamics. The concept of the reservoir was attributed to the thermal degrees of freedom, to which, the internal states undergoing gauge invariant dynamics are coupled. This was introduced in the theory in the form of stochastic noise. Its results albeit primitive, improved the predictions of the simulation, especially in the case of time evolution data. A more intriguing aspect associated with the system-reservoir coupling is the thermal description itself, i.e., it remains to be seen whether the system attains thermal equilibrium at long times. If so, it could be used to determine the temperature of the system. This could further open up opportunities in the study of thermalization aspects of a gauge theory, where the gauge invariant dynamics could possess features of a thermal like steady state without breaking gauge invariance[147].

Processes like atom loss and spatial dynamics seen in sodium were not included in the TWA treatment. By affecting the spatial overlap of the two clouds, these processes lead to

changes in the overlap integrals. Their effects on the dynamics and their roles in the fluctuation of the model parameters themselves are yet to be clarified. From an experimental point of view, strong confinement using an optical lattice is one proposed solution to tackle the spatial deformations. Moreover, to understand how these aspects influence the overlap integrals, they have to be included in the theoretical description, which is an arduous task.

The minimal instance of U(1) LGT presented here is a first step in the direction of building its extended version in a 1D optical lattice. The core concept of a quantum simulator was realized already in the building block, by conceptually bringing together two systems with vastly different energy scales. It was proposed that these different building blocks can be coupled via Raman-assisted tunneling[148]. Moreover, by replacing bosonic species that represented the matter by a fermionic species, it's possible to realize the standard description of QED with fermionic matter and to include the relativistic effect such as Lorentz-invariance[79]. Furthermore, such a mixture platform was proposed for quantum computation and error correction[149], which showcases yet another example of the opportunities associated with ultracold mixtures in optical lattices. Not only these future prospects hold exciting opportunities, but also provide the right foundation to study more complicated systems.

Appendix A

TWA for magnetic field measurements

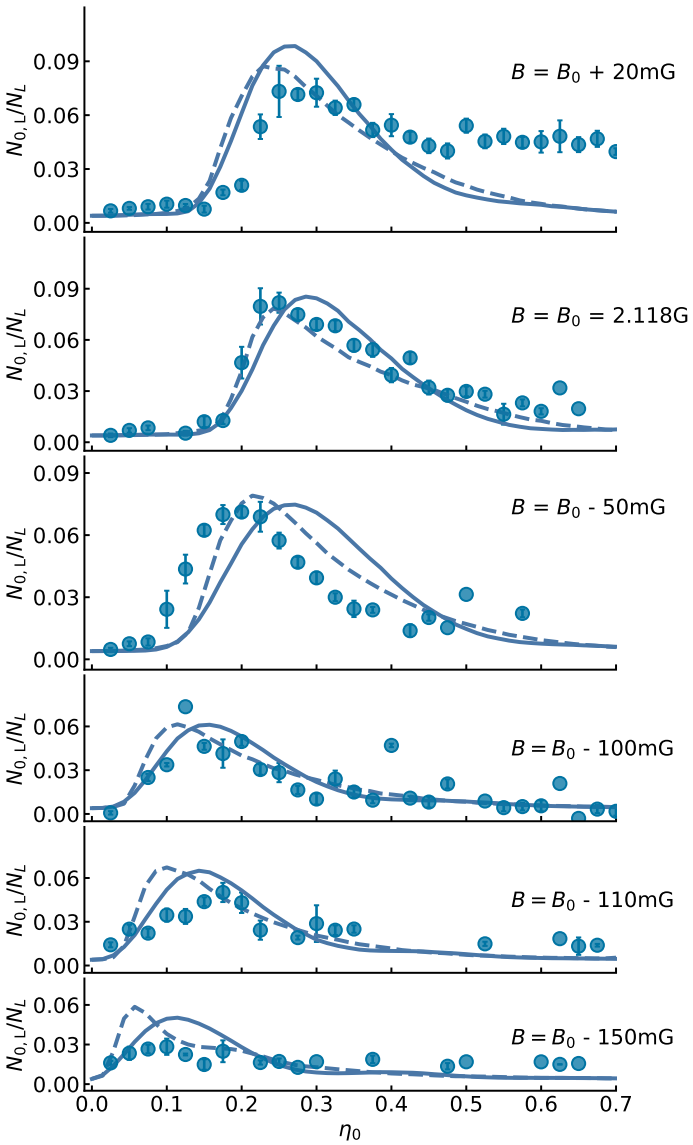

Figure A.1: TWA for imbalance measurements at varying magnetic field. The theoretical predictions for the mean spin transfer in lithium as a function of varying magnetic field are shown. Early time results are displayed in light blue solid lines, and the late time results are represented by the dashed ones.

The predictions of TWA explained in chapter 4 are compared with the rest of the imbalance measurements. The plots in the two figures Fig. A.1 and Fig. A.2 corresponds to the following values of magnetic field: 2.137 G, 2.118 G, 2.068 G, 2.019 G, 2.009 G and 1.968 G (from top to bottom). The initial state fluctuations are added in the form of spin length fluctuations as described in section 4.3.1. The magnitude of the stochastic noise terms is set to $\tilde{\gamma}/2\pi = 0.101$ Hz. The corresponding raw data is displayed in section 3.2.5, chapter 2. The predictions of TWA for the mean and the std are shown in the following figures, where both early (light blue solid) and late time (light blue dashed) results of displayed. There are certain clear deviations in the TWA predictions, especially in the late time simulations of the std for 2.068 G (3^{rd}), 2.019 G (4^{th}) and 2.009 G (5^{th}). As mentioned in the outlook, these data sets await a further interpretation.

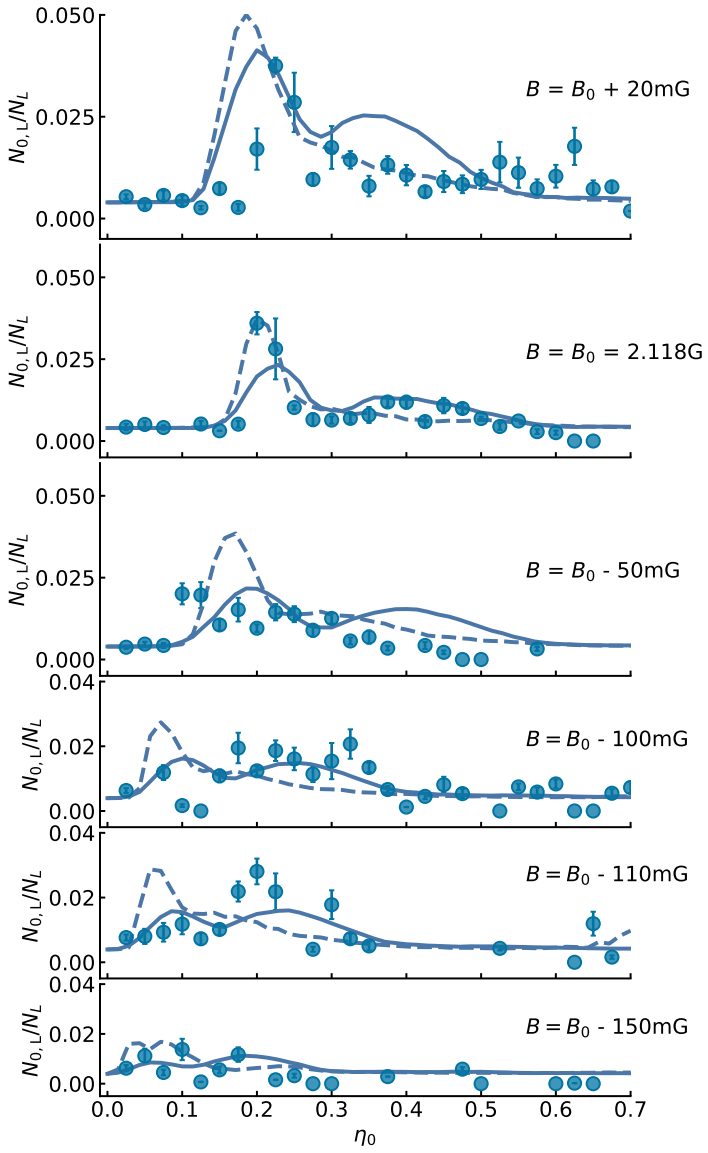

Figure A.2: TWA for the remaining imbalance measurements. The theoretical predictions for the fluctuations $N_{0,L}/N_L$ as a function of varying magnetic field are shown. Early time results are displayed in light blue solid lines, and the late time results are represented by the dashed ones. For some data sets, the late time simulations predict a much higher fluctuations than that of the data (see text).

Appendix B

Experimental sequence

The following python script is called *Experiment.py*, which shows the experimental sequence to carry out a mixture BEC cycle. The commands needed to execute the different stages of the experiment are written in the form of functions in separate scripts, which are imported into the main file. Hardware connections are specified in the beginning of the script, which is identical to the connection table.

```
from labscript import *
from labscript_devices.CiceroOpalKellyXEM3001 import CiceroOpalKellyXEM3001
from labscript_devices.NI_DAQmx.models import NI_PXI_6254
from labscript_devices.NI_DAQmx.models import NI_PXI_6733
from user_devices.MakoCamera.labscript_devices import MakoCamera
from serial import Serial
from user_devices.CustomArduinoDevice.labscript_devices import
    CustomArduinoDevice
from numpy import pi

CiceroOpalKellyXEM3001(name='clock', serial='1711000H46')

NI_PXI_6733(name='Bilbo_card_4', parent_device=clock.clockline,
    clock_terminal='PFI1', MAX_name='PXI1Slot4')
NI_PXI_6733(name='Gollum_card_5', parent_device=clock.clockline,
    clock_terminal='PFI7', MAX_name='PXI1Slot5')
NI_PXI_6733(name='Frodo_card_6', parent_device=clock.clockline,
    clock_terminal='PFI7', MAX_name='PXI1Slot6')
NI_PXI_6254(name='Gandalf_card_2', parent_device=clock.clockline,
    clock_terminal='PFI0', MAX_name='PXI1Slot2')
CustomArduinoDevice('arduino', com_port='COM3')


#CARD 6 (Frodo)  : This is a 6733 card. All the channels out of this card
    are defined below.
#digital channels
DigitalOut(name='D1_1_Na_Big_AOM',parent_device=Frodo_card_6, connection='
    port0/line0')
DigitalOut(name='D1_2_Na_MOT_AOM',parent_device=Frodo_card_6, connection='
    port0/line1')
DigitalOut(name='D1_3_Na_imaging_AOM',parent_device=Frodo_card_6,
    connection='port0/line2')
DigitalOut(name='D1_4_slower_shutter',parent_device=Frodo_card_6,
    connection='port0/line3')
```

```
Shutter(name='D1_5_Na_imaging_shutter',parent_device=Frodo_card_6,
    connection='port0/line4')
Shutter(name='D1_6_Na_repumper_shutter',parent_device=Frodo_card_6,
    connection='port0/line5')
Shutter(name='D1_7_Na_umpump_shutter',parent_device=Frodo_card_6,
    connection='port0/line6')
DigitalOut(name='D1_8_Na_MOT_shutter',parent_device=Frodo_card_6,
    connection='port0/line7')

#Analog channels
AnalogOut(name='A1_1_Na_img_int', parent_device=Frodo_card_6, connection='
    ao0')
AnalogOut(name='A1_2_Li_beat_freq', parent_device=Frodo_card_6, connection=
    'ao1')
AnalogOut(name='A1_3_Li_repump_int_control', parent_device=Frodo_card_6,
    connection='ao2')
AnalogOut(name='A1_4_Li_img_int', parent_device=Frodo_card_6, connection='
    ao3')
AnalogOut(name='A1_5_ODT1_horizontal', parent_device=Frodo_card_6,
    connection='ao4')
AnalogOut(name='A1_6_ODT1_ver', parent_device=Frodo_card_6, connection='ao5
    ')
AnalogOut(name='A1_7_ODT2_hor', parent_device=Frodo_card_6, connection='ao6
    ')
AnalogOut(name='A1_8_ODT2_ver', parent_device=Frodo_card_6, connection='ao7
    ')

#CARD 4 (Bilbo) : This is a 6733 card. All the channels out of this card
    are defined below.
#digital channels

DigitalOut(name='D2_1_Na_repump_AOM',parent_device=Bilbo_card_4,connection=
    'port0/line0')
DigitalOut(name='D2_2_Na_umpump_repump_AOM',parent_device=Bilbo_card_4,
    connection='port0/line1')
DigitalOut(name='D2_3_Na_slower_AOM',parent_device=Bilbo_card_4,connection=
    'port0/line2')
DigitalOut(name='D2_4_Na_umpump_AOM',parent_device=Bilbo_card_4,connection=
    'port0/line3')
DigitalOut(name='D2_5_Antibias_switch',parent_device=Bilbo_card_4,
    connection='port0/line4')
DigitalOut(name='D2_6_Li_MOT_int',parent_device=Bilbo_card_4,connection='
    port0/line5')
DigitalOut(name='D2_7_Schutz_box',parent_device=Bilbo_card_4,connection='
    port0/line6')
DigitalOut(name='D2_8_Li_repump_int',parent_device=Bilbo_card_4,connection=
    'port0/line7')

#anlog channels
AnalogOut(name='A2_1_curvature_power_supply', parent_device=Bilbo_card_4,
    connection='ao0')
AnalogOut(name='A2_2_Gradient_power_supply', parent_device=Bilbo_card_4,
    connection='ao1')
AnalogOut(name='A2_3_bias_power_supply', parent_device=Bilbo_card_4,
    connection='ao2')
```

```
AnalogOut(name='A2_4_finetune_power_supply', parent_device=Bilbo_card_4, connection='ao3')
AnalogOut(name='A2_5_Na_MOT_power', parent_device=Bilbo_card_4, connection='ao4')
AnalogOut(name='A2_6_Offset_Y_fast', parent_device=Bilbo_card_4, connection='ao5')
AnalogOut(name='A2_7_Na_img_freq', parent_device=Bilbo_card_4, connection='ao6')
AnalogOut(name='A2_8_Sirah_AOM', parent_device=Bilbo_card_4, connection='ao7')

#CARD 5 (Gollum) : This is a 6733 card. All the channels out of this card are defined below.
#digital channels

DigitalOut(name='D4_1_RF_switch',parent_device=Gollum_card_5,connection='port0/line0')
DigitalOut(name='D4_2_Retiga_trigger',parent_device=Gollum_card_5, connection='port0/line1')
DigitalOut(name='D4_3_Nuvu_trigger',parent_device=Gollum_card_5,connection='port0/line2')
DigitalOut(name='D4_5_free',parent_device=Gollum_card_5,connection='port0/line4')
DigitalOut(name='D4_6_Synth_switch',parent_device=Gollum_card_5,connection='port0/line5')
DigitalOut(name='D4_8_small_slower_switch',parent_device=Gollum_card_5, connection='port0/line7')
DigitalOut(name='D4_7_external_trig',parent_device=Gollum_card_5,connection='port0/line6')
DigitalOut(name='D4_4_free',parent_device=Gollum_card_5,connection='port0/line3')

#analog channels
AnalogOut(name='A3_1_broken',parent_device=Gollum_card_5,connection='ao0')
AnalogOut(name='A3_2_Offset_Y',parent_device=Gollum_card_5,connection='ao1')
AnalogOut(name='A3_3_Offset_Z',parent_device=Gollum_card_5,connection='ao2')
AnalogOut(name='A3_4_comp_coil_cur',parent_device=Gollum_card_5,connection='ao3')
AnalogOut(name='A3_5_small_slower_cur',parent_device=Gollum_card_5, connection='ao4')
AnalogOut(name='A3_6_Big_slower_cur',parent_device=Gollum_card_5,connection='ao5')
AnalogOut(name='A3_7_ODT1_Setpoint',parent_device=Gollum_card_5,connection='ao6')
AnalogOut(name='A3_8_ODT2_Setpoint',parent_device=Gollum_card_5,connection='ao7')


#CARD 2 (Gandalf) : This is a 6254 card. All the channels out of this card are defined below.
#digital channels

Shutter(name='D3_1_Sirah_shutter',parent_device=Gandalf_card_2,connection='port0/line0')
```

```
DigitalOut(name='D3_2_Home_AOM_switch',parent_device=Gandalf_card_2,
    connection='port0/line1')
DigitalOut(name='D3_3_RSD_Y_fast',parent_device=Gandalf_card_2,connection='
    port0/line2')
DigitalOut(name='D3_4_SSODT2_AOM',parent_device=Gandalf_card_2,connection='
    port0/line3')
DigitalOut(name='D3_5_sirah_lattice_AOM_switch',parent_device=
    Gandalf_card_2,connection='port0/line4')
Shutter(name='D3_6_sirah_lattice_shutter',parent_device=Gandalf_card_2,
    connection='port0/line5')
DigitalOut(name='D3_7_chiller_trigger',parent_device=Gandalf_card_2,
    connection='port0/line6')
DigitalOut(name='D3_8_passbank_trigger',parent_device=Gandalf_card_2,
    connection='port0/line7')
DigitalOut(name='D3_9_Li_slower_AOM_switch',parent_device=Gandalf_card_2,
    connection='port0/line8')
DigitalOut(name='D3_10_Li_repumper_AOM_switch',parent_device=Gandalf_card_2
    ,connection='port0/line9')
DigitalOut(name='D3_11_Li_umpump_repumper_AOM_switch',parent_device=
    Gandalf_card_2,connection='port0/line10')
DigitalOut(name='D3_12_Li_MOT_AOM_switch',parent_device=Gandalf_card_2,
    connection='port0/line11')
DigitalOut(name='D3_13_Li_imaging_AOM_switch',parent_device=Gandalf_card_2,
    connection='port0/line12')
Shutter(name='D3_14_Li_imaging_shutter',parent_device=Gandalf_card_2,
    connection='port0/line13')
Shutter(name='D3_15_Li_MOT_shutter',parent_device=Gandalf_card_2,connection
    ='port0/line14')
DigitalOut(name='D3_16_Li_umpump_AOM_switch',parent_device=Gandalf_card_2,
    connection='port0/line15')
DigitalOut(name='D3_17_dimple_AOM_switch',parent_device=Gandalf_card_2,
    connection='port0/line16')
DigitalOut(name='D3_18_waveguide_AOM_switch',parent_device=Gandalf_card_2,
    connection='port0/line17')
DigitalOut(name='D3_19_Bfield_sample',parent_device=Gandalf_card_2,
    connection='port0/line18')
Shutter(name='D3_20_atomic_beam_shutter',parent_device=Gandalf_card_2,
    connection='port0/line19')
DigitalOut(name='D3_21_broken',parent_device=Gandalf_card_2,connection='
    port0/line20')
DigitalOut(name='D3_22_not_in_use',parent_device=Gandalf_card_2,connection=
    'port0/line21')
DigitalOut(name='D3_23_arduino_reset',parent_device=Gandalf_card_2,
    connection='port0/line22')
DigitalOut(name='D3_24_not_in_use',parent_device=Gandalf_card_2,connection=
    'port0/line23')
DigitalOut(name='D3_25_MOT_IGBT',parent_device=Gandalf_card_2,connection='
    port0/line24')
DigitalOut(name='D3_26_DDS_trigger',parent_device=Gandalf_card_2,connection
    ='port0/line25')
DigitalOut(name='D3_29_FT_HH_IGBT',parent_device=Gandalf_card_2,connection=
    'port0/line28')
DigitalOut(name='D3_30_bias_IGBT',parent_device=Gandalf_card_2,connection='
    port0/line29')
DigitalOut(name='D3_31_curvture_IGBT',parent_device=Gandalf_card_2,
    connection='port0/line30')
```

```
DigitalOut(name='D3_32_MW_trigger',parent_device=Gandalf_card_2,connection=
    'port0/line31')
MakoCamera('mako',Gollum_card_5,'port0/line0',18517)
#the connection table ends here

#here begins experimental script.
#-----------------------------------------------------
DDS_string = 'Rt'+ str(int(dt_MWclean)) + 'f' + str(int(MWclean_start)) + '
    F' + str(int(MWclean_stop))+\
'Rt'+ str(int(dt_RFcool1)) + 'f' + str(int(RFcool1_start)) + 'F' + str(int(
    RFcool1_stop))+\
'Rt'+ str(int(dt_RFcool2)) + 'f' + str(int(RFcool2_start)) + 'F' + str(int(
    RFcool2_stop))+\
'Rt' + str(int(dt_MW_transfer*1e6))+'f'+ str(int(MW_F2F1_center-
    MW_F2F1_halfrange)) + 'F' + str(int(MW_F2F1_center+MW_F2F1_halfrange))

#one has to enode the strings.
ramp = str.encode(DDS_string)
arduino.add_start_command(b'r' +ramp + b'z' )
arduino.add_stop_command(b'The shot is over\r\n')

#the functions are imported from the folder pythonlib
#-----------------------------------------------------
from set_initial_values import SetChannels
from MOT_Na_Li import loadsodiumMOT, getsodiumMOT, End_NaMOT, getlithiumMOT
    , loadlithiumMOT, rampMOT
from Spin_polarization import UMPUMP, SpinPol
from Magnetic_trap import LoadMT, OpenMT, EndMT, Compress_MT,  MWclean,
    RFcooling1, RFcooling2
from ODT import Hold_ODT_MT,load_Waveguide,load_dimple, ODT_off,
    ODT_off_after_lattice, Offset_Ramp,MW_transfer,ODT_ramp
from Imaging_retiga_test import Na_Image_atoms, Na_dark_pic, Li_Image_atoms
    , Li_dark_pic
from SG import Stern_Gerlach, RabiOsc, Ramsey

#define every function in class formalism.
#-----------------------------------------------------
class ExperimentClass():
    def __init__(self):
        self.t = 0
ExperimentClass.SetChannels = SetChannels
ExperimentClass.loadsodiumMOT = loadsodiumMOT
ExperimentClass.End_NaMOT = End_NaMOT
ExperimentClass.getsodiumMOT = getsodiumMOT
ExperimentClass.getlithiumMOT = getlithiumMOT
ExperimentClass.loadlithiumMOT = loadlithiumMOT
ExperimentClass.rampMOT = rampMOT
ExperimentClass.UMPUMP = UMPUMP
ExperimentClass.SpinPol = SpinPol
ExperimentClass.LoadMT = LoadMT
ExperimentClass.OpenMT = OpenMT
ExperimentClass.EndMT = EndMT
ExperimentClass.Compress_MT = Compress_MT
ExperimentClass.MWclean = MWclean
ExperimentClass.RFcooling1 = RFcooling1
ExperimentClass.RFcooling2 = RFcooling2
```

```
164 ExperimentClass.Hold_ODT_MT = Hold_ODT_MT
    ExperimentClass.load_Waveguide = load_Waveguide
166 ExperimentClass.load_dimple = load_dimple
    ExperimentClass.ODT_off = ODT_off
168 ExperimentClass.Offset_Ramp = Offset_Ramp
    ExperimentClass.MW_transfer = MW_transfer
170 ExperimentClass.ODT_ramp = ODT_ramp
    ExperimentClass.Na_Image_atoms = Na_Image_atoms
172 ExperimentClass.Na_dark_pic = Na_dark_pic
    ExperimentClass.Li_Image_atoms = Li_Image_atoms
174 ExperimentClass.Li_dark_pic = Li_dark_pic
    ExperimentClass.Stern_Gerlach = Stern_Gerlach
176 ExperimentClass.imaging = imaging
    Experiment = ExperimentClass()
178 #here ends the importing---------------------------------

180 #the experimental cycle begins.
    start()
182 Experiment.t = 0
    #initialise all the channels
184 Experiment.SetChannels()
    #load the MOTs one by one.
186 if use_LiMOT == True:
        Experiment.loadlithiumMOT(dt_LiMOT)
188     Experiment.rampMOT(dt_RampMOT)
    if use_NaMOT == True:
190     Experiment.loadsodiumMOT(use_LiMOT,dt_cMOT,dt_NaMOT)

192 #start optical pumping scheme for spinpurification process.
    if use_Umpump == True:
194     Experiment.UMPUMP()
    if use_Spinpol == True:
196     Experiment.SpinPol(dt_rampdown_ft, dt_Umpump, use_LiMOT)

198 #load into the magnetic trap, by ramping up the curvature, gradient and
        bias power supplies.
    if use_MT == True:
200     Experiment.LoadMT(dt_loadMT)

202 #here we throw away atoms from F=1, since we make use of only F=2 atoms in
        the MT
    if use_MWclean == True:
204     Experiment.MWclean(dt_MWclean)
    else:
206     Experiment.t += 5*1e-6
        print('Skipping MW clean')
208
    #change the current values for MT coils to make the MT confinement tighter
210 if use_CompressMT == True:
        Experiment.Compress_MT(dt_CompressMT)
212 else:
        if Get_Li_MOT == True and use_NaMOT== True:
214         A3_5_small_slower_cur.exp_ramp_t(self.t-50e-3, duration = 50e-3,
        initial = Na_small_slower_cur, final = 0, time_constant = 50e-3,
        samplerate =4e4 , trunc=False, units=None)
```

```
        A3_4_comp_coil_cur.exp_ramp_t(self.t-50e-3, duration = 50e-3,
    initial = Na_comp_coil_cur, final = 0, time_constant = 50e-3, samplerate
     =4e4 , trunc=False, units=None)
216         A3_6_Big_slower_cur.exp_ramp_t(self.t-50*1e-3, duration = 50*1e-3,
    initial = big_slower_cur, final = 0, time_constant = 50e-3,samplerate =
    4e4,trunc=False, units=None)
        print('Skipping Compressed MT')
218
#here start two evaporative cooling ramps
220 if use_RFcool1 == True:
    Experiment.RFcooling1(dt_RFcool1)
222 else:
    print('Skipping first evaporative cooling')
224
if use_RFcool2 == True:
226     Experiment.RFcooling2(dt_RFcool2)
else:
228     print('Skipping second evaporative cooling')

230 #load into the dipole trap, first into waveguide(ODT2, horizontal)
if use_ODT2_waveguide == True:
232     Experiment.Hold_ODT_MT(dt_Hold)
    Experiment.load_Waveguide(dt_loadODT)
234 else:
    print('No ODT')
236
#reduce the current values in the coils, thus reducing the MT confinement
238 if use_OpenMT == True:
    Experiment.OpenMT(dt_OpenMT)
240
#ramping up the offset field, and then do Rapid Adiabatic Passage to
    transfer from F=2 to F=1
242 if use_MW_transfer == True:
    Experiment.t += dt_offset_delay; #comment this if you want to go to the
     old way
244     Experiment.Offset_Ramp(dt_Offset_ramp,dt_offset_delay)
     # here we start the active magnetic field stabilization
246     Experiment.MW_transfer(dt_MW_transfer)
else:
248     print('No MW transfer')

250 #load the second dipole trap beam, dimple(ODT1, vertical)
if use_ODT1_dimple == True:
252     Experiment.load_dimple(dt_ramp_dimple)
    Experiment.t += 0.1;
254     Experiment.ODT_ramp(dt_odt_ramp_final)
else:
256     print('No dimple')

258 #switching off the traps.
#when ODT is NOT used
260 if use_EndMT == True:
    Experiment.EndMT(dt_MT_turnoff)
262
#when ODT is used, switch it off prior to SG
264 if use_SG == True:
```

```
    Experiment.ODT_off()
266     Experiment.Stern_Gerlach(dt_SG)
elif use_ODT == True:
268     Experiment.ODT_off()

270 #IMAGING----------------------------------------
Experiment.t += dt_TOFNa;
272
if use_Na_imaging == True:
274     Experiment.Na_Image_atoms(dt_Na_repump,dt_Na_img_laser_duration)
    if use_Li_imaging == True:
276         Experiment.Li_Image_atoms(dt_Li_repump,dt_Li_img_laser_duration,
    dt_Li_img_shutter_duration,dt_TOFLi)
    Experiment.t += dt_refpic_delay;
278     Experiment.Na_Image_atoms(dt_Na_repump,dt_Na_img_laser_duration)
    if use_Li_imaging == True:
280         Experiment.Li_Image_atoms(dt_Li_repump,dt_Li_img_laser_duration,
    dt_Li_img_shutter_duration,dt_TOFLi)
    Experiment.t += dt_blackpic_delay;
282     Experiment.Na_dark_pic(dt_Na_img_shutter_duration)
    if use_Li_imaging == True:
284         Experiment.Li_dark_pic(dt_Li_img_shutter_duration)

286 stop(Experiment.t);
```

List of Figures

List of Tables

Bibliography

[1] A. Mil, T. V. Zache, A. Hegde, A. Xia, R. P. Bhatt, M. K. Oberthaler, P. Hauke, J. Berges, and F. Jendrzejewski. A scalable realization of local U(1) gauge invariance in cold atomic mixtures. *Science*, 367(6482):1128–1130, 2020.

[2] R.Y. Rubinstein and D.P. Kroese. *Simulation and the Monte Carlo Method: Third Edition*. 11 2016.

[3] B. Alder Ceperley, D. Quantum Monte Carlo. *Science*, 231:555–560, 1986.

[4] F. Verstraete, V. Murg, and J.I. Cirac. Matrix product states, projected entangled pair states, and variational renormalization group methods for quantum spin systems. *Advances in Physics*, 57(2):143–224, 2008.

[5] Tim Langen, Remi Geiger, and Jörg Schmiedmayer. Ultracold Atoms Out of Equilibrium. *Annu. Rev. Condens. Matter Phys.*, 6(1):201–217, 2015.

[6] R. P. Feynman. Simulating physics with computers. *Int. J. Theor. Phys.*, 21(6-7):467–488, 1982.

[7] T. H. Johnson, S. R. Clark, and D. Jaksch. What is a quantum simulator? *EPJ Quantum Technol.*, 1(1):1–12, 2014.

[8] J. Ignacio Cirac and Peter Zoller. Goals and opportunities in quantum simulation. *Nat. Phys.*, 8(4):264–266, 2012.

[9] I. Buluta and F. Nori. Quantum Simulators. *Science*, 326(1):108, 2009.

[10] Isaac L. Chuang Michael A. Nielsen. *Quantum Computation and Quantum Information*. Cambridge University Press, 10 edition, 2010.

[11] S. Lloyd. Universal quantum simulators. *Science*, 273(5278):1073–1078, 1996.

[12] Laszlo G. and S. Imre. A survey on quantum computing technology. *Computer Science Review*, 31:51–71, 2019.

[13] Philipp Hauke, Fernando M. Cucchietti, Luca Tagliacozzo, Ivan Deutsch, and MacIej Lewenstein. Can one trust quantum simulators? *Reports Prog. Phys.*, 75, 2012.

[14] V. M. Kendon, K. Nemoto, and W. J. Munro. Quantum analogue computing. *Philos. Trans. R. Soc. A Math. Phys. Eng. Sci.*, 368(1924):3609–3620, 2010.

[15] R. Blatt and C. F. Roos. Quantum simulations with trapped ions. *Nat. Phys.*, 8, 2012.

[16] C. Monroe, W. C. Campbell, L. M. Duan, Z. X. Gong, A. V. Gorshkov, P. W. Hess, R. Islam, K. Kim, N. M. Linke, G. Pagano, P. Richerme, C. Senko, and N. Y. Yao. Programmable quantum simulations of spin systems with trapped ions. *Rev. Mod. Phys.*, 93, 2021.

[17] P. Barthelemy and Lieven M.K. Vandersypen. Quantum Dot Systems: A versatile platform for quantum simulations. *Ann. Phys.*, 525(10-11):808–826, 2013.

[18] M. Kjaergaard, M. E. Schwartz, J. Braumüller, P. Krantz, Joel I.J. Wang, S. Gustavsson, and W. D. Oliver. Superconducting Qubits: Current State of Play. *Annu. Rev. Condens. Matter Phys.*, 11:369–395, 2020.

[19] G. S. Paraoanu. Recent progress in quantum simulation using superconducting circuits. *J. Low Temp. Phys.*, 175(5-6):633–654, 2014.

[20] A. Aspuru-Guzik and P. Walther. Photonic quantum simulators. *Nat. Phys.*, 8(4):285–291, 2012.

[21] A. Browaeys and T. Lahaye. Many-body physics with individually controlled Rydberg atoms. *Nat. Phys.*, 16(2):132–142, 2020.

[22] Immanuel Bloch, Jean Dalibard, and Sylvain Nascimbène. Quantum simulations with ultracold quantum gases. *Nat. Phys.*, 8:267–276, 2012.

[23] Maciej Lewenstein, Anna Sanpera, Veronica Ahufinger, Bogdan Damski, Aditi Sen(De), and Ujjwal Sen. Ultracold atomic gases in optical lattices: mimicking condensed matter physics and beyond. *Advances in Physics*, 56(2):243–379, 2007.

[24] J. A. Blackmore, L. Caldwell, P. D. Gregory, E. M. Bridge, R. Sawant, J. Aldegunde, J. Mur-Petit, D. Jaksch, J. M. Hutson, B. E. Sauer, M. R. Tarbutt, and S. L. Cornish. Ultracold molecules for quantum simulation: Rotational coherences in CaF and RbCs. *Quantum Sci. Technol.*, 4(1), 2019.

[25] W. D. Phillips. Laser cooling and trapping of neutral atoms. *Nobel Lecture.*, 1997.

[26] F. London. On the bose-einstein condensation. *Phys. Rev.*, 54:947–954, Dec 1938.

[27] M. H. Anderson, J. R. Ensher, M. R. Matthews, C. E. Wieman, and E. A. Cornell. Observation of bose-einstein condensation in a dilute atomic vapor. *Science*, 269(5221):198–201, 1995.

[28] C. C. Bradley, C. A. Sackett, J. J. Tollett, and R. G. Hulet. Evidence of bose-einstein condensation in an atomic gas with attractive interactions. *Phys. Rev. Lett.*, 75:1687–1690, Aug 1995.

[29] K. B. Davis, M. Mewes, M. R. Andrews, N. J. Van Druten, D. S. Durfee, D. M. Kurn, and W. Ketterle. Bose-Einstein Condensation in a Gas of Sodium Atoms. (November):3969–3973, 1995.

[30] S. L. Rolston and W. D. Phillips. Nonlinear and quantum atom optics. *Nature*, 416(6877):219–224, 2002.

[31] Dan M. Stamper-Kurn and Masahito Ueda. Spinor Bose gases: Symmetries, magnetism, and quantum dynamics. *Rev. Mod. Phys.*, 85(3):1191–1244, 2013.

[32] S. Inouye, M. R. Andrews, J. Stenger, H. J. Mlesner, D. M. Stamper-Kurn, and W. Ketterle. Observation of Feshbach resonances in a Bose-Einstein condensate. *Nature*, 392(6672):151–154, 1998.

[33] D. Jaksch, C. Bruder, J. I. Cirac, C. W. Gardiner, and P. Zoller. Cold bosonic atoms in optical lattices. *Phys. Rev. Lett.*, 81:3108–3111, Oct 1998.

[34] B. DeMarco and D. S. Jin. Onset of Fermi degeneracy in a trapped atomic gas. *Science*, 285(5434):1703–1706, 1999.

[35] K. M. O'Hara, S. L. Hemmer, M. E. Gehm, S. R. Granade, and J. E. Thomas. Observation of a strongly interacting degenerate fermi gas of atoms. *Science*, 298:2179–2182, 2002.

[36] M. Greiner, O. Mandel, T. Rom, A. Altmeyer, A. Widera, T. W. Hänsch, and I. Bloch. Quantum phase transition from a superfluid to a Mott insulator in an ultracold gas of atoms. *Nature*, 415:39–44, 2002.

[37] T. Bourdel, L. Khaykovich, J. Cubizolles, J. Zhang, F. Chevy, M. Teichmann, L. Tarruell, S. J.J.M.F. Kokkelmans, and C. Salomon. Experimental study of the BEC-BCS crossover region in lithium 6. *Phys. Rev. Lett.*, 93(5), 2004.

[38] S. Jochim, M. Bartenstein, A. Altmeyer, G. Hendl, S. Riedl, C. Chin, J. Hecker Denschlag, and R. Grimm. Bose-einstein condensation of molecules. *Science*, 302(5653):2101–2103, 2003.

[39] M. W. Zwierlein, C. A. Stan, C. H. Schunck, S. M.F. Raupach, S. Gupta, Z. Hadzibabic, and W. Ketterle. Observation of Bose-Einstein condensation of molecules. *Phys. Rev. Lett.*, 91(25):1–4, 2003.

[40] A. G. Truscott, K. E. Strecker, W. I. McAlexander, G. B. Partridge, and R. G. Hulet. Observation of fermi pressure in a gas of trapped atoms. *Science*, 291(5513):2570–2572, 2001.

[41] F. Schreck, L. Khaykovich, K. L. Corwin, G. Ferrari, T. Bourdel, J. Cubizolles, and C. Salomon. Quasipure bose-einstein condensate immersed in a fermi sea. *Phys. Rev. Lett.*, 87:080403, Aug 2001.

[42] Z. Hadzibabic, C. A. Stan, K. Dieckmann, S. Gupta, M. W. Zwierlein, A. Görlitz, and W. Ketterle. Two-species mixture of quantum degenerate bose and fermi gases. *Phys. Rev. Lett.*, 88:160401, Apr 2002.

[43] G. Roati, F. Riboli, G. Modugno, and M. Inguscio. Fermi-bose quantum degenerate $^{40}\mathrm{K}-^{87}\mathrm{Rb}$ mixture with attractive interaction. *Phys. Rev. Lett.*, 89:150403, Sep 2002.

[44] J. Goldwin, S. Inouye, M. L. Olsen, B. Newman, B. D. DePaola, and D. S. Jin. Measurement of the interaction strength in a bose-fermi mixture with $^{87}\mathrm{Rb}$ and $^{40}\mathrm{K}$. *Phys. Rev. A*, 70:021601, Aug 2004.

[45] P. K. Molony, P. D. Gregory, Z. Ji, B. Lu, M. P. Köppinger, C. Ruth Le S., C. L. Blackley, J. M. Hutson, and S. L. Cornish. Creation of ultracold $^{87}\mathrm{Rb}^{133}\mathrm{Cs}$ molecules in the rovibrational ground state. *Phys. Rev. Lett.*, 113:255301, Dec 2014.

[46] C. Politi, A. Trautmann, P. Ilzhöfer, G. Durastante, M. J. Mark, M. Modugno, and F. Ferlaino. Study of the inter-species interactions in an ultracold dipolar mixture. (2):1–10, 2021.

[47] R. Scelle, T. Rentrop, A. Trautmann, T. Schuster, and M. K. Oberthaler. Motional coherence of fermions immersed in a bose gas. *Phys. Rev. Lett.*, 111(7):1–5, 2013.

[48] A. Schirotzek, C. Wu, A. Sommer, and M. W. Zwierlein. Observation of fermi polarons in a tunable fermi liquid of ultracold atoms. *Phys. Rev. Lett.*, 102:230402, Jun 2009.

[49] M. Hu, Mi. J. Van de Graaff, D. Kedar, J. P. Corson, E. A. Cornell, and D. S. Jin. Bose polarons in the strongly interacting regime. *Phys. Rev. Lett.*, 117:055301, Jul 2016.

[50] S. Tomonaga. On a Relativistically Invariant Formulation of the Quantum Theory of Wave Fields*. *Progress of Theoretical Physics*, 1(2):27–42, 08 1946.

[51] J. Schwinger. Quantum electrodynamics. i. a covariant formulation. *Phys. Rev.*, 74:1439–1461, Nov 1948.

[52] R. P. Feynman. Space-time approach to quantum electrodynamics. *Phys. Rev.*, 76:769–789, Sep 1949.

[53] I. Montvay and G. Munster. *Quantum fields on a lattice*. Cambridge Monographs on Mathematical Physics. Cambridge University Press, 3 1997.

[54] K. G. Wilson. *Quarks and Strings on a Lattice*. 1977.

[55] Michael Creutz, Laurence Jacobs, and Claudio Rebbi. Experiments with a gauge-invariant Ising system. *Phys. Rev. Lett.*, 42(21):1390–1393, 1979.

[56] M. C. Banuls, R. Blatt, J. Catani, A. Celi, J. I. Cirac, M. Dalmonte, L. Fallani, K. Jansen, S. Montenagro, A.C. Muschik, B. Reznik, E. Rico, L. Tagliacozzo, K. Van Acoleyen, F. Veestraete, U.J. Wiese, M. Wingate, J. Zakrzewski, and P. Zoller. Simulating Lattice Gauge theories. *Eur. Phys. J. D*, 2020.

[57] U. J. Wiese. Ultracold quantum gases and lattice systems: Quantum simulation of lattice gauge theories. *Ann. Phys.*, 525:777–796, 2013.

[58] M. Dalmonte and S. Montangero. Lattice gauge theory simulations in the quantum information era. *Contemp. Phys.*, 7514:1–25, 2016.

[59] M. Aidelsburger, L. Barbiero, A. Bermudez, T. Chanda, A. Dauphin, D. González-Cuadra, Przemysław R. Grzybowski, S. Hands, F. Jendrzejewski, J. Jünemann, G. Juzeliunas, V. Kasper, A. Piga, S. Ran, M. Rizzi, G. Sierra, L. Tagliacozzo, E. Tirrito, T. V. Zache, J. Zakrzewski, E. Zohar, and M. Lewenstein. Cold atoms meet lattice gauge theory. *Philos. Trans. R. Soc. A*, 2021.

[60] E. Zohar, J. I. Cirac, and B. Reznik. Quantum simulations of gauge theories with ultracold atoms: Local gauge invariance from angular-momentum conservation. *Phys. Rev. A - At. Mol. Opt. Phys.*, 88:1–24, 2013.

[61] Julian Schwinger. Gauge invariance and mass. ii. *Phys. Rev.*, 128:2425–2429, Dec 1962.

[62] J. Kogut and L. Susskind. Hamiltonian formulation of Wilson's lattice gauge theories. *Phys. Rev. D*, 11(2):395–408, 1975.

[63] E. A. Martinez, C. A. Muschik, P. Schindler, D. Nigg, A. Erhard, M. Heyl, P. Hauke, M. Dalmonte, T. Monz, P. Zoller, and R. Blatt. Real-time dynamics of lattice gauge theories with a few-qubit quantum computer. *Nature*, 534:516–519, 2016.

[64] C.J. Hamer, J. Kogut, D.P. Crewther, and M.M. Mazzolini. The massive schwinger model on a lattice: Background field, chiral symmetry and the string tension. *Nuclear Physics B*, 208(3):413–438, 1982.

[65] T. M. R. Byrnes, P. Sriganesh, R. J. Bursill, and C. J. Hamer. Density matrix renormalization group approach to the massive schwinger model. *Phys. Rev. D*, 66:013002, Jul 2002.

[66] M. C. Bañuls, K. Cichy, J. I. Cirac, and K. Jansen. The mass spectrum of the Schwinger model with matrix product states. *J. High Energy Phys.*, 2013(11), 2013.

[67] V. Kasper, F. Hebenstreit, M.K. Oberthaler, and J. Berges. Schwinger pair production with ultracold atoms. *Physics Letters B*, 760, 06 2015.

[68] Julian Schwinger. On gauge invariance and vacuum polarization. *Phys. Rev.*, 82:664–679, Jun 1951.

[69] C. Kokail, C. Maier, R. van Bijnen, T. Brydges, M. K. Joshi, P. Jurcevic, C. A. Muschik, P. Silvi, R. Blatt, C. F. Roos, and P. Zoller. Self-verifying variational quantum simulation of lattice models. *Nature*, 569(7756):355–360, 2019.

[70] H. Bernien, S. Schwartz, A. Keesling, H. Levine, A. Omran, H. Pichler, S. Choi, A. S. Zibrov, M. Endres, M. Greiner, V. Vuletic, and M. D. Lukin. Probing many-body dynamics on a 51-atom quantum simulator. *Nature*, 551(7682):579–584, 2017.

[71] Subir Sachdev. *Quantum Phase Transitions*. Cambridge University Press, 2 edition, 2011.

[72] F. M. Surace, P. P. Mazza, G. Giudici, A. Lerose, A. Gambassi, and M. Dalmonte. Lattice gauge theories and string dynamics in rydberg atom quantum simulators. *Phys. Rev. X*, 10:021041, May 2020.

[73] B. Yang, H. Sun, R. Ott, H. Y. Wang, T. V. Zache, J. C. Halimeh, Z. S. Yuan, P. Hauke, and J. W. Pan. Observation of gauge invariance in a 71 site Bose Hubbard quantum simulator. *Nature*, 587(7834):392–396, 2020.

[74] Christian Schweizer, Fabian Grusdt, Moritz Berngruber, Luca Barbiero, Eugene Demler, Nathan Goldman, Immanuel Bloch, and Monika Aidelsburger. Floquet approach to Z2 lattice gauge theories with ultracold atoms in optical lattices. *Nat. Phys.*, 15(11):1168–1173, 2019.

[75] H. N. Dai, B. Yang, A. Reingruber, H. Sun, X. F. Xu, Y. A. Chen, Z. S. Yuan, and J. W. Pan. Four-body ring-exchange interactions and anyonic statistics within a minimal toric-code Hamiltonian. *Nat. Phys.*, 13(12):1195–1200, 2017.

[76] Lifshitz L.D. Landau, E.M. *Statistical Physics.* Pergamon Press Ltd., 2 edition, 1969.

[77] C.J. Pethick Smith, H. *Bose-Einstein Condensation in Dilute Gases.* Cambridge University Press, 2002.

[78] J. B. Kogut. The lattice gauge theory approach to quantum chromodynamics. *Rev. Mod. Phys.*, 55(3):775–836, 1983.

[79] T. V. Zache, F. Hebenstreit, F. Jendrzejewski, M. K. Oberthaler, J. Berges, and P. Hauke. Quantum simulation of lattice gauge theories using Wilson fermions. *Quantum Sci. Technol.*, pages 1–19, 2018.

[80] V. Kasper, F. Hebenstreit, F. Jendrzejewski, M. K. Oberthaler, and J. Berges. Implementing quantum electrodynamics with ultracold atomic systems. *New J. Phys.*, pages 1–22, 2017.

[81] T.V Zache. Quantum simulation of high-energy physics with ultracold atoms. *PhD thesis.*

[82] Assa Auerbach. Interacting Electrons and Quantum Magnetism, 1994.

[83] Eite Tiesinga, Carl J. Williams, Paul S. Julienne, Kevin M. Jones, Paul D. Lett, and William D. Phillips. A spectroscopic determination of scattering lengths for sodium atom collisions. *J. Res. Natl. Inst. Stand. Technol.*, 101(4), 1996.

[84] Alexander Mil. *Experimental realization of U(1) gauge invariance in ultracold atomic mixtures.* PhD thesis, 2020.

[85] R. P. Feynman, F. L. Vernon, and R. W. Hellwarth. Geometrical Representation of the Schrödinger Equation for Solving Maser Problems. *J. Appl. Phys.*, 28(1):49–52, 1957.

[86] J.J. Sakurai, Jim Napolitano. *Modern Quantum Mechanics.*

[87] M. Ueda M. Kitagawa. Squeezed spin states. *Phys. Rev. A*, 47, 1993.

[88] Lifshitz L.D. Landau, E.M. *Quantum mechanics, Non-relativistic theory.* Pergamon Press, 1958.

[89] Anton Piccardo-Selg. Degenerate Quantum Gases: Towards Bose-Einstein Condensation of Sodium. Diploma thesis. 2008.

[90] Jens Appmeier. *Immersed Quantum Systems: A Sodium Bose-Einstein Condensate for Polaron Studies.* PhD thesis, 2010.

[91] Tobias Schuster. Feshbach Resonances and Periodic Potentials in Ultracold Bose-Fermi Mixtures. 2012.

[92] Tobias Rentrop. *Observation of the Phononic Lamb Shift in a Synthetic Vacuum.* PhD thesis, 2016.

[93] Fabian Olivares. *Towards Lattice Gauge Theories in Ultracold Mixtures of Sodium and Lithium.* PhD thesis, 2018.

[94] C. A. Stan and W. Ketterle. Multiple species atom source for laser-cooling experiments. *Rev. Sci. Instrum.*, 76(6), 2005.

[95] Marc Repp. *Aufbau einer Vakuumapparatur f¨ur Experimente mit ultrakalten fermionischen und bosonischen Quantengasen.* PhD thesis, 2007.

[96] Christopher J. Foot. *Atomic physics.* Oxford University Press, 2005.

[97] Robert W. Boyd. *Nonlinear Optics, Third Edition.* Academic Press, Inc., USA, 3rd edition, 2008.

[98] Arno Trautmann. *Spin Dynamics and Feshbach Resonances in Ultracold Sodium-Lithium Mixtures.* PhD thesis, 2016.

[99] Tanja Behrle. Construction and Characterization of a Diode Laser Setup and Spectroscopy Cell for ^{6}Li and ^{7}Li. Bachelor thesis. 2014.

[100] TOPTICA Photonics AG. Compact Fiber Coupler Manual. 2015.

[101] Matthias Heinrich. Design and Realization of a Laser System for ATTA of Argon-39. Diploma thesis. 2010.

[102] U. Schünemann, H. Engler, R. Grimm, M. Weidemüller, and M. Zielonkowski. Simple scheme for tunable frequency offset locking of two lasers. *Rev. Sci. Instrum.*, 70(1 PART II):242–243, 1999.

[103] Arno Trautmann. Feshbach Spectroscopy of Sodium and Sodium-Lithium Mixtures. Diploma thesis. 2011.

[104] W. D. Phillips Metcalf and H. Laser Deceleration of an Atomic Beam. *J. Exp. Mar. Bio. Ecol.*, 48, 1982.

[105] E. Pedrozo-Peñafiel, F. Vivanco, P. Castilho, R. R. Paiva, K. M. Farias, and V. S. Bagnato. Direct comparison between a two-dimensional magneto-optical trap and a Zeeman slower as sources of cold sodium atoms. *Laser Phys. Lett.*, 13(6), 2016.

[106] Jan Krieger. Zeeman-Slower und Experimentsteuerung für das NaLi-Experiment. Diploma thesis. page 130, 2008.

[107] E. L. Raab, M. Prentiss, Alex Cable, Steven Chu, and D. E. Pritchard. Trapping of Neutral Sodium Atoms with Radiation Pressure. *Phys. Rev. Lett.*, 59(23):2631–2634, 1987.

[108] W. Ketterle, K. B. Davis, M. A. Joff, A. Martin, and D. E. Pritchard. High Densities of Cold Atoms in a Dark Spontaneous-Force Optical Trap. 70(15):2253–2256, 1993.

[109] Samuel Earnshaw. On the Nature of the Molecular Forces which Regulate the Constitution of the Luminiferous Ether, 1842.

[110] A. Görlitz, T. L. Gustavson, A. E. Leanhardt, R. Löw, A. P. Chikkatur, S. Gupta, S. Inouye, D. E. Pritchard, and W. Ketterle. Sodium Bose-Einstein Condensates in the [Formula presented] State in a Large-Volume Optical Trap. *Phys. Rev. Lett.*, 90(9):4, 2003.

[111] A. S. Sanz J. Perez-Rios. How does a magnetic trap work ? *Am. J. Phys.*, 81(836), 2013.

[112] Raphael Scelle. *Dynamics and Motional Coherence of Fermions Immersed in a Bose Gas.* PhD thesis, 2013.

[113] David E. Pritchard. Cooling neutral atoms in a magnetic trap for precision spectroscopy. *Phys. Rev. Lett.*, 51(15):1336–1339, 1983.

[114] Z. Hadzibabic, S. Gupta, C. A. Stan, C. H. Schunck, M. W. Zwierlein, K. Dieckmann, and W. Ketterle. Fiftyfold improvement in the number of quantum degenerate fermionic atoms. *Phys. Rev. Lett.*, 91(16):16–19, 2003.

[115] K. M.R. Van Der Stam, A. Kuijk, R. Meppelink, J. M. Vogels, and P. Van Der Straten. Spin-polarizing cold sodium atoms in a strong magnetic field. *Phys. Rev. A - At. Mol. Opt. Phys.*, 73(6):1–7, 2006.

[116] F. Schreck, G. Ferrari, K. L. Corwin, J. Cubizolles, L. Khaykovich, M. O. Mewes, and C. Salomon. Sympathetic cooling of bosonic and fermionic lithium gases towards quantum degeneracy. *Phys. Rev. A. At. Mol. Opt. Phys.*, 64(1):114021–114024, 2001.

[117] C. J. Myatt, E. A. Burt, R. W. Christ, E. A. Cornell, and C. E. Wieman. Production of two verlapping bose-einstein condensates by sympathetic cooling. *Phys. Rev. Lett.*, 1997.

[118] M. O. Mewes, M. R. Andrews, N. J. Van Druten, D. M. Kurn, D. S. Durfee, and W. Ketterle. Bose-einstein condensation in a tightly confining dc magnetic trap. *Phys. Rev. Lett.*, 77(3):416–419, 1996.

[119] M. D. Barrett, J. A. Sauer, and M. S. Chapman. All-optical formation of an atomic bose-einstein condensate. *Phys. Rev. Lett.*, 87(1):1–4, 2001.

[120] T. Weber, J. Herbig, M. Mark, H. C Nägerl, and R. Grimm. Bose-Einstein condensation of cesium. *Science*, 299(5604):232–235, 2003.

[121] D. M. Stamper-Kurn, M. R. Andrews, A. P. Chikkatur, S. Inouye, H. J. Miesner, J. Stenger, and W. Ketterle. Optical confinement of a bose-einstein condensate. *Phys. Rev. Lett.*, 80(10):2027–2030, 1998.

[122] S. Chu, J. E. Bjorkholm, A. Ashkin, and A. Cable. Experimental Observation of Optically Trapped Atoms. *Phys. Rev. Lett.*, 57, 1986.

[123] C.S. Adams, H. J. Lee, N. Davidson, M. Kasevich, and S. Chu. Evaporative Cooling in a Crossed Dipole Trap. 74(18):3577–3581, 1995.

[124] Peter van der Straten Harold J. Metcalf. *Laser Cooling andf Trapping.* Springer-Verlag New York, Inc.

[125] W. Ketterle, D. S. Durfee, and D. M. Stamper-Kurn. Making, probing and understanding Bose-Einstein condensates. 1999.

[126] G Reinaudi, T Lahaye, and D. Guéry-Odelin Wang, Z. Strong saturation absorption imaging of dense clouds of ultracold atoms. 32(21):3143–3145, 2007.

[127] Alexander Mil. Design and Implementation of a Versatile Imaging Objective for Imaging of Ultracold Mixtures of Sodium and Lithium. Master thesis. 2016.

[128] PXI-1033 User Manual. (October), 2019.

[129] Thomas Starkey Philip. *A software framework for control and automation of precisely timed experiments*. PhD thesis, 2019.

[130] Christopher Billington. *State-dependent forces in cold quantum gases*. PhD thesis, 2018.

[131] P. T. Starkey, C. J. Billington, S. P. Johnstone, M. Jasperse, K. Helmerson, L. D. Turner, and R. P. Anderson. A scripted control system for autonomous hardware-timed experiments. *Rev. Sci. Instrum.*, 84(8), 2013.

[132] G. Breit and I. I. Rabi. Mesurement of Nuclear Spin. *Phys. Rev.*, 38(11):2082, 1931.

[133] Marcell W. Gall. Active Magnetic Field Stabilisation for Ultracold Sodium Lithium Mixtures. Master thesis. 2012.

[134] P. Kunkel, M. Prüfer, S. Lannig, R. Rosa-Medina, A. Bonnin, M. Gärttner, H. Strobel, and M. K. Oberthaler. Simultaneous Readout of Noncommuting Collective Spin Observables beyond the Standard Quantum Limit. *Phys. Rev. Lett.*, 123(6):63603, 2019.

[135] G. E. Marti and D. M. Stamper-Kurn. Spinor Bose-Einstein gases. 2015.

[136] O. Stern W. Gerlach. Uber dae Richtungsquantelung im Nagnetfeld. 1924.

[137] C. F. Ockeloen, A. F. Tauschinsky, R. J.C. Spreeuw, and S. Whitlock. Detection of small atom numbers through image processing. *Phys. Rev. A - At. Mol. Opt. Phys.*, 82(6), 2010.

[138] L. Niu, X. Guo, Y. Zhan, X. Chen, W. M. Liu, and X. Zhou. Optimized fringe removal algorithm for absorption images. *Appl. Phys. Lett.*, 113(14), 2018.

[139] W. Ketterle J. Stenger, S. Inouye, D. M. Stamper-Kurn, H.-J. Miesner, A. P. Chikkatur. Spin domains in ground-state Bose Einstein condensates. *Nature*, 396:345–348, 1998.

[140] W. M. Itano, J. C. Bergquist, J. J. Bollinger, J. M. Gilligan, D. J. Heinzen, F. L. Moore, M. G. Raizen, and D. J. Wineland. Quantum projection noise: Population fluctuations in two-level systems. *Phys. Rev. A*, 47(5):3554–3570, 1993.

[141] A. Polkovnikov. Phase space representation of quantum dynamics. *Ann. Phys. (N. Y).*, 325(8):1790–1852, 2010.

[142] U. Fano. Description of states in quantum mechanics by density matrix and operator techniques. *Rev. Mod. Phys.*, 29:74–93, Jan 1957.

[143] P. B. Blakie, A. S. Bradley, M. J. Davis, R. J. Ballagh, and C. W. Gardiner. Dynamics and statistical mechanics of ultra-cold Bose gases using c-field techniques. *Adv. Phys.*, 57(5):363–455, 2008.

[144] A. Polkovnikov. Quantum corrections to the dynamics of interacting bosons: Beyond the truncated Wigner approximation. *Phys. Rev. A - At. Mol. Opt. Phys.*, 68(5):10, 2003.

[145] A. Sinatra, C. Lobo, and Y. Castin. The truncated Wigner method for Bose-condensed gases: Limits of validity and applications. *J. Phys. B At. Mol. Opt. Phys.*, 35(17):3599–3631, 2002.

[146] F. Petruccione H.-P. Breuer. *Theory of open quantum systems*. Oxford University Press, 2002.

[147] Z. Zhou, Guo-Xian Su, J. C. Halimeh, R. Ott, H. Sun, P. Hauke, B. Yang, Z. Yuan, J. Berges, and Jian-Wei Pan. Thermalization dynamics of a gauge theory on a quantum simulator. pages 1–11, 2021.

[148] M. E. Tai, A. Lukin, M. Rispoli, R. Schittko, T. Menke, D. Borgnia, P. M. Preiss, F. Grusdt, A. M. Kaufman, and M. Greiner. Microscopy of the interacting Harper-Hofstadter model in the two-body limit. *Nature*, 546(7659):519–523, 2017.

[149] V. Kasper, G. Juzeliūnas, M. Lewenstein, F. Jendrzejewski, and E. Zohar. From the jaynes–cummings model to non-abelian gauge theories: a guided tour for the quantum engineer. *New Journal of Physics*, 22(10):103027, oct 2020.

Acknowledgements

Last four years have been *Monumental*. I can neither comprehend the essence of my PhD nor can I reminisce these days without first thinking of all those people who contributed towards its completion.

- My first and foremost gratitude goes to my family, for I wouldn't be writing this page had it not been for their unhindered support, love and most important of all, for their willingness to help a girl child fly beyond the barriers of the society.
- I sincerely thank Fred, my supervisor, mentor and an incredible person for his constant and careful guidance throughout all these years. He has been there always, be it for group activities filled with fun and laughter, or the lab times filled with intense, sometimes quite exhausting experiences. His ability to think from a grad student's perspective, and to understand what sort of support he/she needs, makes him simply exceptional.
- I express my utmost gratitude to Selim, who agreed to be a second referee for this thesis.
- My heartfelt thanks to Markus for understanding the constant struggles in the Na-Li, and for offering his genuine support throughout. His keen observations and inputs have been crucial for my research.
- I thank Jürgen, for being the core of theory collaboration.
- I thank Philipp Hauke for providing valuable insights in the beginning of this project.
- A gigantic thanks to all the current members of NaLi/SoPa/NaKa: Andy, my inseparable colleague, Jan, Lilo and Rohit, the unbreakable trio, Ingrid, Yannick, Lisa, Noah, Gopal, and Leo.
- I thank Jan for proofreading this thesis with extreme attention to detail.
- I thank Robert for being my go-to colleague for any theory doubt under the sun. His patience towards my endless queries has been incredible. My physical understanding of the project improved a great deal, thanks to every single one of our discussions that lasted at least two hours.
- A big thanks to the former members of the Na-Li, Alex and Fabi, for teaching me every little thing in the lab when I first joined the group. Special thanks to Arno, who promptly helped me debug his extremely complicated DDS tower.
- I thank Jolan, who joined the group as a summer intern only for five months and ended up being my favorite for his sassiest and funniest remarks about things.
- I thank all the other former members of the group: Kai, Manu, Alex Hesse, Kerim and Hannes. The last four years would not have been the same without them.

- Honest note of thanks to Helmut, for being that person everybody goes to whenever in doubt, be it conceptual or experimental.
- I thank all the former and current members of SynQS from BECK, ATTA and BEC whose constant inputs related to experimental methods and physical concepts have contributed greatly to this project. It indeed felt like I was a part of something big.
- Thanks to Martin, Thomas, and all the colleagues from the theory department.
- Special thanks to Maciej, Valentin, Daniel and Alexandr from ICFO Barcelona, for developing novel proposals to implement in the experiment, and also for giving me a chance to present my research in their institute.
- I thank Dagmar and Christiane for being the coolest women and helping me with all the administrative works, and most importantly, for always applauding my ability to try and speak broken Deutsch.
- A massive pour of gratitude to all my former teachers and professors for laying the foundation to study physics.
- I thank all my friends and relatives in India for encouraging me throughout these years.
- I thank all my friends in Heidelberg, who have been a constant part of this journey; ranting about a freshly broken piece of equipment in the lab, cooking great food on the night of Diwali, sipping Glühwein in Weihnachtsmarkt. The list is endless.

And at last to the place itself: dear Heidelberg, thank you, for being my second home. Indeed, *ich hab' mein Herz in Heidelberg verloren!*